Hiroshima University Doctoral Thesis

Electronic structure of Kondo insulator $Yb_{1-x}Zr_xB_{12}$ and Kondo lattice $Yb_2Pt_6X_{15}$ (X=Al, Ga) studied by photoemission spectroscopy

(光電子分光による近藤絶縁体 $Yb_{1-x}Zr_xB_{12}$ および近藤格子 $Yb_2Pt_6X_{15}$(X=Al, Ga)の電子状態の研究)

2017

Department of Physical Science,

Graduate School of Science,

Hiroshima University

Awabaikeli Rousuli

Table of Contents

H. Sato, H. Nagata, F. Iga, Y. Osanai, A. Rousuli, K. Mimura, H. Anzai, K. Ichiki, S. Ueda, T. Takabatake, A. Kondo, K. Kindo, K. Shimada, H. Namatame, and M. Taniguchi

J. Electron Spectrosc. Relat. Phennom., in press.

DOI: https://doi.org/10.1016/j.elspec.2017.03.006

(3) Valence transition in polycrystalline $Eu(Rh_{1-x}Co_x)_2Si_2$ studied by hard x-ray photoemission spectroscopy

K. Ichiki, T. Matsumoto, H. Anzai, R. Takeshita, K. Abe, S. Ishihara, T. Uozumi, H. Sato, A. Rousuli, S. Ueda, Y. Taguchi, K. Shimada, H. Namatame, M. Taniguchi, S. Hamano, A. Mitsuda, H. Wada, and K. Mimura

J. Electron Spectrosc. Relat. Phennom., in press.

DOI: https://doi.org/10.1016/j.elspec.2017.03.014

Main Thesis

Doctoral thesis

Electronic structure of Kondo insulator $Yb_{1-x}Zr_xB_{12}$ and Kondo lattice $Yb_2Pt_6X_{15}$ (X=Al, Ga) studied by photoemission spectroscopy

Department of Physical Science,

Graduate School of Science,

Hiroshima University

Awabaikeli Rousuli

August 29, 2017

Contents

List of acronyms

ARPES	Angle-resolved photoemission spectroscopy
BL	Beam line
CB	Conduction-band
DOS	Density of states
E_B	Binding energy
E_F	Fermi level
FL	Fermi-liquid
HAXPES	Hard x-ray photoemission spectroscopy
HiSOR	Hiroshima Synchrotron Radiation Center
LEPES	Low-energy photoemission spectroscopy
PAM	Periodic Anderson model
QCP	Quantum critical point
RKKY	Ruderman-Kittel-Kasuya-Yosida
SIAM	Single-impurity Anderson model
T_K	Kondo temperature
T_{max}	Maximal temperature of magnetic susceptibility
VUVPES	Vacuum ultraviolet photoemission spectroscopy

Chapter1: Introduction

This chapter gives a briefly overview on the rare-earth compounds and physical concepts, such as Kondo effect, Kondo insulators, Kondo lattices, Ruderman-Kittel-Kasuya-Yosida (RKKY) interaction, valence fluctuation, that are used to motivate and interpret the measurements presented in this thesis. Further details can be followed in their respective references.

1.1 Rare-earth compounds

The rare earth elements are consisted of 17 chemical elements in the periodic table, lanthanides, scandium (Sc) and yttrium (Y). And the lanthanides have 15 elements from lanthanum (La) to lutetium (Lu). When the atomic number increases, the number of 4*f* electrons of the lanthanides are increased and 4*f* orbitals fully occupied for Lu with 14 *f* electrons. The radial distribution function of electron orbitals of Ce is shown in Fig. 1.1 [1.1]. Although the 4*f* orbitals are very localized at the atom, the 4*f* orbitals tiny bit extend to out. When they form chemical compounds, the 4*f* orbitals weakly hybridize with the itinerant conduction band electrons, which is called *c-f* hybridization, and form heavy-fermion system.

The heavy-fermion systems exhibit local movement behavior at high temperature, in contrast at low temperature exhibit a fermi liquid (FL) ground state with very large specific heat. The specific heat coefficient of the heavy-fermion systems are several orders larger than a normal metal. Because of the specific heat is proportional to effective mass of quasi particles, thus the effective mass of the quasi particles is ~1000 times larger than that of free electrons. For example, the specific heat coefficient of $CeCu_2Si_2$ is ~1100mJ/(mole•K^2), which is three orders larger than a normal metal [1.2].

In this thesis, our work focuses on the electronic structure of ytterbium (Yb)-based compounds. In this system, Yb has a mixing state of trivalent (Yb^{3+}) with $4f^{13}$ state (one 4*f* hole) and divalent (Yb^{2+}) state with fully occupied $4f^{14}$ state (no 4*f* hole). Because of the *c-f* hybridization, the Yb valence has intermediate value between Yb^{2+} and Yb^{3+}, and in some cases, it changes with decreasing temperature.

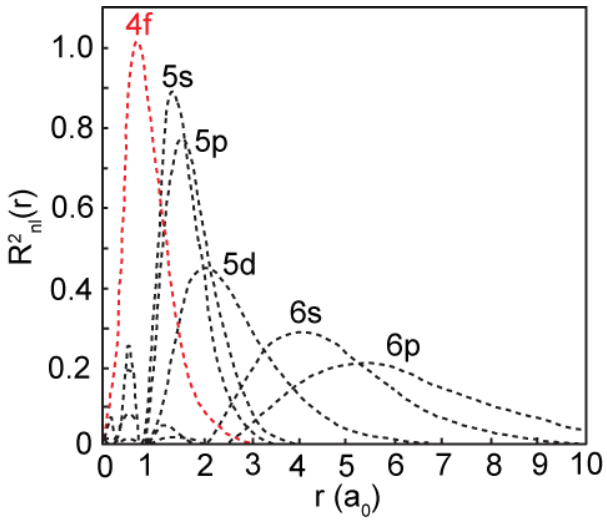

Figure 1.1: Radial distribution function of electron orbitals of Ce [1.1].

1.2 Kondo effect

The main contribution to the electrical resistivity in metals arises from the scattering of the conduction electrons by the nuclei, which vibrate about their equilibrium positions (lattice vibrations). The scattering increases rapidly with increasing temperature and lattice vibrations are more excited. Thus, the electrical resistivity increases (decreases) monotonically with increasing (decreasing) temperature in most metals, and at the same time, there is also a residual temperature-independent resistivity due to the scattering of the electrons with defects, impurities and vacancies in the very low temperature range where the lattice vibrations almost disappeared.

In 1930's, however, a resistance minimum was observed in gold as a function of temperature by Meissner and Voight [1.3] as shown in Fig. 1.2, indicating that there must be some additional scattering mechanism which gives an extra contribution to the resistivity increasing with decreasing temperature. In 1964, Kondo revealed the resistivity minimum due to scattering off individual magnetic impurities [1.4]. Kondo studied the interaction of a 1/2 impurity spin $\boldsymbol{S}$ with a free conduction electrons $\boldsymbol{s}$ via an exchange integral J by using perturbation theory. The associated *s-d* Hamiltonian can be written as

$$H = \sum_{k\sigma} \epsilon_k c^{\dagger}_{k\sigma} c_{k\sigma} + J\boldsymbol{S}\cdot\boldsymbol{s} \,, \tag{1.1}$$

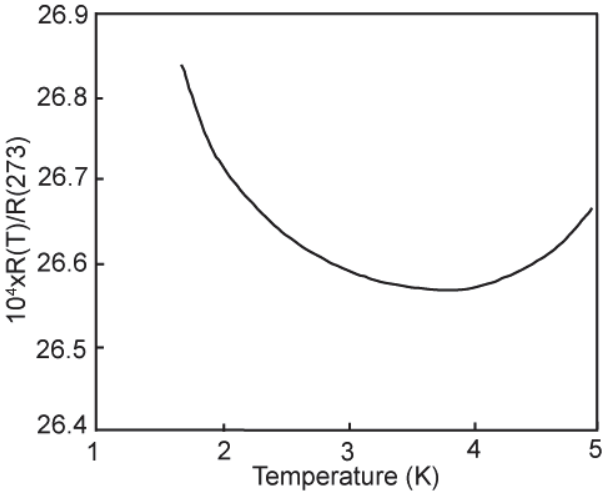

Figure 1.2: The minimum in the resistivity of Au [1.3].

where the first term describes the kinetic energy of the itinerant electrons, ε_k is kinetic energy of conduction electrons, and $c^{\dagger}_{k\sigma}$ and $c_{k\sigma}$ are creation and annihilation operators of conduction electrons with the wave vector k and spin σ, respectively. The second term represents their interaction with the magnetic moment and J is the interaction energy between local spin $\boldsymbol{S}$ and spin density of conduction electrons, $\boldsymbol{s}$, at the localized spin site, respectively. As a result, the resistivity minimum R_{imp} was obtained by using second order perturbation theory as

$$R_{\mathrm{imp}}=R_0\{1+4J\rho_{\mathrm{F}}\log\left(\frac{k_{\mathrm{B}}T}{D}\right)+\ldots\}, \tag{1.2}$$

where ρ_{F} and D are conduction electron density of states (DOS) at the Fermi level (E_{F}) and the band width of the conduction electron states, respectively. R_0 is the resistivity derived within first order perturbation theory (first Born approximation) and k_{B} is the Boltzmann constant. The log$T$ term in this expression is the characteristic term describing the increase of the resistivity with decreasing temperature at low temperature region in Fig. 1.2. However, in the limit of $T\rightarrow 0$, the resistivity diverges due to the log$T$ term. Such an unphysical result constituted the called Kondo problem. The solution came from Wilson by the theory of numerical renormalization group [1.5]. A characteristic temperature called Kondo temperature, T_{K} is given by

$$T_{\mathrm{K}}=k_{\mathrm{B}}^{-1}D\exp(-1/2|J|\rho_{\mathrm{F}}). \tag{1.3}$$

for $T >> T_{\mathrm{K}}$ the system behaves as a normal metal with free magnetic moments following a Curie-Weiss behavior. Around T_{K}, spin flip scattering of conduction electrons on an impurity gradually screens its magnetic moment. Thus, the final

ground state constitutes a non-magnetic singlet state. Such a Kondo singlet results from the complete compensation of the magnetic moments by the built-up cloud of electrons. Thus, the moments become strong scattering centers, which explains the observed resistivity minimum. After screening, for $T << T_K$ a temperature-independent Pauli susceptibility is dominated and the resistivity saturates. Thus, T_K characterizes the energy scale for the formation of the Kondo singlet state. However, it does not represent a phase transition. Furthermore, below T_K the system recovers a Landau FL regime with strong renormalized masses [1.6]. Also, the Kondo effect changes the electronic states near E_F. The strong spin-flip scattering leads to the formation of a resonance level at E_F. Such an enhanced DOS has a width of $\sim k_B T_K$ and is known as the Kondo resonance [1.7, 1.8].

1.3 Kondo insulator

Some strongly correlated electron systems exhibit semiconducting behavior at low temperatures and a narrow band gap opens near E_F in order of 10 meV due to *c-f* hybridization. These systems are called Kondo insulators and also referred as Kondo semiconductors or heavy-fermion semiconductors. In 1969, Menth *et al.* discovered that SmB_6 with nonmagnetic ground state shows a changing from metallic to insulator with decreasing temperature to 0.35 K by the temperature dependent resistivity measurements [1.9]. Another famous Yb-based valence fluctuation Kondo insulator YbB_{12} was discovered by Kasuya *et al.* in 1983 [1.10]. Its resistivity exponentially increases from 100 K on cooling. After discovery of the Kondo insulators, the formation of narrow gaps in these compounds has been extensively studied by using different approach.

Figure 1.3 shows the proposed band structures and DOS of the Kondo insulator and Kondo metal [1.11]. It illustrates the different behaviors of the Kondo insulators with a gap at E_F and the Kondo metal with large DOS near E_F. If the dispersion of the 4*f* band is small as shown in Fig. 1.3(a), a small gap is formed at E_F due to *c-f* hybridization as shown in Fig. 1.3 (b). On the other hand, if the dispersion of the 4*f* band is large due to strong electron-phonon or the other interactions as shown in Fig. 1.3 (c), the DOS near E_F is enhanced due to the *c-f* hybridization (Fig. 1.3(d)).

In real systems, the situation is in general more complex. In the band structure shown in Fig. 1.3, only one conduction band crosses over E_F. However, if more than two bands cross over E_F, no gap is most likely formed, even if the dispersion

is small [1.12]. Thus, further works in theoretical and experiment are necessary to clarify the origin of the insulating properties.

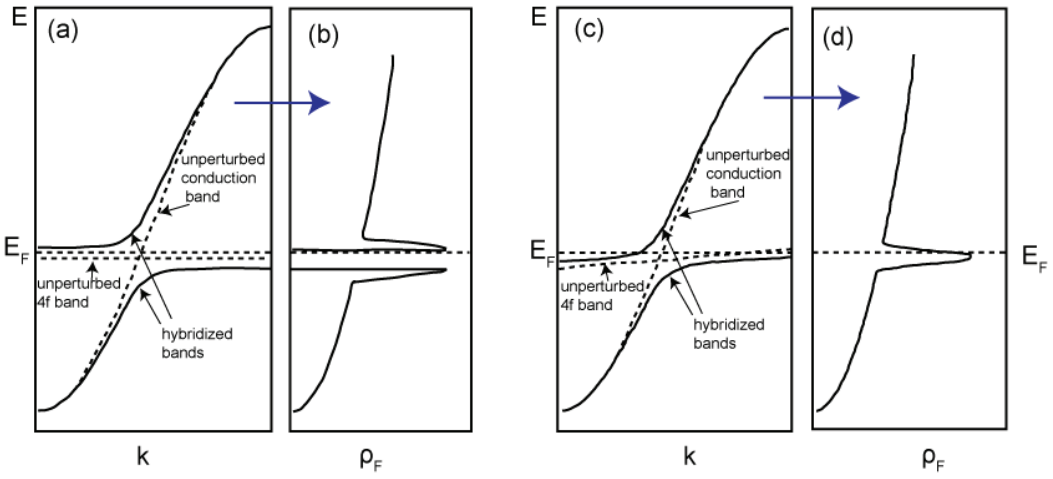

Figure 1.3: Energy and DOS curves for two hybridization models [1.11]. (a) the hybridization model of the nondispersive 4*f* and conduction bands and (b) its energy and DOS curves. (c) the hybridization model of dispersive 4*f* and conduction bands and (d) its energy and DOS curves.

1.4 Kondo lattice model

As described above, the Kondo effect is caused by the antiferromagnetic exchange interaction *J* between the localized magnetic impurities and the conduction electrons. When the localized magnetic ions completely occupy a lattice site, same as the stoichiometric rare-earth compounds, the regular arrangement of the local magnetic moments is called Kondo lattice. Since the magnetic moments obey the translational symmetry of the crystal, the coherence effects due to the formation of extended Bloch states may arise. And it changes the transport properties such as the resistivity.

In the Kondo lattice system, the distance between neighboring local magnetic moments is relatively short compared to the Kondo systems. Although the direct interaction between the magnetic 4*f* moments is still negligible, they may interact by the conduction electrons. A local magnetic moment induces an oscillating spin polarization of the conduction electrons near the magnetic moment, and the conduction electrons affect the orientation of neighboring 4*f* moments. This is an indirect interaction and it is called RKKY interaction which causes a magnetic ordering of the 4*f* moments at low temperatures. The RKKY exchange interaction

J_{RKKY} between two spins $\boldsymbol{S}_i$ and $\boldsymbol{S}_j$ at a distance by r_{ij} from each other, is expressed as

$$J^{ij}_{RKKY}=6\pi Z J^2 \rho_F \left[\frac{\sin(2k_F r_{ij})}{(2k_F r_{ij})^4} - \frac{\cos(2k_F r_{ij})}{(2k_F r_{ij})^3}\right], \tag{1.4}$$

where Z is the number of conduction electrons per atom, ρ_F is DOS of the conduction electrons at E_F and k_F is Fermi momentum [1.13]. The energy sclae related to the RKKY interaction is

$$k_B T_{RKKY} \sim J^2 \rho_F. \tag{1.5}$$

These opposite interactions, the Kondo interaction with a nonmagnetic ground state and RKKY interaction with a magnetic ordered ground state, cause a large variety of low-temperature behaviors in Kondo-lattice compounds. The ground state properties of Kondo lattice system are well illustrated by the Doniach phase diagram in Fig.1.4 [1.14]. T_K and T_{RKKY} are the characteristic temperature curves of the Kondo interaction and RKKY interaction, respectively. In case of a small exchange integral J between the local moments and the conduction electrons, the Kondo interaction is negligibly small. The RKKY interaction overcomes the Kondo interaction and forms a magnetically ordered ground state. With increasing J the Kondo interaction gets strong, and the system reaches the cross point of the RKKY interaction and Kondo effect called quantum critical point (QCP), where magnetic order disappears at 0 K. With further increasing J the Kondo effect becomes stronger and it overcomes the RKKY interaction, and the non-magnetic FL ground state is formed.

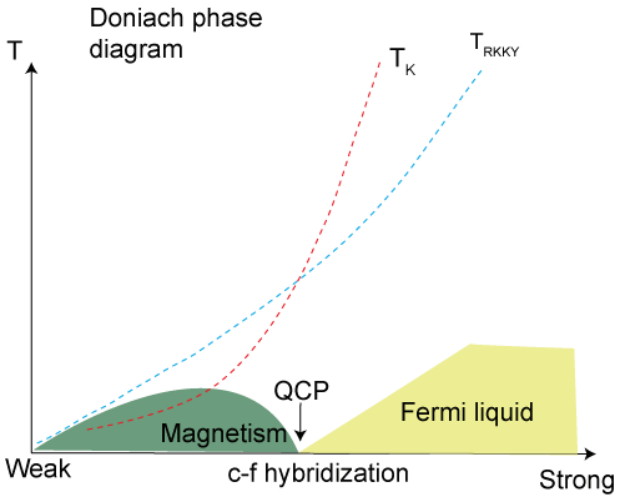

Figure 1.4: Doniach phase diagram [1.14].

1.5 Valence fluctuation

In rare-earth compounds, due to the *c-f* hybridization, the number of 4*f* electrons are perturbed, and this is called valence fluctuation. The valence fluctuation phenomena often occur in Ce, Sm, Eu and Yb compounds and it is a strong challenge to reveal its mechanism for solid-state physicists. In several aspects, the problem plays an important role in our understanding of condensed matter; magnetic moment formation in metals, FL behavior, electron screening and correlation, strong electron-phonon coupling, and magnetic phase transitions, etc. Many excellent articles have already been published on valence fluctuation phenomena, including both of experiments and theories. Recently, the Yb-based superconductor β-$YbAlB_4$ was discovered [1.15] and it shows the strong valence fluctuation with the estimated Yb valence of 2.75 [1.16]. The Kondo insulator YbB_{12} belongs to the valence fluctuation compounds with the valence of 2.9 [1.17,1.18]. In these compound, the origins of anomalous phenomena are possibly related to the valence fluctuation.

The *c-f* hybridization leads to the broadening of bare 4*f* level and the width is expressed as

$$\Gamma=\pi|V|^2\rho_F, \tag{1.6}$$

where V is the matrix elements of the mixing between conduction and 4*f* band electrons. By comparing Γ with 4*f* level (ε_f), we can easily understand the valence fluctuation behaviors of Kondo systems. When $\Gamma \ll \varepsilon_f$, the hybridization is negligibly small, the 4*f* state is well localized and the valence takes an integer value. With increasing the hybridization or shifting ε_f to E_F, the relation $\Gamma \sim \varepsilon_f$ is satisfied. The 4*f* state is no longer localized and Kondo resonance is occurred near E_F. The valence deviates from the integer value. This is called valence fluctuation regime.

1.6 Outline of the thesis

Main work of this thesis is study of the electronic structure of Yb-based compounds, focusing on two Yb compounds. One is famous Kondo insulator YbB_{12}, and the other one is the newly synthesized Kondo lattice compound, $Yb_2Pt_6X_{15}$ (X=Al, Ga).

YbB_{12} exhibits insulating property with a small gap near E_F on cooling. The gap formation mechanism has been controversial. Hayashi *et al.* successfully synthesized $Yb_{1-x}Zr_xB_{12}$ and $Yb_{1-x}R_xB_{12}$ (R=Sc, Y, Lu) single crystals in the wide range of $0 \leq x \leq 0.875$ [1.19]. The temperature of maximum magnetic susceptibility (T_{max}) of YbB_{12} is around 80 K, and it gradually increase with increasing Zr concentration. In contrast, in case of Sc, Y and Lu-doping, T_{max} is almost constant. Therefore, by Zr-doping largely controls T_K of YbB_{12}.

Kondo lattice $Yb_2Pt_2X_{15}$ (X=Al, Ga) was newly synthesized recently and their properties strongly depend on the X atom. Both are valence fluctuation systems with T_K~64 K for $Yb_2Pt_6Al_{15}$ and T_K higher than 1000 K for $Yb_2Pt_6Ga_{15}$ [1.20,1.21]. Recently, Utsumi *et al*. published hard x-ray photoemission spectroscopy (HAXPES) study on Kondo lattices $YbNi_3X_9$ [1.22]. $YbNi_3Al_9$ is an antiferromagnetic heavy-fermion system with T_K of a few K and $YbNi_3Ga_9$ is valence fluctuation system with T_K~570 K. Although the both $Yb_2Pt_6X_{15}$ and $YbNi_3X_9$ have same X and similar crystal structure, moreover, Ni and Pt are belonging to the same family in the periodic table, their properties are different.

In chapter 2 the principles of photoemission spectroscopy which is utilized in these experiments, and experimental set up of synchrotron beam lines and apparatus will be described.

Chapter 3 describes HAXPES and low energy photoemission spectroscopy (LEPES) studies on Zr-doped Kondo insulator YbB_{12}. From the Yb 3*d* HAXPES spectra the Yb valence is estimated and its temperature and Zr-concentration dependences are observed. In the valence-band HAXPES spectra, energy shifts in Yb^{3+} 4*f* spectra toward deeper E_B side with increasing Zr-concentration is observed. The Zr-concentration dependences of the energy positions of the Zr 3*d* and B 1*s* HAXPES spectra are detected. Based on the experimental results, an electronic model is proposed for $Yb_{1-x}Zr_xB_{12}$. It is concluded that the Zr-doping increases conduction band DOS at E_F due to electron doping, and the valence fluctuation becomes stronger. In the LEPES spectra of YbB_{12}, the pseudo gap near E_F is observed and its Zr-concentration dependence is observed. With Zr-doping the pseudo gap gradually closes.

In chapter 4, for comparison with $Yb_{1-x}Zr_xB_{12}$, we performed HAXPES and LEPES on the $Yb_{1-x}R_xB_{12}$ (R=Y, Lu) system. In the Yb 3*d* HAXPES spectra, valence fluctuation behavior and its R substitution and temperature dependences are observed. The valence-band, B 1*s*, Y 3*d* and Lu $3d_{5/2}$ HAXPES spectra show R dependent energy shifts. Moreover, LEPES spectra show the pseudo gap information. Comparing the results with that of $Yb_{1-x}Zr_xB_{12}$, the difference in the

electronic structure and the pseudo gap mechanism are discussed. In conclusion, Zr-doping plays significant role in the pseudo gap closing for YbB_{12}.

Chapter 5 describes the investigation of electronic structure of Kondo lattices $Yb_2Pt_6X_{15}$ by means of HAXPES, vacuum ultraviolet photoemission spectroscopy (VUVPES), LEPES and angle-resolved photoemission spectroscopy (ARPES). The Yb 3*d* HAXPES spectra of $Yb_2Pt_6Al_{15}$ reveal that Yb valence is close to 3+ and decreases with decreasing temperature. In contrast, that of $Yb_2Pt_6Ga_{15}$ is close to 2+ and it is temperature independent. The energy shifts are observed between $Yb_2Pt_6X_{15}$ in the Pt $4f_{7/2}$ and Pt $4d_{5/2}$ HAXPES spectra and Pt 5*d* and Yb^{3+} 4*f* peaks in the valence-band HAXPES and VUVPES spectra. Based on these results, we described the differences between the electronic structures of $Yb_2Pt_6X_{15}$ base on a proposed schematic electronic model. The results are discussed in comparison with those for $YbNi_3X_9$. The DOS of Ni 3*d* and Pt 5*d* at E_F is an origin of the different properties of $Yb_2Pt_6X_{15}$ and $YbNi_3X_9$. In the LEPES spectra of $Yb_2Pt_6X_{15}$, the Kondo peak is successfully observed. The ARPES spectra show very clear band dispersion and characteristic features due to the *c-f* hybridization. The *c-f* hybridization features are fitted with periodic Anderson model (PAM) neglecting 4*f*-4*f* Coulomb interaction and the hybridization energy and effective mass enhancement factor are estimated.

Chapter 6 describes the investigation on the electronic structure of Kondo lattices $YbNi_2X'_2$ (X'=Si, Ge) by means of HAXPES. The Yb 3*d* HAXPES spectra show that the Yb valence of $YbNi_2Si_2$ is close to 3+ and it is temperature-independent. On the other hand, the Yb valence of $YbNi_2Ge_2$ is intermediate valence of 2.9 at 300 K and it decreases with decreasing temperature. We found similar X' dependent spectra of $YbNi_2X'_2$ as $Yb_2Pt_6X_{15}$ and $YbNi_3X_9$.

In chapter 7, we conclude this work by summarizing investigation of each chapter.

Reference:

[1.1] C. Huang. "Rare earth Coordination Chemistry (Fundamentals and Applications) ", John Wiley & Sons (2010).

[1.2] F. Steglich, J. Aarts, C. D. Bredl, W. Lieke, D. Meschede, W. Franz, and H. Schäfer, Phys. Rev. Lett. **43**, 1892 (1979).

[1.3] W. Meissner and G. Voight, Ann. Phys. **7**, 761 (1930).

[1.4] J. Kondo, Prog. Theor. Phys. **32**, 37 (1964).

[1.5] K. G. Wilson, Rev. Mod. Phys. **47**, 773 (1975).

[1.6] P. Nozieres, J. Low Temp. Phys. **17**, 31 (1974).

[1.7] A. A. Abrikosov, Phys. **2**, 5 (1965).

[1.8] H. Suhl, Phys. Rev. **138**, A515 (1965).

[1.9] A. Menth, E. Buehler, and T.H. Geballe, Phys. Rev. Lett. **22**, 295 (1969).

[1.10] M. Kasaya, F. Iga, K. Negishi, S. Nakai, and T. Kasuya, J. Magn. Magn. Mat. **31**, 437 (1983).

[1.11] G. Aeppli and Z. Fisk, Comments Cond. Mat. Phys. **16(3)**, 155 (1992).

[1.12] T. Kasuya, Prog. Theor. Phys. **16**, 581 (1956).

[1.13] H. Tsunetsugu, M. Sigrist, and K. Ueda, Rev. Mod. Phys. **69**, 3 (1997).

[1.14] S. Doniach, Physica B & C **91**, 231 (1977).

[1.15] S. Nakatsuji, K. Kuga, Y. machida, T. Tayama, T. Sakakibara, Y. karaki, H. Ishimoto, S. Yonezawa, Y. Maeno, E. Pearson, G. G. Lonzarichm, L. Balicas, H. Lee, and Z. Fisk, Nature Phys. **4**, 603 (2008).

[1.16] M. Okawa, M. Matsunami, K. Ishizaka, R. Eguchi, M. Taguchi, A. Chainani, Y. Takata, M. Yabashi, K. Tamasaku, Y. Nishino, T. Ishikawa, K. Kuga, N. Horie, S. Nakatsuji, and S. Shin, Phys. Rev. Lett. **104**, 247201 (2010).

[1.17] J. Yamaguchi, A. Sekiyama, S. Imada, H. Fujiwara, M. Yano, T. Miyamachi, G. Funabashi, M. Obara, A. Higashiya, K. Tamasaku, M. Yabashi, T. Ishikawa, F. Iga, T. Takabataki, and S. Suga, Phys. Rev. B **79**, 125121 (2009).

[1.18] Y. Takeda, M. Arita, M. Higashiguchi, K. Shimada, H. Sato, M. Sawada, M. Nakatake, H. Namatame, M. Taniguchi, F. Iga, T. Takabatake, Y. Takata, E. Ikenaga, M. Yabashi, D. Miwa, Y. Nishino, K. Tamasaku, T. Ishikawa, S. Shin, and K. Kobayashi, Physica B **351**, 286 (2004).

[1.19] K. Hayashi, K. Ishii, F. Iga, T. Noguchi, T. Takabatake, A. Kondo, and K. Kindo, JPS Conf. Proc. **3**, 011050 (2014).

[1.20] M. Deppe, S. Hartmann, M. E. Macovei, N. Oeschler, M. Nicklas, and C. Geibel, New J. Phys. **10**, 093017 (2008).

[1.21] S. Ohara. Private communication.

[1.22] Y. Utsumi, H. Sato, S. Ohara, T. Yamashita, K. Mimura, S. Motonami, K. Shimada, S. Ueda, K. Kobayashi, H. Yamaoka, N. Tsujii, N. Hiraoka, H. Namatame, and M. Taniguchi, Phys. Rev. B **86**, 115114 (2012).

Chapter 2: Experimental

2.1 Photoemission spectroscopy

In solid state, the various physical properties of materials, such as electrical, thermal and magnetic properties, are originated from the electrons in materials. Therefore, it is key point to study the electronic structure of materials to understand their physical phenomena. As we know, the photoemission spectroscopy (PES) (also known as photoelectron spectroscopy) is one of powerful and widely used tools to directly investigate the electronic structure of materials. The photoelectric effect is basis of PES and detected by Hertz in 1887 [2.1]. In this chapter, the basic principles of PES and the related experiment techniques are discussed.

2.1.1 Principle of photoemission spectroscopy

Today, the light sources used for PES are a gas-discharge lamp, an X-ray tube, a laser or a synchrotron radiation source. The light with an energy larger than work function of the sample impinges on the sample surface, and the electrons excited by the photoelectric effect are then analyzed by the detector. The important parameters to be measured are the kinetic energy (E_{kin}) of the photoemitted electron. If we know the energy of the light and the work function of the sample, we can determine the binding energy (E_B) of the electrons in the sample relative to the Fermi level (E_F) by using the following equation:

$$E_{kin}=\hbar\omega-\Phi-E_B, \quad (2.1)$$

where $\hbar\omega$ is photon energy and Φ is work function [2.2]. Figure 2.1 shows schematically the energy-level diagram and energy distribution of photoemitted electrons. The solid sample has core levels and valence bands. In the present case, E_F is at the top of the valence bands and is located below the vacuum level. If photo-absorption takes place in a core level with binding energy E_B (E_B = 0 at E_F) the photoelectrons can be detected in the vacuum and their kinetic energies can be calculated by Eq. (2.1).

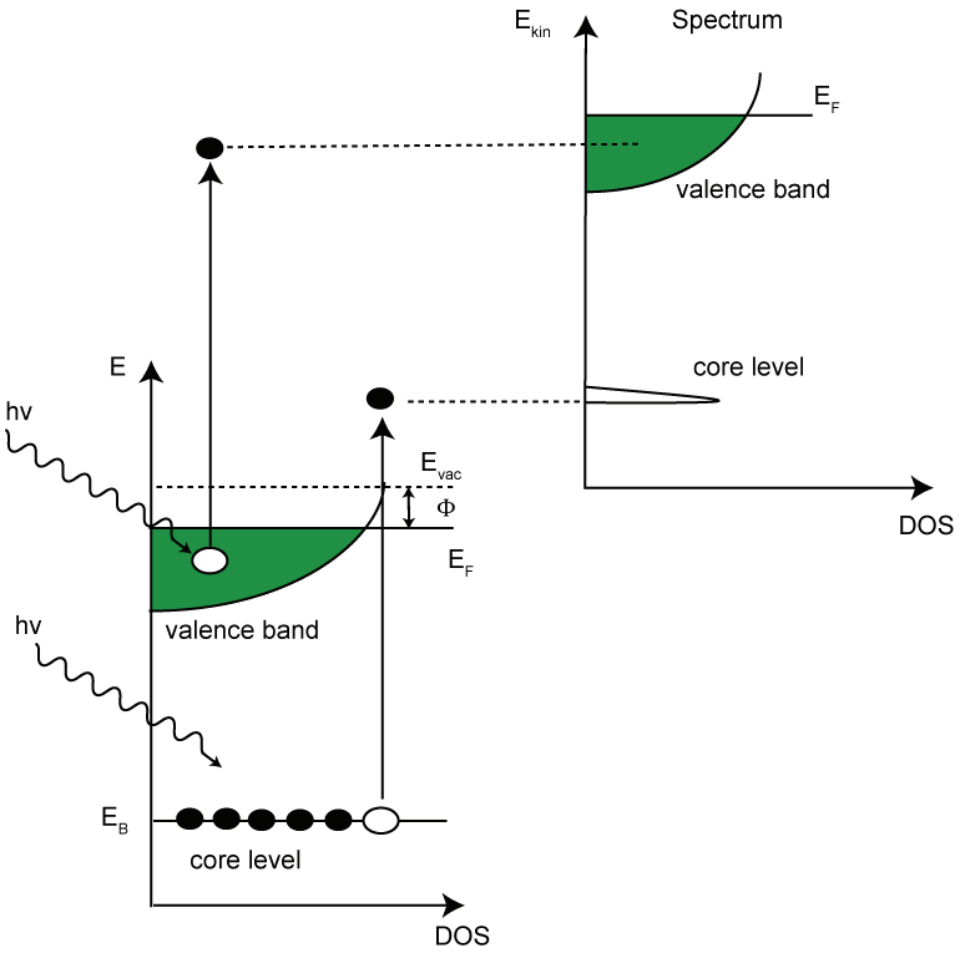

Figure 2.1: Schematic picture of basic principles of PES.

2.1.2 Electron mean free path

In the second step, created photoelectron, as described previous section, is transferred to surface. Generally, although the energy range of the excitation photon in PES can create a photoelectron deep inside the solid, most of the photoelectrons are inelastically scattered during the transport process to the surface and lose their kinetic energy. The inelastic scattered electrons which lose their kinetic energy contribute to creation of the background of a PES spectrum. Moreover, if an electron is created deep inside the solid, is scattered many times and completely loses its kinetic energy, it cannot escape from the surface. Depending on the excitation photon energy (kinetic energy of photoelectron) and element, the escape depth of the photoelectrons is changed. Figure 2.2 shows the electron mean free paths of Rh, Pd, Ag, In, Sn and Cs elements as a function of

electron kinetic energy [2.3]. They have a minimal value around 20-100 eV region with different energies. At energies below 20 eV and higher than 2000 eV, the inelastic mean free path is enhanced and the emitted electrons can reflect the bulk properties of the sample, although they have different inelastic mean free path. The kinetic energy of the minimum inelastic mean free path might come from the inter-band transitions and the plasmon excitation.

However, if the electronic structure of the surface region is the same as in the bulk, the concept of the inelastic mean free path is not so important. In the case of materials that the surface electronic structure is different from the bulk electronic structure, it is important to consider the inelastic mean free path. Among many solid systems, strongly correlated electron systems in which the electron correlation energy U comparable to or larger than the band width D, belong to this category, because the electrons are less itinerant at the surface due to the large U/D compared to those in the bulk where U/D is much reduced. Thus, we should carefully consider the inelastic mean free path for these kinds of materials.

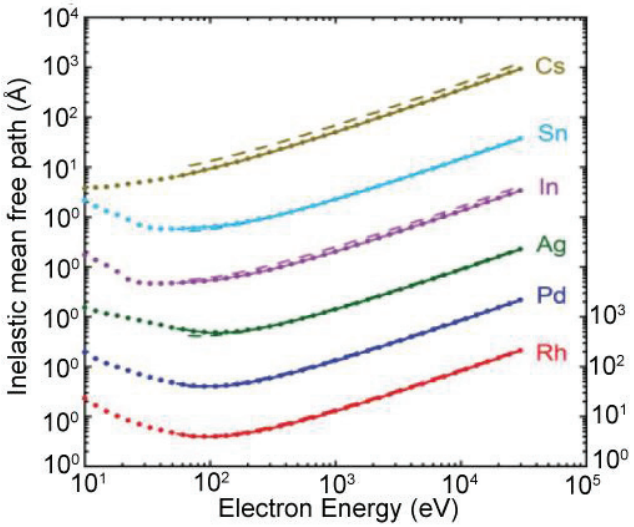

Figure 2.2: Electron inelastic mean free paths as function of electron energy for Rh, Pd, Ag, In, Sn and Cs [2.3].

2.1.3 Angle-resolved photoemission spectroscopy

Angle-resolved PES (ARPES) is one of the well-known experimental tools to observe entire band structure of a material. In ARPES techniques, not only the energies but also the momentum of the electrons in the solids can be probed

simultaneously. In case of the photoexcitation by using low-energy photons, the momentum of incident photon $\hbar\omega/c$ can be neglected compared to the size of the Brillouin zone of the sample, and the wave number of the electron is conserved before and after the photoexcitation except for the reciprocal lattice vector. Thus, the following relationship is satisfied between the wave vector of the initial state (k_i) and that of the final state (k_f):

$$k_f = k_i + G, \tag{2.2}$$

where $G=(G_x, G_y, G_z)$ is an arbitrary reciprocal lattice vector.

Figure 2.3 shows a diagram of the emission of an electron from a solid to vacuum through the surface. When the electron is emitted from the material as shown in Fig. 2.3 (a), the wave vector perpendicular to the surface ($k_{f\perp}$) is changed, whereas the wave vector parallel to the surface ($k_{f||}$) is conserved, because of the transitional symmetry along the surface. Thus, the following relationship is satisfied between the wave vector parallel to the surface of the electron in the solid $k_{f||}$ and emitted photoelectron $K_{||}$,

$$K_{||} = k_{f||} = p_{f||}/\hbar, \tag{2.3}$$

where $p_{f||}$ is a momentum of the electron in the solid. Since $K_{||}$ is related to the kinetic energy of photoelectron E_{kin} and two orthogonal emission angles, polar angle θ and azimuthal angle ϕ as shown in Fig. 2.3 (b), we obtain

$$p_x = \sqrt{2m_e E_{\mathrm{kin}}}\cos\phi\sin\theta = \sqrt{2m_e(\hbar\omega - \Phi - E_{\mathrm{B}})}\cos\phi\sin\theta, \tag{2.4}$$

$$p_y = \sqrt{2m_e E_{\mathrm{kin}}}\sin\phi = \sqrt{2m_e(\hbar\omega - \Phi - E_{\mathrm{B}})}\sin\phi\ , \tag{2.5}$$

where m_e is mass of the free electron. Summarizing Eqs. (2.3) ~ (2.5), we can directly observe both the energy $E \equiv -E_{\mathrm{B}}$ and the parallel momentum $k_{||}$ of the electron in the sample by the photoemission process as

$$k_x = \frac{\sqrt{2m_e E_{\mathrm{kin}}}}{\hbar}\cos\phi\sin\theta + G_x\ , \tag{2.6}$$

$$k_y = \frac{\sqrt{2m_e E_{\mathrm{kin}}}}{\hbar}\sin\phi + G_y. \tag{2.7}$$

In the practical experiments, since the sample is oriented, we have to align its crystal axis depending on the experimental apparatus.

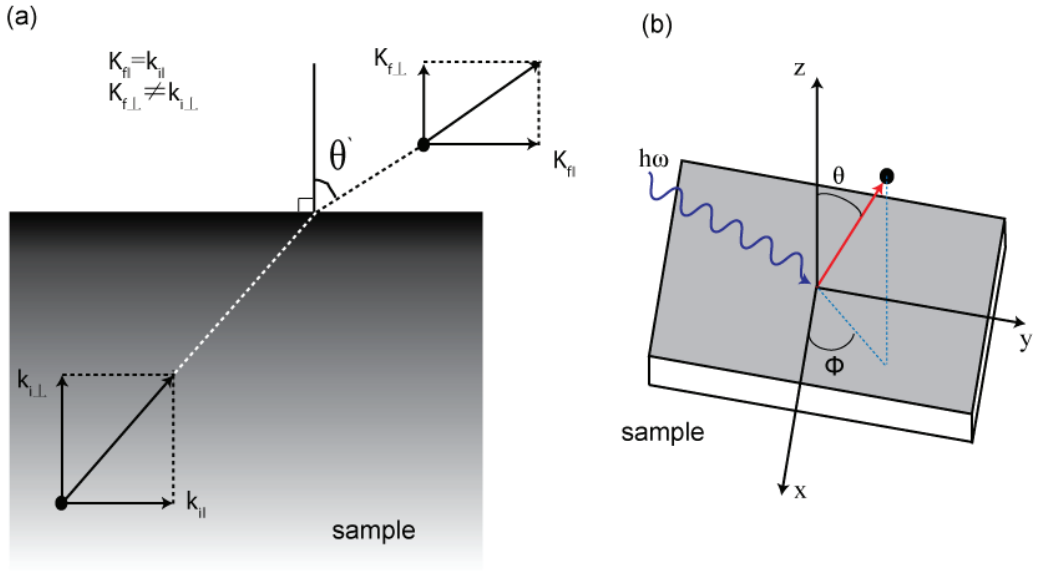

Figure. 2.3: (a) Relations between the photoelectron momentum and the crystal momentum. (b) The angle and axis arrangement of photoelectrons and sample surface.

2.2 Synchrotron radiation

Synchrotron radiation is very intense light emitted from charged particles traveling with close to speed of light. When the direction of electron motion is changed by magnetic field, strong electromagnetic radiation is emitted along the direction of electron motion. Synchrotron radiation was named after its discovery at General Electric synchrotron accelerator in Schenectady, New York in May 1947. In the 1980s, synchrotron radiation has been opened to condensed-matter physicists and physical chemists. After that, they began to recognize the capability of synchrotron radiation to investigate the properties of matter. In the synchrotron radiation facility, electrons accelerated by a microtron etc. to desired speed are injected into the storage ring and are forced to bent by a magnetic field. In that time, synchrotron radiation is produced toward forth.

The synchrotron radiation has been used as light source for different kind of experiments. For our PES experiment the synchrotron radiation shows valuable properties, such as continuous energy from infrared to x-ray regime and different polarized properties etc. Our main PES experiments are done using synchrotron radiation at SPring-8 in Hyogo [2.4] and Hiroshima Synchrotron Radiation Center (HiSOR) in Hiroshima University [2.5].

2.3 Undulator beamline BL15XU at SPring-8

We carried out the hard x-ray PES (HAXPES) at BL15XU at SPring-8. BL15XU is a revolver undulator beamline and provides monochromatic x-rays from 2.2 keV to 36 keV. For HAXPES experiments, the synchrotron radiation is monochromatized to ~6 keV with Si 111 double-crystal monochromator and a post Si 333 channel-cut monochromator [2.6,2.7]. The end station for HAXPES consists of analysis chamber, preparation chamber and load lock chamber. A hemispherical electron-energy analyzer R4000 (VG Scienta) is installed in the analysis chamber. The angle between the optical axis and detection direction of photoelectrons is fixed to 90 degrees. Fig. 2.4 shows schematic layout of BL15XU at SPring-8 [2.8].

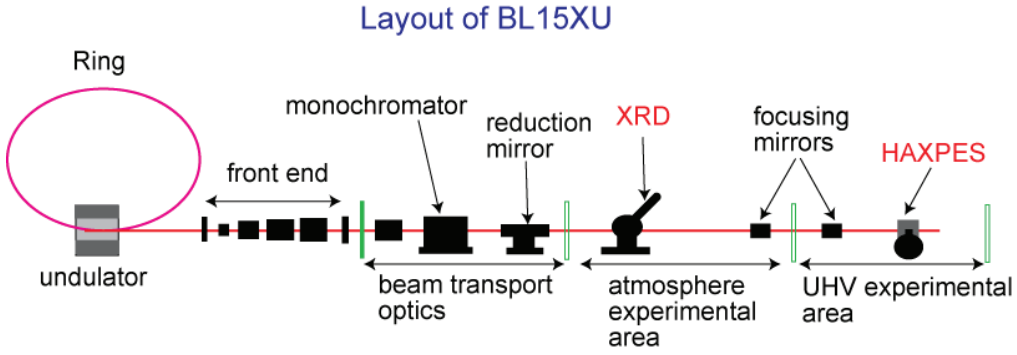

Figure 2.4: Schematic layout of the optical system of BL15XU at SPring-8 [2.8].

2.4 The beamlines at HiSOR

We carried out vacuum ultraviolet PES (VUVPES), ARPES, and low energy PES (LEPES) at HiSOR. The synchrotron radiation is emitted from a compact 700 MeV electron storage ring with a 2.7 T polarized electromagnet (bending magnet). The critical wavelength is 1.42 m and the circumference of the race-truck-type storage ring is 21.95 m. The electron beam lifetime is longer than 10 hours. Linear and Apple II undulators are installed at the two straight sections as an insertion device [2.9,2.10]. Figure 2.5 shows beamlines of HiSOR [2.11]. There are 14 beamlines at HiSOR; 11 beamlines utilize the radiation from bending magnets and 3 from undulators.

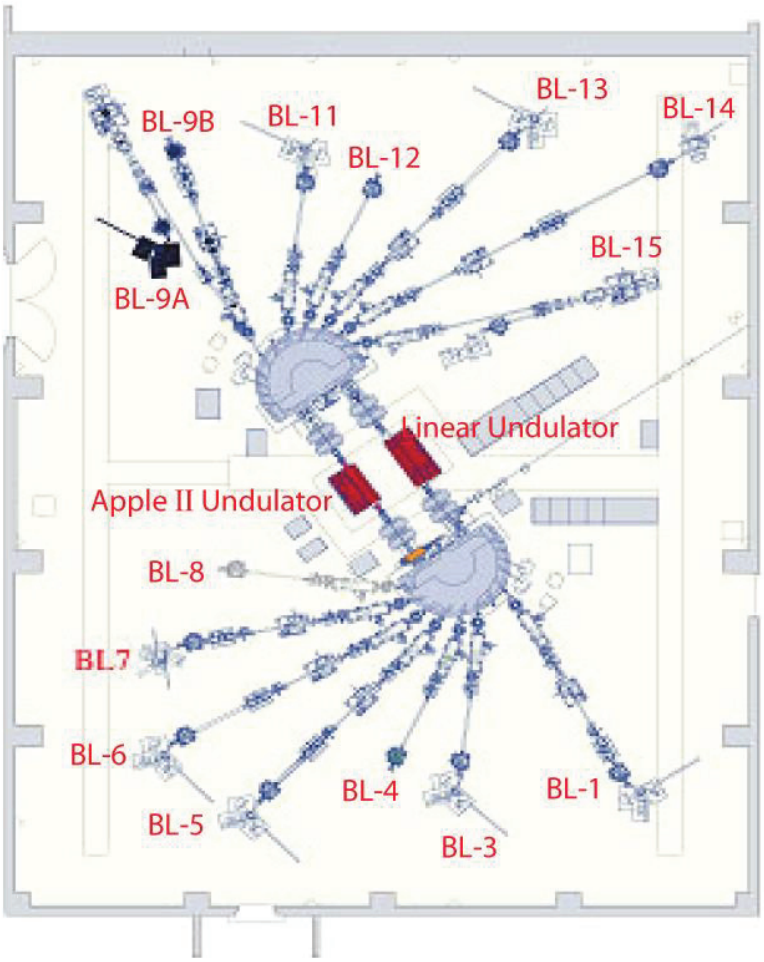

Figure 2.5: Beamlines of HiSOR [2.11].

2.4.1 Linear undulator beamline BL-1 at HiSOR

We carried out ARPES measurements at BL-1 at HiSOR. BL-1 is the linear undulator beamline which provides ultraviolet linearly polarized radiation. The schematic layout of BL-1 is shown in Fig. 2.6 [2.11]. The dragon type grazing incidence monochromator is installed. The beamline consists of four dimensional slits (4DS), water cooled cylindrical mirrors for horizontal focusing (M_0) and vertical focusing (M_1), an entrance slit (S_1), spherical grating (GR), a movable exit slit (S_2) and a refocusing mirror (MF), respectively. The three-interchangeable gold-coated spherical gratings G1 (2000 l/mm), G2 (1400 l/mm) and G3 (2400 l/mm) cover photon energies of $\hbar\omega$=130-300, 90-300 and 26-110 eV, respectively. Two plane mirrors (M_2 and M_3) are inserted between S_1 and GR to reduce the incidence angle.

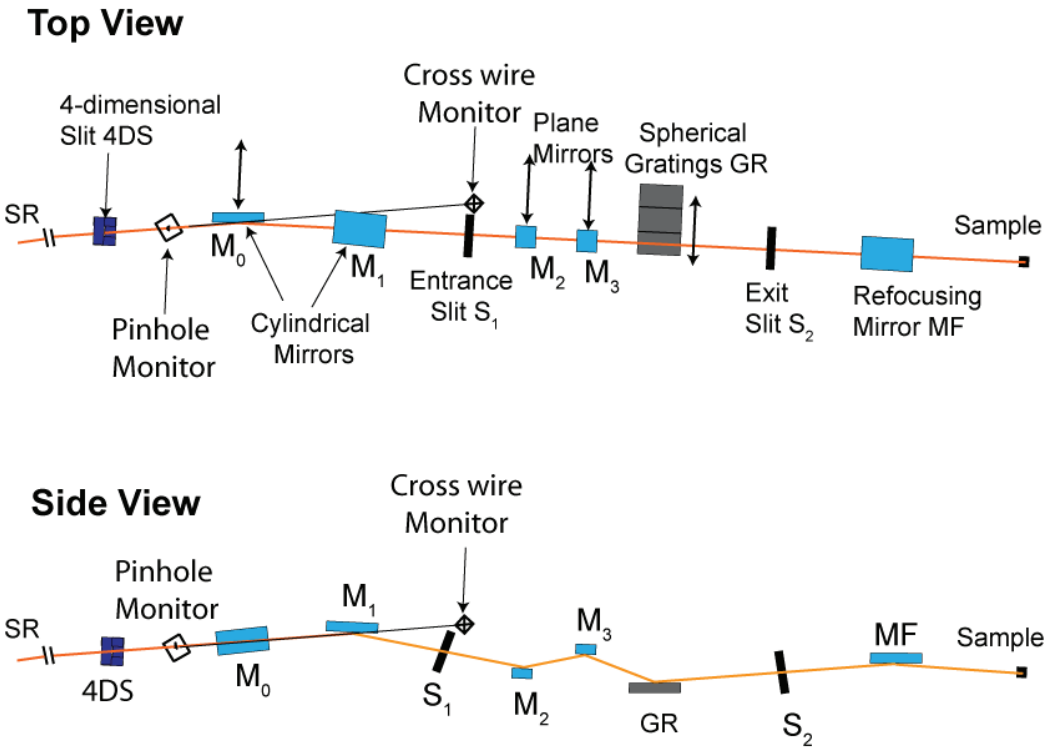

Figure 2.6: Schematic layout of the optical system of BL-1 in the top and side view [2.11].

The end station is consisted of analysis chamber with a high resolution ARPES, preparation and load lock chamber. A hemispherical electron-energy analyzer R4000 (VG Scienta) and liquid-He-flow-type six-axis goniometer (*x*, *y*, *z*, polar, tilt, azimuth) are installed in the analysis chamber. Moreover, we can observe *s*-and *p*-polarization dependences on ARPES measurement by rotating the whole analysis chamber by 90 degrees without broking ultra-high vacuum level.

2.4.2 Helical undulator beamline BL-9A at HiSOR

We carried out high-resolution LEPES and ARPES measurements at BL-9A at HiSOR. BL-9A is helical/linear switchable beamline using the Apple II undulator [2.10,2.12]. A 3m off-plane Eagle type normal-incidence monochromator is installed as a main optical system. Figure 2.7 shows schematic layout of BL-9A [2.11]. The beamline is consisted of a 4-dimensional slit (4DS), a water-cooled toroidal mirror (M_0) and a spherical mirror (M_1), an entrance slit (S_1), two spherical gratings (G1, G2), an exit slit (S_2), a refocusing mirror (MF), and 4DS toward up-to down-stream. Two gratings G1 and G2 are exchangeable in ultrahigh vacuum.

G1 is gold-coated with a line density of 1200 lines/mm and G2 is aluminum-coated with 600 lines/mm, respectively. G1 covers a photon energy region of $\hbar\omega$=10-40 eV, and G2 $\hbar\omega$= 4-12 eV. The circular polarization is more than 96 % [2.10].

The end station is consisted of analysis chamber, preparation and load lock chamber. The hemispherical electron analyzer R4000 (VG Scienta) is equipped and the angle between the optical axis and detection direction of photoelectrons is fixed to 50 degrees. In the analysis chamber, a six-axis liquid-He-flow-type manipulator is equipped and it is covered by radiation shield to prevent the radiation heat and get the lowest sample temperature ~7 K.

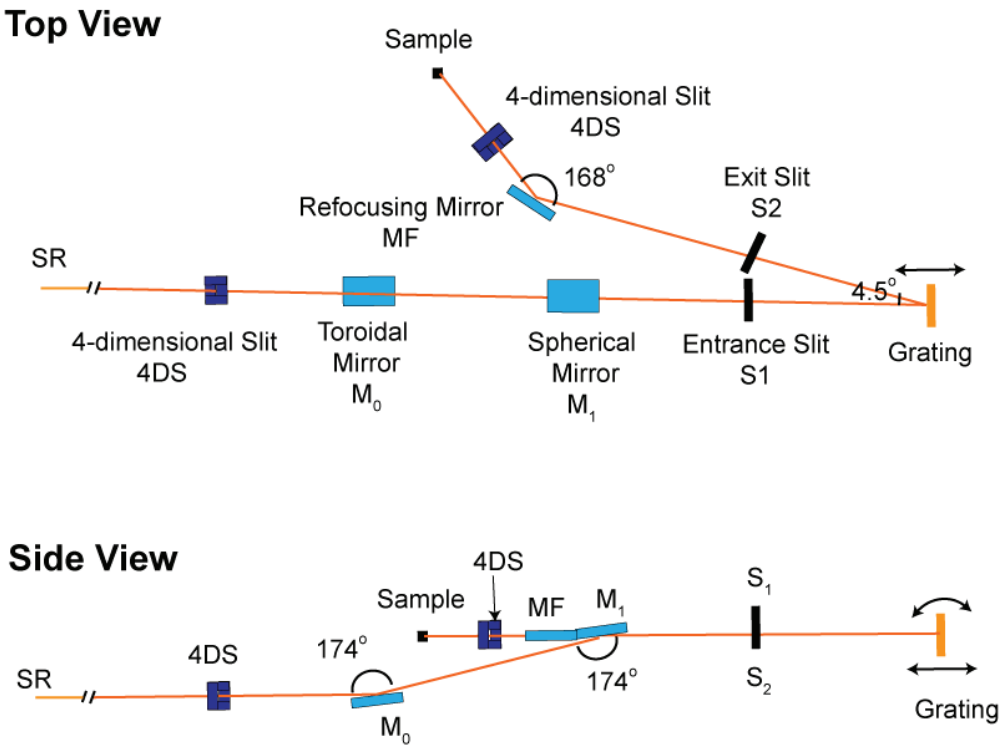

Figure 2.7: Schematic figure of the optical system of BL-9A in the top and side view [2.11].

2.4.3 Bending magnet beamline BL-7 at HiSOR

We carried out high-resolution VUVPES measurements at BL-7 at HiSOR. BL-7 is also an ARPES beamline and installed at bending magnet section of HiSOR ring, operating in the 20-380 eV. The dragon type grazing incidence monochromator is installed. Figure 2.8 shows the schematic image of BL-7 optical system [2.11]. This beam line consisted of two cylindrical mirrors (M_0, M_1),

entrance slit (S_1), two plane mirrors (M_2, M_3), three spherical gratings (G1, G2, G3), exit slit (S_2) and refocusing mirror (MF). G1 covers a photon energy region of $\hbar\omega$=130~380 eV, G2 $\hbar\omega$=60~150 eV, and G3 covers $\hbar\omega$=30~70 eV.

The end station is consisted of analysis chamber, preparation chamber and load lock chamber. A hemispherical electron energy analyzer SES2002 (VG Scienta) and a five-axis liquid-He-flow-type manipulator are installed in analysis chamber. The sample position in the manipulator is covered by radiation shield to prevent radiation heat.

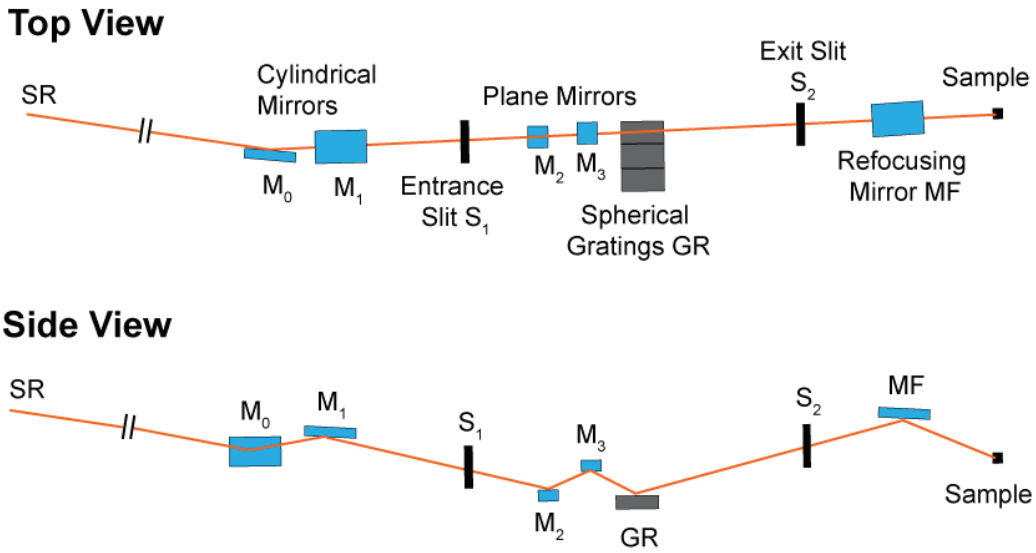

Figure 2.8: Schematic layout of the optical system of BL-7 in the top and side view [2.11].

Reference:

[2.1] H. Hertz, Ann. Physik. **31**, 983 (1887).

[2.2] Stefan Hüfner. "Photoelectron Spectroscopy Principles and Applications, Springer", (1995).

[2.3] S. Tanuma, C. J. Powell, and D. R. Penn, Surf. Interface Anal. **43**, 689 (2011).

[2.4] The SPring-8 web page: http://www.spring8.or.jp/ja/.

[2.5] M. Taniguchi and J. Ghijsen, J. Synchrotron Rad. **5**, 445 (1998).

[2.6] S. Ueda, Y. Katsuya, M. Tanaka, H. Yoshikawa, Y. Yamashita, S. Ishimaru, Y. Matsushita, and K. Kobayashi, AIP Conf. Proc. **1234**, 403 (2010).

[2.7] K. Kobayashi, M. Yabashi, K. Tamasaku, D. Miwa, T. Ishikawa H. Nohira, T. Hattori, Y. Sugita, O. Nakatsuka, A. Sakai, and S. Zaima, Appl. Phys. Lett. **83**, 1005 (2003).

[2.8] The Spring-8 BL15XU web page: http://www.spring8.or.jp/wkg/BL15XU/instrument/langen/INS0000000354/instrument_summary_view.

[2.9] A. Hiraya, K. Yoshida, S. Yagi, M. Taniguchi, S. Kimura, H. Hama, T. Takayama, and D. Amano, J. Synchrotron Rad. **5**, 445 (1998).

[2.10] T. Matsui, H. Sato, K. Shimada, M. Arita, S. Senba, H. Yoshida, K. Shirasawa, M. Morita, A. Hiraya, H. Namatame, and M. Taniguchi, Nucl. Instrum. Meth. A **537**, 467 (2001).

[2.11] HiSOR web page: http://www.hsrc.hiroshima-u.ac.jp/english/bl7.htm.

[2.12] M. Arita, K. Shimada, H. Namatame, and M. Taniguchi, Surf. Rev. Lett. **9**, 1 (2002).

Chapter 3： Photoemission study of Zr-doped Kondo insulator YbB_{12}

3.1 Introduction

Kondo insulators with 4*f* electrons have attracted considerable attention in last few decades. They are metals with a local magnetic moment at high temperature region, in contrast, become an insulator with non-magnetic ground state on cooling and opening a narrow energy gap in the vicinity of Fermi level (E_F). The mechanism behind the gap formation has been controversial; one model assumes presence of a Kondo singlet [3.1,3.2], another proposes the *c-f* hybridization with reduction of the magnitude of the energy gap originated from electron correlation [3.3]. YbB_{12} is well known as one of the most typical Kondo insulators. It has very simple NaCl-type crystal structure (Fig. 3.1) with Yb captions at the sodium ion site and B_{12} dodecahedra at the chlorine ion site, forming the two interpenetrating *fcc* sub-lattices.

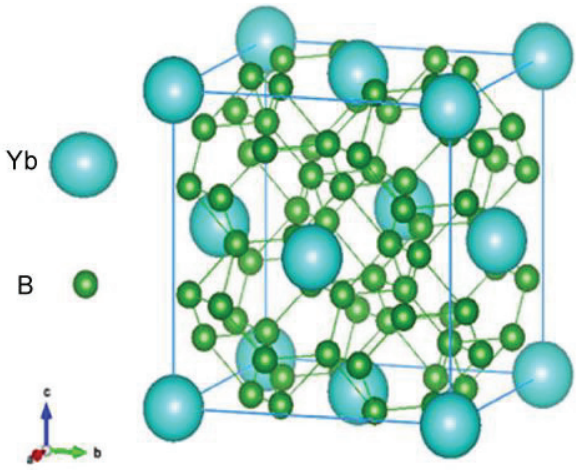

Figures 3.1: Crystal structure of YbB_{12}.

Recently, Hayashi *et al.* successfully synthesized R-doped Kondo insulator $Yb_{1-x}R_xB_{12}$ (R=Lu, Y, Sc and Zr) with the range of $0 \leq x \leq 0.875$ [3.4]. The Zr-concentration dependence of the lattice constants of $Yb_{1-x}Zr_xB_{12}$ is summarized in

Fig. 3.2. The lattice constant of YbB_{12} is a=7.469 Å, and that of $Yb_{1-x}Zr_xB_{12}$ gradually decreases with increasing x. The reason most likely is due to the larger ionic radius of Yb^{3+} (101 pm) than Zr^{4+} (86 pm). We will discuss later, Yb valence of YbB_{12} is almost close to 3+.

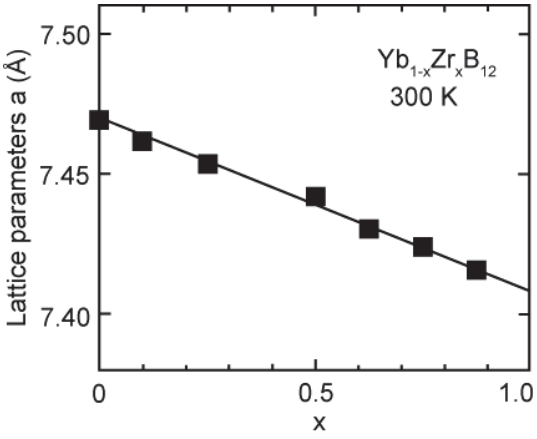

Figure 3.2: Lattice constants of $Yb_{1-x}Zr_xB_{12}$ as a function of x at 300 K [3.4].

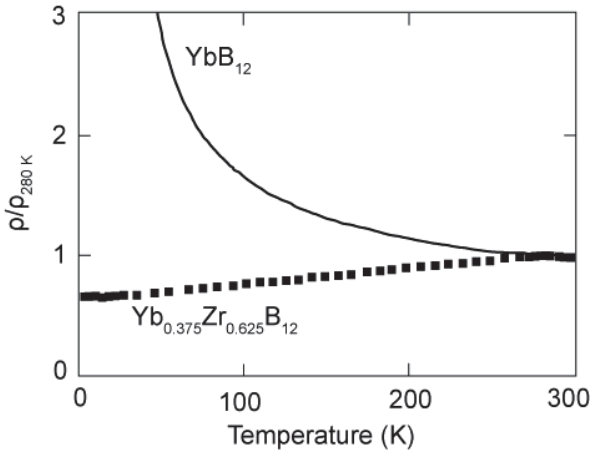

Figure 3.3: Temperature dependences of relative electrical resistivity of YbB_{12} and $Yb_{0.375}Zr_{0.625}B_{12}$ normalized by that at 280 K [3.4].

The temperature dependent relative electrical resistivity of YbB_{12} and $Yb_{0.375}Zr_{0.625}B_{12}$ are shown in Fig. 3.3. The spectra are normalized at 280 K. The resistivity of YbB_{12} shows metallic behavior at high temperature region, and it sharply increases below 50 K on cooling showing insulator behavior. In contrast, the resistivity of $Yb_{0.375}Zr_{0.625}B_{12}$ at low temperature gradually decreases like a normal metal.

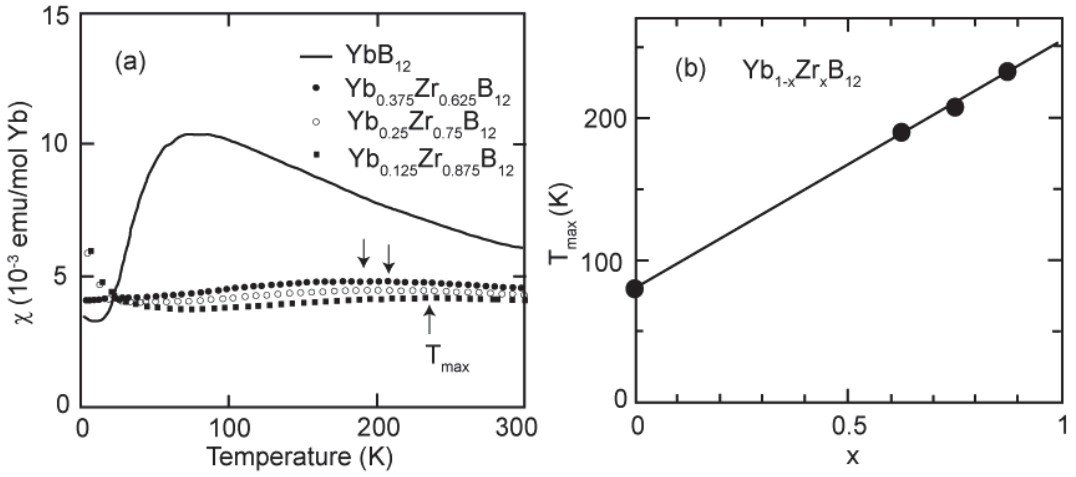

Figures 3.4: (a) Temperature dependent magnetic susceptibility of $Yb_{1-x}Zr_xB_{12}$. (b) Zr-concentration dependent T_{max} of $Yb_{1-x}Zr_xB_{12}$ [3.4].

The temperature dependent magnetic susceptibility of $Yb_{1-x}Zr_xB_{12}$ is shown in Fig. 3.4 (a). The magnetic susceptibility of YbB_{12} shows Curie-Weiss-like behavior above 170 K, and it takes a maximum value at T_{max}=80 K and then it rapidly drops with non-magnetic ground state on cooling [3.5,3.6]. The effective magnetic moment is μ_{eff}=4.4 μ_B, which is very close to that of Yb^{3+} ion of μ_{eff}=4.54 μ_B. Furthermore, T_{max} of the magnetic susceptibility of $Yb_{1-x}Zr_xB_{12}$ gradually increases by Zr-doping and the maximum peak gradually gets broader. T_{max} is summarized in Fig. 3.4 (b) as a function of Zr-concentration. From the figure, we can clearly see T_{max} of $Yb_{1-x}Zr_xB_{12}$ from 80 K for x=0 gradually increases to 220 K for x=0.875. Based on the relation between the Kondo temperature T_K and T_{max}, $T_K \approx 3T_{max}$, T_K changes from 240 K for YbB_{12} to 660 K for $Yb_{0.125}Zr_{0.875}B_{12}$. Therefore, we can control T_K of $Yb_{1-x}Zr_xB_{12}$ by the Zr-concentration.

The nominal electronic configuration of Zr ion is $4d^15s^2$ and it has tetravalent state in these compounds. As reported in hard x-ray photoemission spectroscopy (HAXPES) studies, the Yb valence of YbB_{12} is estimated from Yb 3*d* HAXPES spectra which is taken with $\hbar\omega$=6 keV [3.7] and 8 keV [3.8]. The estimated Yb valence of YbB_{12} is 2.9, almost close to trivalent. When the Yb ion is substituted by the Zr ion, the Zr ion supplies extra one more conduction electron and the Zr-doping works as the electron doping. Therefore, the changes of T_{max} of $Yb_{1-x}Zr_xB_{12}$ by Zr-doping is most likely related with the electron doping.

HAXPES is now widely recognized as one of the powerful tools to reveal bulk electronic states for strongly correlated electron systems, because of the large inelastic mean free path of the photoelectrons of about 100 Å and the sufficient energy resolution of about 0.1 eV. In this study, we investigated the evolution of

the electronic structure of $Yb_{1-x}Zr_xB_{12}$ ($0 \leq x \leq 0.875$) by means of HAXPES with $\hbar\omega$=5.95 keV. To investigate evolution of the pseudo gap, we also performed high resolution low-energy PES (LEPES) measurement on $Yb_{1-x}Zr_xB_{12}$ at $\hbar\omega$=7 eV.

3.2 Experiment

The HAXPES experiments for $Yb_{1-x}Zr_xB_{12}$ were performed at the undulator beamline BL15XU [3.9] of SPring-8. Synchrotron radiation was monochromatized to 5.95 keV with Si 111 double crystal and Si 333 channel-cut monochromators [3.10]. The angle-integrated HAXPES spectra were taken by using a high-energy-resolution hemispherical photoelectron analyzer (VG Scienta R4000). The total energy resolution was set to 240 meV for the whole measurement. Binding energy (E_B) was calibrated with Fermi edge of Au spectra. The LEPES measurements were performed for $Yb_{1-x}Zr_xB_{12}$ at the undulator beamline BL-9A of HiSOR equipped with the Eagle-type normal incidence monochromator [3.11]. We used a high-energy-resolution hemispherical photoelectron analyzer (VG Scienta R4000) for the LEPES measurements. The total energy resolution was ~5 meV and E_B was calibrated with the Fermi edge of Au spectra.

Single crystals of $Yb_{1-x}Zr_xB_{12}$ were synthesized by the traveling-solvent floating method using an image furnace with four Xenon lamps [3.5]. Single phase of the sample was confirmed by x-ray diffraction and the Zr-concentrations were determined by x-ray fluorescence analysis. Clean surfaces for HAXPES and LEPES measurements were obtained by fracturing below 10^{-7} Pa at 300 K and 10^{-9} Pa at 10 K, respectively.

3.3 Results of HAXPES

Figure 3.5 shows HAXPES spectra of $Yb_{0.125}Zr_{0.875}B_{12}$ in the wide energy range measured at 300 K. The Zr 4*p*, Zr 4*s*, Zr 3*d*, B 1*s*, Zr 3*p*, and Zr 3*s* structures are observed at 29, 52, 181, 188, 332 and 432 eV, respectively. Although the signal from O 1*s* state is observed at 531 eV, the intensity is negligibly weak compared to the Zr and B-derived structures.

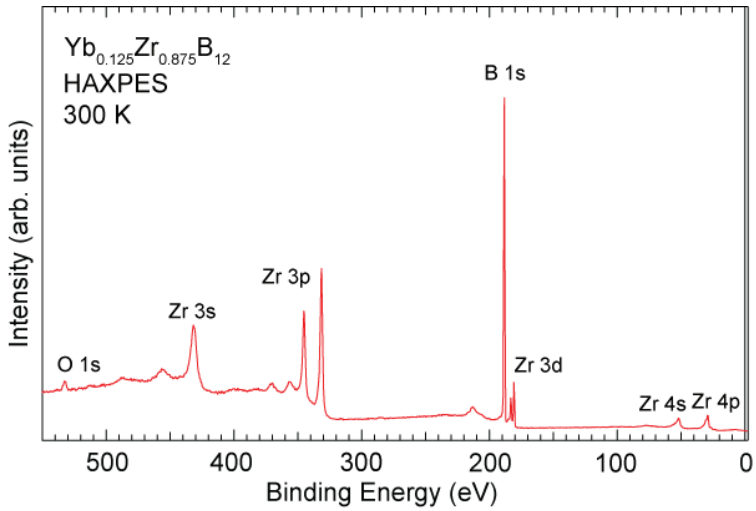

Figure 3.5: HAXPES spectra of $Yb_{0.125}Zr_{0.875}B_{12}$ in the wide energy range measured at 300 K.

Figure 3.6 (a) shows Zr-concentration dependence of the Yb 3*d* HAXPES spectra of $Yb_{1-x}Zr_xB_{12}$ measured between x=0 and 0.875 at 300 K. The Yb 3*d* spectra are split into $3d_{5/2}$ region at 1515 - 1540 eV and $3d_{3/2}$ region at 1560 - 1590 eV due to spin-orbit interaction. Both $3d_{5/2}$ and $3d_{3/2}$ spectra are further split into Yb^{2+} and Yb^{3+} components. The Yb^{2+} components are observed at 1520 and 1568 eV as single peaks, and the Yb^{3+} components at 1524 - 1538 and 1572 - 1584 eV as multiplet structures due to the Coulomb interaction between the 3*d*-photohole and 4*f*-hole of Yb^{3+} in the electronic configurations of the $3d^9 4f^{13}$ final states. Broad structures around 1553 and 1601 eV are attributed to the Yb^{3+}-related plasmon satellites. The small structures at 1545 and 1592 eV in the spectra of $x \geq 0.5$ are observed and its intensity slightly increased with increasing Zr-concentration. These structures were not observed for $Yb_{1-x}Lu_xB_{12}$ [3.8]. They were observed in the Yb 3*d* spectra of $YbNiGe_3$ [3.12] and $YbNi_3Ga_9$ [3.13] compounds with the larger Yb^{2+} component and they are assigned to Yb^{2+} plasmon satellites. The prominent spectral intensity of Yb^{3+} structures indicate that the Yb valence is close to trivalent, which is consistent with previous results [3.8]. We can clearly see that the intensities of the Yb^{2+} (Yb^{3+}) peaks gradually increase (decrease) with increasing Zr-concentration, indicating that Yb valence goes to divalent side. In Fig. 3.6 (a), the spectrum of x = 0.875 is compared with that of YbB_{12} (x = 0) with a dashed line. The Yb^{2+} (Yb^{3+}) spectral intensity of x = 0.875 significantly increases (decreases) compared to that of x = 0. This indicates that the Yb valence decreases by the Zr-doping, and the valence fluctuation becomes stronger.

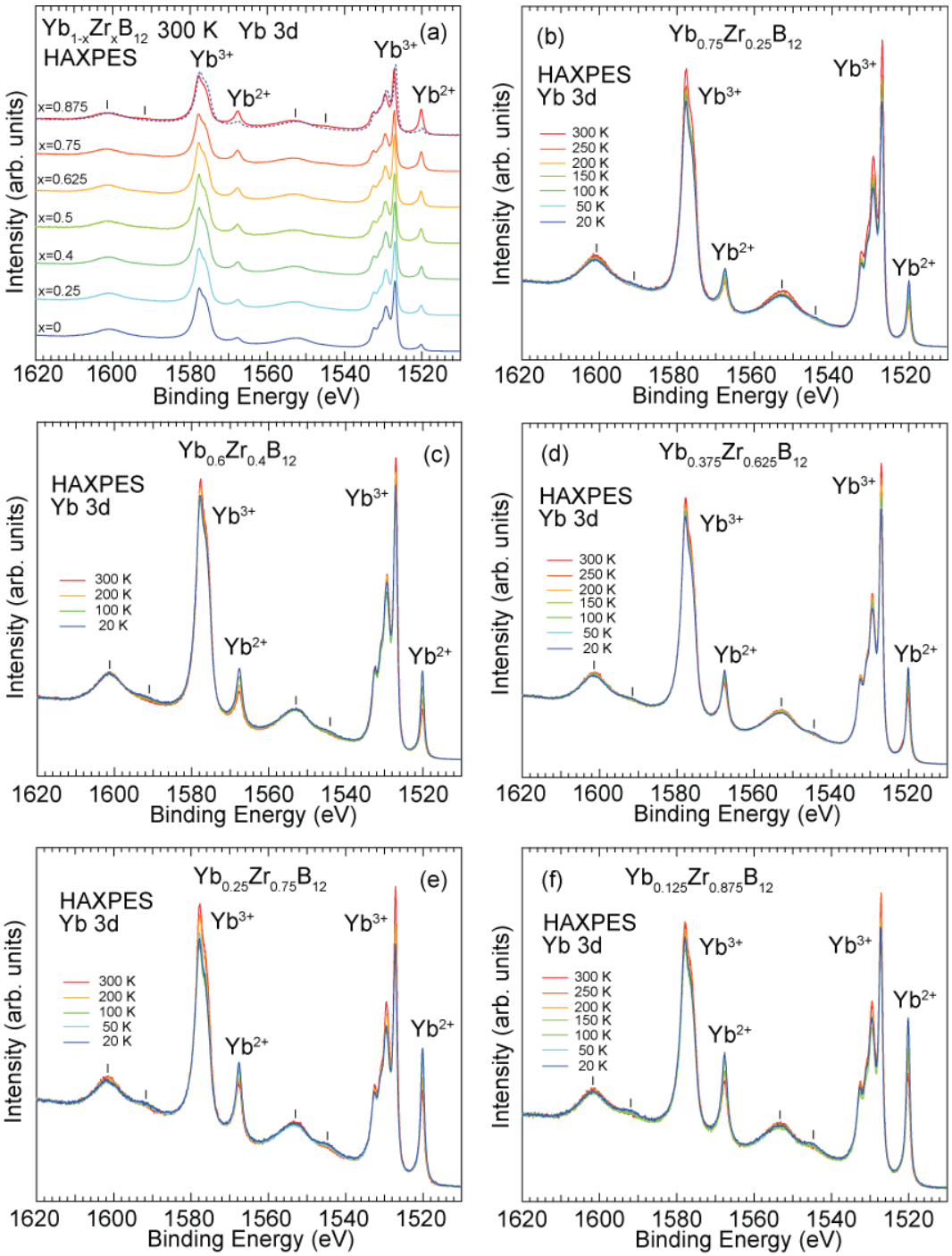

Figure 3.6: (a) Zr-concentration dependence of Yb 3*d* HAXPES spectra of $Yb_{1-x}Zr_xB_{12}$ measured at 300 K. A dashed line on the spectrum of x=0.875 is that of x=0 for comparison. Temperature dependences of Yb 3*d* HAXPES spectra of (b) $Yb_{0.75}Zr_{0.25}B_{12}$, (c) $Yb_{0.6}Zr_{0.4}B_{12}$, (d) $Yb_{0.375}Zr_{0.625}B_{12}$, (e) $Yb_{0.25}Zr_{0.75}B_{12}$ and (f) $Yb_{0.125}Zr_{0.875}B_{12}$ measured between 300 and 20 K. Vertical bars in (a) ~ (f) indicate plasmon satellite structures.

Figures 3.6 (b), (c), (d), (e), and (f) show the temperature dependence of the Yb 3*d* HAXPES spectra of $Yb_{0.75}Zr_{0.25}B_{12}$, $Yb_{0.4}Zr_{0.6}B_{12}$, $Yb_{0.375}Zr_{0.625}B_{12}$, $Yb_{0.25}Zr_{0.75}B_{12}$ and $Yb_{0.125}Zr_{0.875}B_{12}$ measured from 300 K to 20 K, respectively. On cooling, the intensities of the Yb^{2+} (Yb^{3+}) structures slightly increase (decrease), indicating that the Yb valence goes to divalent side. The decrease of the valence on cooling is often observed in the Yb-based valence fluctuation compounds and has previously been reported for YbB_{12} [3.7,3.8].

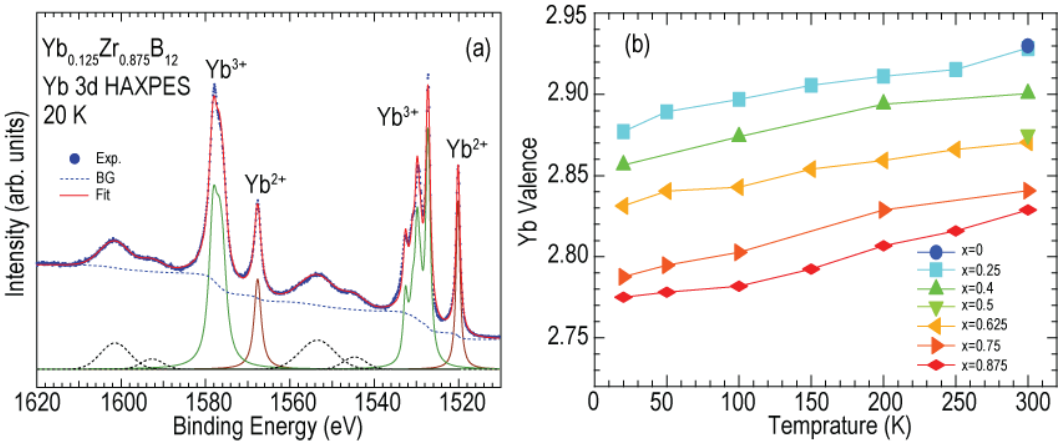

Figure 3.7: (a) Fit of Yb 3*d* HAXPES spectrum of $Yb_{0.125}Zr_{0.875}B_{12}$ measured at 20 K. (b) Estimated Yb valences of $Yb_{1-x}Zr_xB_{12}$ as a function of temperature.

It is known that analysis of the Yb 3*d* spectrum gives the accurate Yb valence of the Yb compounds compared to that of Yb 4*f* spectrum in the valence-band spectra [3.14]. In order to evaluate the Yb valence, we carried out the curve fitting for the Yb 3*d* spectra of $Yb_{1-x}Zr_xB_{12}$. Then the Yb valence is evaluated as $v = 2+I_3/(I_2+I_3)$, where I_2 and I_3 denote the integrated intensities of the Yb^{2+} and Yb^{3+} components, respectively. Figure 3.7 (a) shows the fit of the Yb 3*d* spectrum for x=0.875 at 20 K as an example. The Yb^{2+} components are fitted by a single line spectrum and the Yb^{3+} component some line spectra with a help of atomic multiplet calculation. The line spectra convoluted with the Lorentzian function for lifetime broadening. The Gaussian function are assumed for the plasmon satellites. The background contribution from secondary electrons was estimated from Shirley's method [3.15]. Finally, all spectra convoluted with the Gauss function with the instrumental resolution of 240 meV.

The evaluated Yb valences of $Yb_{1-x}Zr_xB_{12}$ are summarized in Fig. 3.7 (b) as a function of temperature. The Yb valences of $Yb_{1-x}Zr_xB_{12}$ evaluated from Yb 3*d* spectra at 300 K are ~2.93, 2.92, 2.91, 2.90, 2.88, 2.84 and 2.83 for x=0, 0.25, 0.4, 0.5, 0.625, 0.75 and 0.875, respectively. The Yb valences of all the compounds gradually decrease with decreasing temperature to 2.88, 2.86, 2.83, 2.79 and 2.78

at 20 K for x=0.25, 0.4, 0.625, 0.75 and 0.875, respectively. The Yb valences of $Yb_{1-x}Zr_xB_{12}$, thus, gradually shift to divalent side with increasing Zr-concentration and with decreasing temperature, and the valence fluctuation develops with electron doping due to Zr substitution. This kind of Yb valence evolution is observed in $YbNi_3(Ga_{1-x}Al_x)_9$ system [3.16]. The Yb valence of $YbNi_3(Ga_{1-x}Al_x)_9$ gradually shifts to divalent side with increasing x and decreasing temperature. In $YbNi_3(Ga_{1-x}Al_x)_9$, T_{max} of the magnetic susceptibility increases with x.

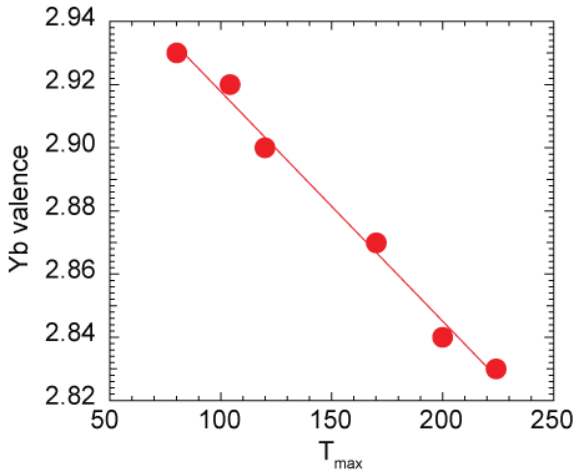

Figure 3.8: Yb valences of $Yb_{1-x}Zr_xB_{12}$ as a function of T_{max} [3.18].

The decrease of the Yb valence of $Yb_{1-x}Zr_xB_{12}$ with increasing Zr-concentration is consistent with the increase of T_{max}; as discussed in introduction part, T_{max}=80 K for x =0 and 220 K for x=0.875 [3.4]. Because of the strength of *c-f* hybridization is represented by T_K, the increasing of T_K with Zr-doping indicating the stronger *c-f* hybridization. According to theoretical calculations [3.17], the Yb valence start to decrease significantly near T_K. Therefore, when increasing T_K, the Yb valence gradually shifts to divalent side. Here, recall the Yb valence of $Yb_{1-x}Zr_xB_{12}$ are 2.94, 2.93, 2.91, 2.87, 2.84 and 2.83 for x=0, 0.25, 0.4, 0.625, 0.75 and 0.875, respectively. Figure 3.8 shows the relation between Yb valence and T_{max} of $Yb_{1-x}Zr_xB_{12}$ [3.18]. The similar trend is observed for $YbNi_3(Ga_{1-x}Al_x)_9$ with T_{max} with increasing Al-concentration up to x=0.15 [3.16]. The Yb valence of $YbNi_3(Ga_{1-x}Al_x)_9$ gradually approaches to 3+ with increasing x, that is T_{max}. The decreasing of the valence with increasing T_{max} as observed for $Yb_{1-x}Zr_xB_{12}$ are similar to $YbNi_3(Ga_{1-x}Al_x)_9$. The similar trend is also reported for $Yb_{1-x}Lu_xAl_3$ ($0 \leq x \leq 0.4$) [3.19]. The Yb valence shifting from magnetic Yb^{3+} to non-magnetic Yb^{2+} can explains suppression of the magnetic susceptibility with Zr-doping as observed in temperature dependent magnetic susceptibility measurement [3.4].

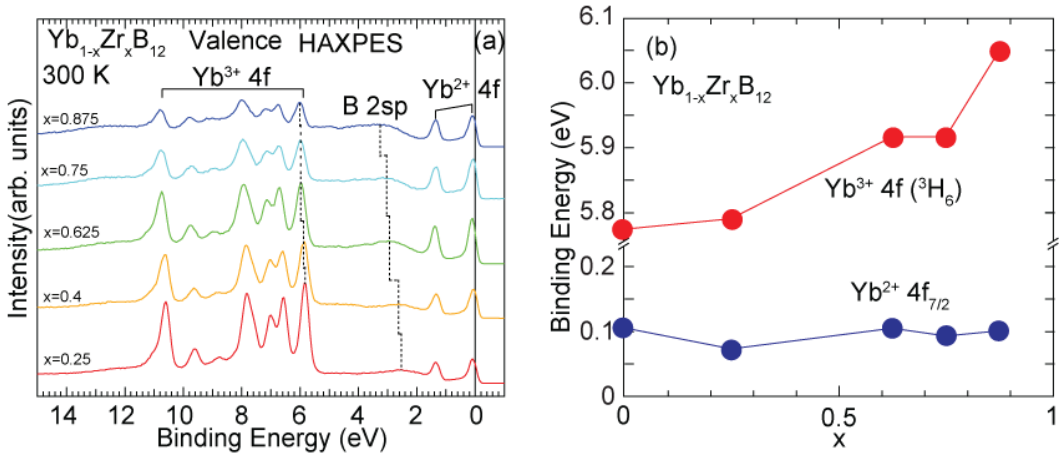

Figure 3.9: (a) Valence-band HAXPES spectra of $Yb_{1-x}Zr_xB_{12}$ (x=0.25, 0.4, 0.625, 0.75 and 0.875) measured at 300 K. (b) Energy positions of Yb^{3+} $4f$ ($^3H_6$) and Yb^{2+} $4f_{7/2}$ peaks of $Yb_{1-x}Zr_xB_{12}$ as a function of Zr-concentration.

In order to investigate how the Yb $4f$ states of $Yb_{1-x}Zr_xB_{12}$ are changed with Zr-doping, we measured valence-band HAXPES spectra. Figure 3.9 (a) shows the valence-band spectra of $Yb_{1-x}Zr_xB_{12}$ with x=0.25, 0.4, 0.625, 0.75 and 0.875 at 300 K. The prominent peaks due to the Yb^{2+} $4f_{7/2}$ and $4f_{5/2}$ states are observed near E_F and at 1.4 eV, respectively. On the other hand, the Yb^{3+} $4f$ state is observed at 5 - 12 eV as multiplet structures due to the $4f^{12}$ final states. The broad structure at ~ 2.7 eV is originated from the B $2sp$ states [3.8]. In this case, the B $2s$ states mainly contribute to the spectrum, because the photoionization cross section of the B $2p$ states at $\hbar\omega$=6 keV is negligibly small compared to that of the B $2s$ states [3.20].

The Yb^{2+} $4f$ intensity relative to the Yb^{3+} $4f$ intensity gradually becomes larger with increasing Zr-concentration, again indicating that the Yb valence moves to the divalent side with Zr-doping. Furthermore, the Yb^{3+} $4f$ multiplet structures gradually shift to the deeper E_B with increasing Zr-concentration. The energy positions of the shallowest peak ($^3H_6$ peak) among the Yb^{3+} $4f$ multiplet structures are plotted as a function of Zr-concentration in Fig. 3.8 (b) together with those of the Yb^{2+} $4f_{7/2}$ peak. The energy shifts of the Yb^{3+} $4f$ multiplet structures is originated by the differences of $4f$-hole level, ε_f, relative to E_F. In the multielectron picture, $\varepsilon_f > 0$ corresponds to the energy required for the $f^{13} \rightarrow f^{14}$ transition (f^{14} final state in the N+1 electron system). E_B for the Yb^{3+} $4f$ peaks (f^{12} final state in the N-1 electron system) is given by $-\varepsilon_f + U$, where U represents for the intra-atomic Coulomb interaction energy between the $4f$ holes. Because U is considered to be unchanged among $Yb_{1-x}Zr_xB_{12}$ due to interatomic character, and the $^3H_6$ peak shift suggests that the decrease of ε_f with Zr-doping. Therefore, the $4f$ hole level continuously shifts to E_F with increasing Zr-concentration. And the decrease of the

Yb valence with Zr-doping in Fig. 3.7 (b) is explained as a result that the conduction electrons are more easily transferred into the Yb^{3+} 4*f* hole level being closer to E_F.

As shown in Fig. 3.9 (a), in contrast to the Yb^{3+} 4*f* multiple structures, the energy position of the Yb^{2+} $4f_{7/2}$ peak is almost unchanged with Zr-doping. The Yb^{2+} $4f_{7/2}$ peak exhibiting just below E_F has been called Kondo-resonance peak [3.7,3.21], although high-energy resolution is required to observe the detailed structures. The peak position is roughly scale with T_K by $\varepsilon_{KR} \sim k_B T_K$, where ε_{KR} is the energy position of Kondo-resonance peak. Therefore, the Yb^{2+} $4f_{7/2}$ peak of $Yb_{1-x}Zr_xB_{12}$ is expected that is shifted to the deeper E_B with Zr-doping since T_K increases with Zr-doping. However, such energy shift could not be detected in the present experimental results as shown in Fig. 3.9 (b). The reason is the inefficient energy resolution of HAXPES for investigating the tiny energy shifts near E_F.

The broad structure at 2-4 eV of the valence-band spectra of $Yb_{1-x}Zr_xB_{12}$ is most likely B 2*sp* states [3.8]. The origin of this structure of $Yb_{1-x}Zr_xB_{12}$ is examined. The photoionization cross section of Zr 5*s*, B 2*s*, B 2*p*, Zr 4*d* and Zr 5*s* states are 45.07, 7.46, 0.04, 39.04 and 45.07 Mb, respectively [3.20]. Among them, the value of Zr 5*s* is the largest and it is larger than that of B 2*s* by one order of magnitude. When we are taking into account molar ratio of constituent elements in $Yb_{1-x}Zr_xB_{12}$, the contribution of the B 2*s* states to the spectrum relative to that of the Zr 5*s* states is estimated to be at least more than 2. Moreover, according to the band-structure calculation of ZrB_{12}, the B 2*s* DOS at 2-4 eV is larger than the Zr 5*s* DOS [3.22]. Therefore, the broad structure at 2-4 eV in the spectrum of $Yb_{1-x}Zr_xB_{12}$ can be assigned to the B 2*sp* (B 2*s*) states. Under the assignment, the B 2*sp*-derived structure of $Yb_{0.25}Zr_{0.75}B_{12}$ is gradually shifted to the deeper E_B with increasing Zr-concentration. This energy shift suggests that Zr-doping elevates E_F of the conduction-band DOS as a result of electron doping.

We measured the B 1*s* and Zr $3d_{5/2}$ HAXPES spectra of $Yb_{1-x}Zr_xB_{12}$ at 300 K in order to investigate the charge distribution of the conduction electrons around the B and Zr atoms. These core levels were selected in order to easily estimate the peak position by their narrow line width. The Zr-concentration dependence of the B 1*s* and Zr $3d_{5/2}$ spectra are shown in Figs. 3.10 (a) and (b), respectively. The B 1*s* peak of YbB_{12} is located at 187.82 eV and is gradually shifted to the deeper E_B with increasing Zr-concentration, consistent with the energy shift of the B 2*sp* structure in the valence-band spectra in Fig. 3.9 (a). The amount of the shift is about 0.3 eV between YbB_{12} and $Yb_{0.125}Zr_{0.875}B_{12}$. The same trend is detected in the Zr $3d_{5/2}$ spectra; the peak position changes from 180.28 eV for $Yb_{0.75}Zr_{0.25}B_{12}$ to 180.42 eV for $Yb_{0.125}Zr_{0.875}B_{12}$. The B 1*s* and Zr $3d_{5/2}$ peak positions are plotted

as a function of Zr-concentration in Fig. 3.11. Although there exists difference in the amount of the energy shift, these results suggest that the E_F position of the conduction-band DOS is shifted to the higher energy as a result of electron doping due to Zr substitution. These energy shifts in B 1*s* and Zr $3d_{5/2}$ states due to the E_F shift is illustrated in Fig. 3.12. Because of the electron doping, E_F shifts to higher energy, and the energy shifts were observed in the B 1*s* and Zr $3d_{5/2}$ core level.

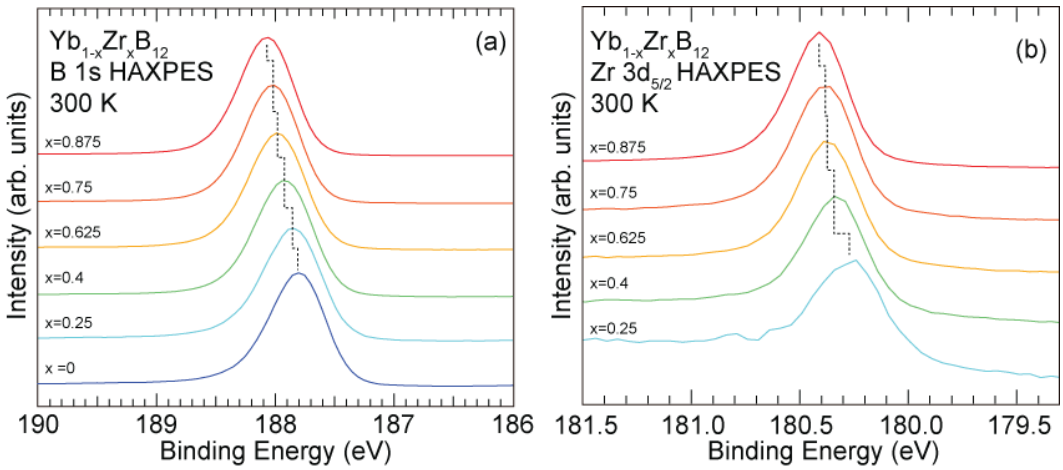

Figure 3.10: Zr-concentration dependence of (a) B 1*s* and Zr $3d_{5/2}$ HAXPES spectra of $Yb_{1-x}Zr_xB_{12}$ measured at 300 K.

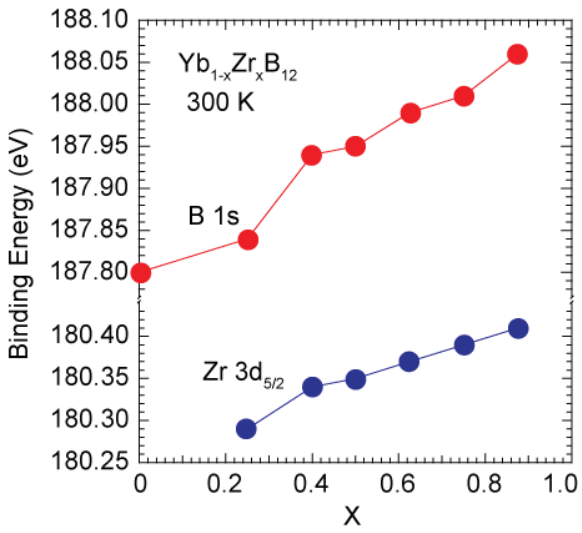

Figure 3.11: B 1*s* and Zr $3d_{5/2}$ peak positions of $Yb_{1-x}Zr_xB_{12}$ as a function of Zr-concentration.

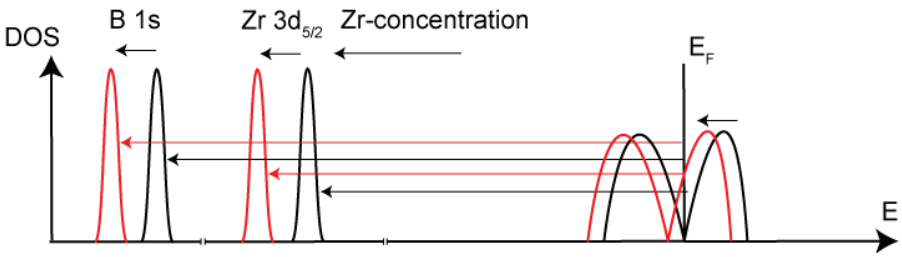

Figure 3.12: Schematic image of the energy shifts of B 1s and Zr $3d_{5/2}$ states toward higher E_B side with increasing Zr-concentration.

3.4 Electronic structure model of $Yb_{1-x}Zr_xB_{12}$

The energy shifts observed in the B 1*s* and Zr $3d_{5/2}$ spectra of $Yb_{1-x}Zr_xB_{12}$ indicate that the E_F-position of the conduction-band DOS moves to higher energy with Zr-doping. Since a narrow energy gap develops at low temperature at E_F of YbB_{12}, E_F should be located in the low DOS region. The supplied electrons by Zr-doping fill the DOS and push E_F to the higher energy, resulting in the increase of DOS at E_F. This induces the enhancement of the *c-f* hybridization and T_K becomes higher, which qualitatively explains the increase of T_{max} of the magnetic susceptibility [3.23]. The decrease of the Yb valence with Zr-doping is induced by the Yb^{3+} 4*f* hole level closer to E_F and enhanced *c-f* hybridization, and correlates with the large change in T_{max} through the enhanced *c-f* hybridization. The valence changes from the magnetic Yb^{3+} to non-magnetic Yb^{2+} suppresses the magnetic susceptibility with Zr-doping.

Yamaguchi *et al*. analyzed the temperature dependence of the Yb valences and Yb 4*f* peak positions of YbB_{12} and $Yb_{0.875}Lu_{0.125}B_{12}$ by the non-crossing approximation calculation based on the single-impurity Anderson model (SIAM) [3.8]. The experimental results of YbB_{12} cannot be interpreted within SIAM and the authors insisted that the Kondo lattice effects are important for describing the bulk electronic states of YbB_{12}. On the other hand, the experimental results of $Yb_{0.875}Lu_{0.125}B_{12}$ are reproduced within SIAM, indicating that the lattice coherence is collapsed already with Lu-doping by 12.5 %. Also for $Yb_{1-x}Zr_xB_{12}$, the coherence should be collapsed at a certain Zr-doping x_{coh}. Since Zr-doping is expected to modify the electronic structure of YbB_{12} compared to Lu-doping, x_{coh} would be smaller than x=0.25, the lowest Zr-concentration in the present experiments. For $x > x_{coh}$, the Yb ion can be treated as the impurity irrespective x and SIAM would be applicable. Under this assumption, the experimental results of $Yb_{1-x}Zr_xB_{12}$ suggest that the *c-f* hybridization qualitatively increases with

increasing Zr-concentration. Within SIAM, T_K is a measure of the *c-f* hybridization and also correlates with T_{max} [3.23]. On the other hand, we find no discontinuity on the Zr-concentration dependences of the Yb valence (Fig. 3.7 (b)) and the energy positions of the Yb^{3+} 4*f* ($^3H_6$) peak (Fig. 3.9 (b)) and B 1*s* peak (Fig. 3.11 (b)) from $Yb_{0.125}Zr_{0.875}B_{12}$ to YbB_{12}. We assume that the *c-f* hybridization strength qualitatively continues to decrease still for $x < x_{coh}$.

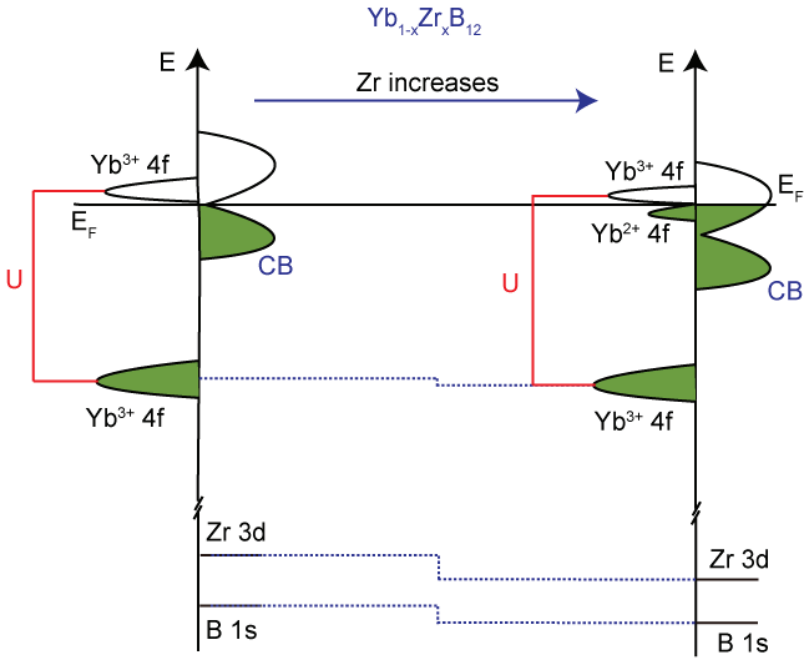

Figure 3.13: Schematic electronic model of $Yb_{1-x}Zr_xB_{12}$. *U* stands for the Coulomb interaction between 4*f* electrons on the same site. The vertical axis represents the energy relative to E_F.

We illustrate the evolution of electronic structure of $Yb_{1-x}Z_xB_{12}$ with increasing Zr-concentration as the schematic electronic model in Fig. 3.13. The vertical axis represents the energy relative to E_F and the Yb 4*f* and conduction band DOS are located at left and right sides of the vertical line, respectively. *U* is the Coulomb interaction energy between the 4*f* electrons. In the low Zr-concentration phase as shown in the left side of the figure, Yb ions are almost trivalent and 4*f* orbitals have one hole just above E_F. With increasing Zr-concentration, going to right side of the figure, the number of conduction electrons become large due to the electron doping by Zr substitution and E_F shifts to higher E_B side leading to the energy shift in the Zr 3*d* and B 1*s* core-level spectra. On the other hand, the Yb^{3+} 4*f* hole level gets closer to E_F and the conduction electrons go

into the Yb^{3+} 4*f* hole just above E_F. The Yb valence becomes small, and the energy position of Yb^{3+} 4*f* multiplet structure in the valence-band spectra shift to higher E_B side. Therefore, the experimental results are well interpreted in this model.

3.5 Results of LEPES

LEPES experiments are useful to investigate the conduction-band states of Yb compounds, because the photo-ionization cross section of the Yb 4*f* states rapidly decreases with decreasing $\hbar\omega$ to several eV [3.24]. In addition to that, very high energy resolution of meV order is achieved at present. In particular, the tiny energy gap of the Kondo insulator as the present system could precisely be investigated by LEPES. We have measured temperature dependent LEPES spectra near E_F for $Yb_{1-x}Zr_xB_{12}$ and investigated the temperature evolution of the energy gap and Zr-doping effect on the energy gap. LEPES was performed at BL-9A at HiSOR.

Figures 3.14 (a), (b), (c), (d) and (e) show the temperature dependence of LEPES spectra near E_F of $Yb_{1-x}Zr_xB_{12}$ with x=0, 0.1, 0.25, 0.4 and 0.5 taken at 7 eV from 210 to ~6 K, respectively. The spectra were normalized with the spectral intensity around 0.14 eV where the spectra show no temperature dependence, and the thermal effect is negligible. In the LEPES spectra of YbB_{12} (Fig. 3.14 (a)), the spectral intensity at E_F gradually decreases with decreasing temperature, reflecting the pseudo gap opening. Two peak structures are observed at 15 and 45 meV as indicated vertical bars in the figure, which were observed by previous LEPES studies [3.25,3.26,3.27]. Okawa *et al*. explain that former peak at 15 meV corresponds to the renormalization band due to the *c-f* hybridization, and the latter structure at 45 meV corresponds to the main peak of the Yb $4f_{7/2}$ state [3.25], which can be clearly seen in the valence-band HAXPES spectra (Fig. 3.9) due to higher photoionization cross-section [3.22]. Takeda *et al*. insisted that the *c-f* hybridization between the Yb 4*f* and 5*d* states plays essential role for the gap formation [3.26]. The *c-f* hybridization peak disappears already at x=0.1 (Fig. 3.14 (b)). Although the small peak seems to be found at x=0.25 (Fig. 3.14 (c)) and to become prominent at x=0.4 (Figs. 3.14 (d)) and x=0.5 (Fig. 3.14 (e)), we consider that the small structure is not the *c-f* hybridization peak. This structure reflects the metallic DOS feature and is only observed like the peak due to the thermal effect.

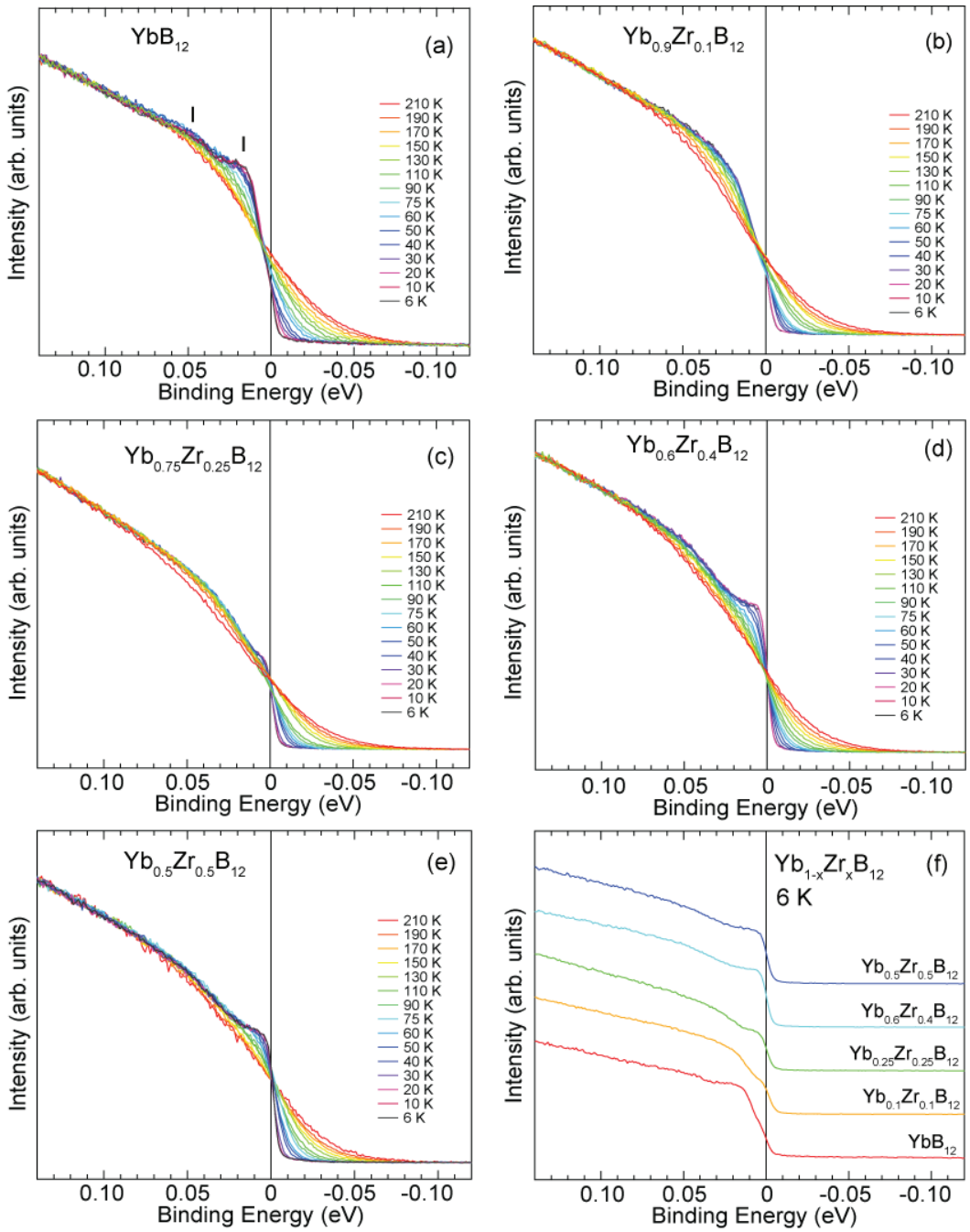

Figure 3.14: Temperature dependence of LEPES spectra of $Yb_{1-x}Zr_xB_{12}$ with (a) x=0, (b) x=0.1, (c) x=0.25, (d) x=0.4 and (e) x=0.5 taken at 7 eV. (f) Zr-doping dependence of the spectra of $Yb_{1-x}Zr_xB_{12}$ at 6 K.

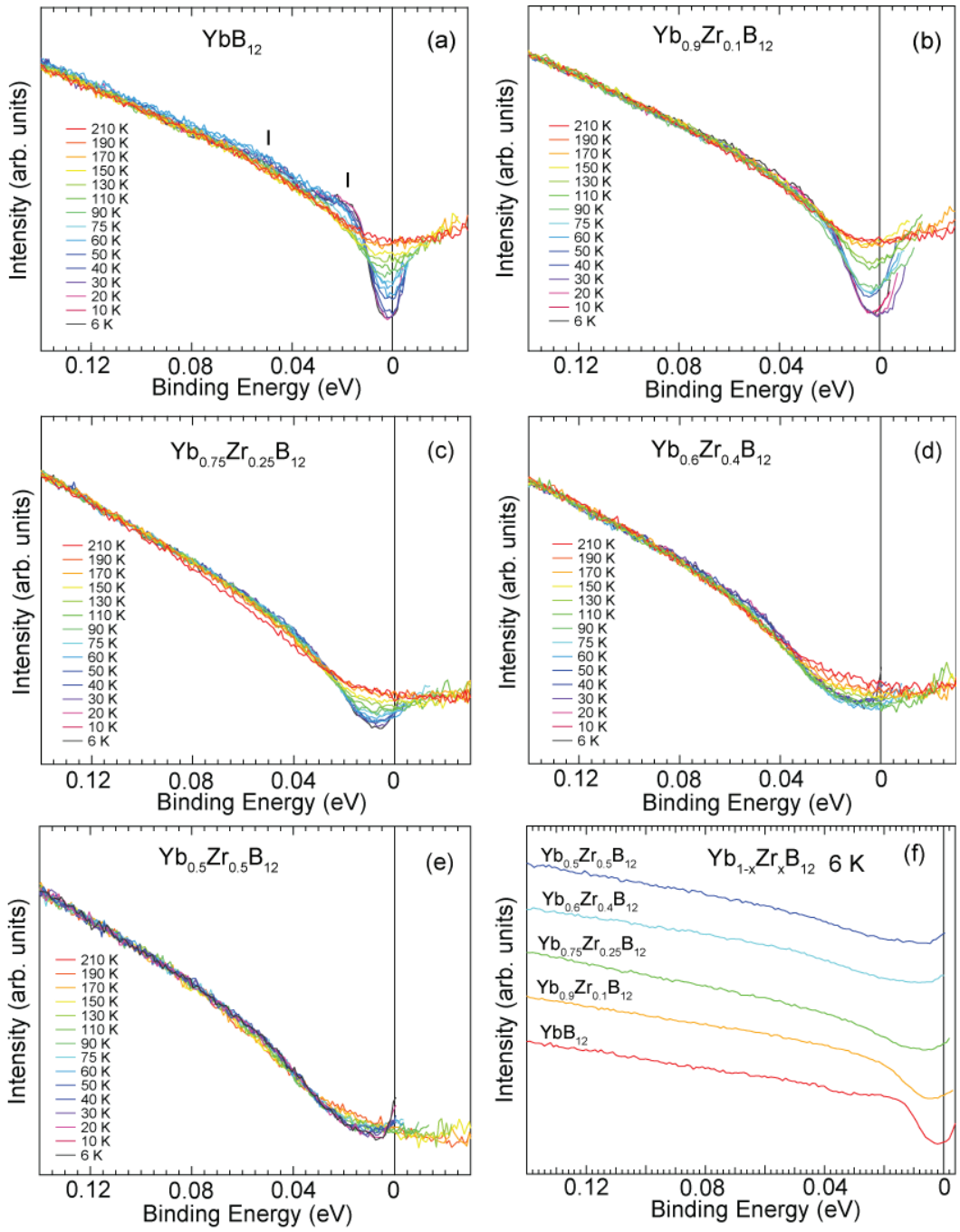

Figure 3.15: Spectral DOS of $Yb_{1-x}Zr_xB_{12}$ with (a) x=0, (b) x=0.1, (c) x=0.25, (d) x=0.4, and (e) x=0.5. (f) Zr-doping dependence of spectral DOS of $Yb_{1-x}Zr_xB_{12}$ at 6 K.

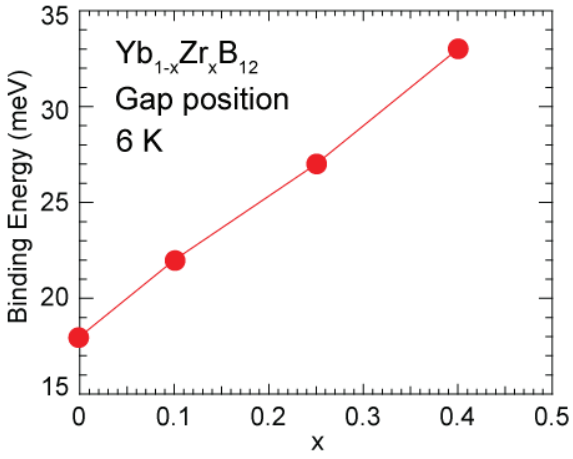

Figure 3.16: Pseudo gap position as a function of Zr-concentration at 6 K.

In the LEPES spectra of YbB_{12}, the cross point of the temperature dependent spectra is located below E_F, reflecting the energy gap opening. The spectral weight near E_F gradually grows up after Zr-doping as shown in Figs. 3.14 (b)-(e). In order to see the doping effects, we show the Zr-doping dependence of the spectra of $Yb_{1-x}Zr_xB_{12}$ measured at 6 K in Fig. 3.14 (f). The spectral intensity around at E_F is gradually recovered by Zr-doping, which reflects that the energy gap is gradually closed.

In order to further discuss on the doping and temperature dependences of the gap behaviors, the spectral DOS of $Yb_{1-x}Zr_xB_{12}$ were obtained by dividing the LEPES spectra in Fig. 3.14 by a Gaussian-broadened Fermi-Dirac distribution function. The results are displayed in Fig. 3.15, where the respective spectral DOS corresponds to the LEPES spectrum in Fig. 3.14. In case of YbB_{12}, DOS at E_F clearly decreases with decreasing temperature, indicating the pseudo gap opening at E_F. The DOS at E_F starts to decrease from 130 K, indicating the gap starts to open around this temperature. The DOS below a characteristic energy of 18 meV is strongly suppressed but DOS above 18 meV is temperature independent. Therefore, we defined this value as the gap size and the size is estimated to be 18 meV.

With the Zr-doping, the suppression of DOS at E_F decreases and almost disappears at x=0.5, indicating that the system becomes close to the metallic. Because of this observation, the small peak in the LEPES spectra of $Yb_{1-x}Zr_xB_{12}$ above $x \geq 0.25$ is not the *c-f* hybridization peak. As seen from the Figs. 3.15 (b)-(e), the peak at 45 meV is almost unchanged and the structure at 15 meV disappears by Zr-doping. The characteristic temperature 130 K for the gap opening is almost unchanged. Fig. 3.15 (f) shows the x-dependence of spectral DOS at 6 K. We find

that the spectral weight at E_F is gradually recovered with increasing the Zr-doping. We plot the gap size of $Yb_{1-x}Zr_xB_{12}$ as a function of x in Fig. 3.16, which almost linearly increases with increasing x. The pseudo gap gradually disappears with increasing its size with the Zr-doping.

3.6 Conclusion

The HAXPES and LEPES measurements were performed on the Zr-doped Kondo insulator YbB_{12}. In the Yb 3*d* HAXPES spectra both Yb^{2+} and Yb^{3+}-derived structures were clearly seen, indicating valence fluctuation. The Yb valence decreases with Zr-doping; it changes from 2.93 for YbB_{12} to 2.83 for $Yb_{0.125}Zr_{0.875}B_{12}$ at 300 K. The decrease of the valence upon cooling is also observed. The Yb^{3+} 4*f* multiplet structures in the valence-band spectra are shifted to the deeper E_B with Zr-doping, reflecting that the Yb^{3+} 4*f* hole level becomes closer to E_F. Which is understood as a result that the supplied electrons by Zr-doping move E_F to higher energy of the conduction-band DOS. The increased DOS at E_F enhances the *c-f* hybridization, leading to the increase of T_{max} as well as T_K. The evolution of electronic structure of $Yb_{1-x}Zr_xB_{12}$ with increasing Zr-concentration is well explained by using schematic electronic model. The detailed gap formation at E_F was investigated by LEPES with $\hbar\omega$=7 eV. In YbB_{12}, the pseudo gap with 18 meV starts to open from 130 K. The *c-f* hybridization peak and Yb $4f_{7/2}$ peak are detected at 15 and 45 meV, respectively. With Zr-doping *c-f* hybridization peak disappears and the spectral DOS at E_F is gradually recovered.

Reference:

[3.1] T. Kasuya, Europhys. Lett. **26**, 277 (1994).

[3.2] S. H. Liu, Phys. Rev. B **63**, 115108 (2001).

[3.3] T. Saso and H. Harima, J Phys. Soc. Jpn. **72**, 1131 (2001).

[3.4] K. Hayashi, K. Ishii, F. Iga, T. Noguchi, T. Takabatake, A. Kondo, and K. Kindo, JPS Conf. Proc. **3**, 011050 (2014).

[3.5] F. Iga, N. Shimizu, and T. Takabatake, J. Magn. Magn. Mater. **177**, 337 (1998).

[3.6] F. Iga, S. Hiura, J. Klijn, N. Shimizu, T. Takabatake, M. Ito, Y.Matsumoto, F. Masaki T. Suzuki, and T. Fujita, Physica B **259**, 312 (1999).

[3.7] Y. Takeda, M. Arita, M. Higashiguchi, K. Shimada, H. Sato, M. Sawada, M. Nakatake, H. Namatame, M. Taniguchi, F. Iga, T. Takabatake, Y. Takata, E. Ikenaga, M. Yabashi, D. Miwa, Y. Nishino, K. Tamasaku, T. Ishikawa, S. Shin, and K. Kobayashi, Physica B **351**, 286 (2004).

[3.8] J. Yamaguchi, A. Sekiyama, S. Imada, H. Fujiwara, M. Yano, T. Miyamachi, G. Funabashi, M. Obara, A. Higashiya, K. Tamasaku, M. Yabashi, T. Ishikawa, F. Iga, T. Takabatake, and S. Suga, Phys. Rev. B **79**, 125121 (2009).

[3.9] S. Ueda, Y. Katsuya, M. Tanaka, H. Yoshikawa, Y. Yamashita, S. Ishimaru, Y. Matsushita, and K. Kobayashi, AIP Conf. Proc. **1234**, 403 (2010).

[3.10] K. Kobayashi, M. Yabashi, K. Tamasaku, D. Miwa, T. Ishikawa H. Nohira, T. Hattori, Y. Sugita, O. Nakatsuka, A. Sakai, and S. Zaima, Appl. Phys. Lett. **83**, 1005 (2003).

[3.11] M. Arita, K. Shimada, H. Namatame, and M. Taniguchi, Surf. Rev. Lett. **9**, 535 (2002).

[3.12] H. Sato, Y. Utsumi, J. Kodama, H. Nagata, M. A. Avila, R. A. Ribeiro, K. Umeo, T. Takabatake, K. Mimura, S. Motonami, H. Anzai, S. Ueda, K. Shimada, H. Namatame, and M. Taniguchi, Phys. Status Solidi C **12**, 620 (2015).

[3.13] Y. Utsumi, H. Sato, S. Ohara, T. Yamashita, K. Mimura, S. Motonami, K. Shimada, S. Ueda, K. Kobayashi, H. Yamaoka, N. Tsujii, N. Hiraoka, H. Namatame, and M. Taniguchi, Phys. Rev. B **86**, 115114 (2012).

[3.14] H. Sato, K. Shimada, M. Arita, K. Hiraoka, K. Kojima, Y. Takeda, K. Yoshikawa, M. Sawada, M. Nakatake, H. Namatame, M. Taniguchi, Y. Takata, E. Ikenaga, S. Shin, K. Kobayashi, K. Tamasaku, Y. Nishino, D. Miwa, M. Yabashi, and T. Ishikawa, Phys. Rev. Lett. **93**, 246404 (2004).

[3.15] D. A. Shirley, Phys. Rev. B **5**, 12 (1972).

[3.16] Y. Utsumi, H. Sato, H. Nagata, J. Kodama, S. Ohara, T. Yamashita, K. Mimura, S. Motonami, M. Arita, S. Ueda, K. Shimada, H. Namatame, and M. Taniguchi, J. Phys. Soc. Conf. Proc. **1**, 012117 (2014).

[3.17] L. H. Tjeng, S.-J. Oh, E.-J. Cho, H.-J. Lin, C. T. Chen, G.-H. Gweon, J.-H. Park, J. W. Allen, T. Suzuki, M. S. Makivic, and D. L. Cox, Phys. Rev. Lett. **71**, 1419 (1993).

[3.18] F. Iga. Private communication.

[3.19] J. Yamaguchi, A. Sekiyama, S. Imada, A. Yamasaki, M. Tsunekawa, T Muro, T. Ebihara, Y. Onuki, and S. Suga, New J. Phys. **9**, 317 (2007).

[3.20] J. H. Scofield, Lawrence Livemore Laboratory, Tech. Rep. UCRL -51326 (1973).

[3.21] M. Matsunami, A. Chainani, M. Taguchi, R. Eguchi, Y. Takata, M. Oura, M. Yabashi, K. Tamasaku, Y. Nishino, T. Ishikawa, M. Kosaka, and S. Shin, J. Phys. Soc. Jpn. **81**, 073702 (2012).

[3.22] S. Thakur, D. Biswas, N. Sahadev, P. K. Biswas, G. Balakrishnan, and K. Maiti, Sci. Rep. **3**, 332 (2013).

[3.23] E. D. Bauer, C. H. Booth, J. M. Lawrence, M. F. Hundley, J. L. Sarrao, J. D. Thompson, P. S. Riseborough, and T. Ebihara, Phys. Rev. B **69**, 125102 (2004).

[3.24] J. J. Yeh and I. Lindau, At. Data Nucl. Data Tables **32**, 1 (1985).

[3.25] M. Okawa, Y. Ishida, M. Takahashi, T. Shimada, F. Iga, T. Takabatake, T. Saitoh, and S. Shin, Phys. Rev. B **92,** 161108 (2015).

[3.26] Y. Takeda, M. Arita, M. Higashiguchi, K. Shimada, H. Namatame, M. Taniguchi, F. Iga, and T. Takabatake, Phys. Rev. B **73**, 033202 (2006).

[3.27] J. Yamaguchi, A. Sekiyama, M. Y. Kimura, H. Sugiyama, Y. Tomida, G. Funabashi, S. Komori, T. Balashov, W. Wulfhekel, T. Ito, S. Kimura, A. Higashiya, K. Tamasaku, M. Yabashi, T Ishikawa, S. Yeo, S.-I. Lee, F Iga, T. Takabatake, and S. Suga, New. J. Phys. **15**, 043042 (2013).

Chapter 4: Photoemission study of Kondo insulators $Yb_{1-x}R_xB_{12}$ (R=Y, Lu)

4.1 Introduction

The electronic structure of Zr-doped Kondo insulator YbB_{12} were investigated by hard x-ray photoemission spectroscopy (HAXPES) and low-energy photoemission spectroscopy (LEPES) as described in Chapter 3. For comparison to $Yb_{1-x}Zr_xB_{12}$, in this chapter we will discuss on R-doped compounds $Yb_{1-x}R_xB_{12}$ (R= Y, Lu) [4.1,4.2]. The Y atom is located next to the Zr atom and the Lu atom below the Y atom in the periodic table as shown in Fig. 4.1. The nominal electronic configurations of Y and Lu are $4d^15s^2$ and $5d^16s^2$, respectively. They have same three conduction electrons of *s* and *d* orbitals for chemical bonding, one less compared to Zr atom ($4d^25s^2$).

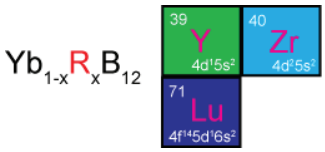

Figure 4.1: Nominal electronic configurations of Y, Lu and Zr atoms in the periodic table.

Figure 4.2 shows temperature dependences of relative electrical resistivity of YbB_{12}, $Yb_{0.25}R_{0.75}B_{12}$, and $Yb_{0.25}Zr_{0.75}B_{12}$ normalized at 280 K [4.1]. The increase at low temperature region observed for YbB_{12} is suppressed with R-doping. Furthermore, as discussed in Chaper 3, the low temperature resistivity is strongly suppressed by Zr-doping and $Yb_{0.25}Zr_{0.75}B_{12}$ becomes almost normal metal.

Figure 4.3 shows the lattice constants of $Yb_{1-x}R_xB_{12}$ as a function of *x* at 300 K. The Y-doping generates increase of the lattice constant, in contrast, the Lu-doping sample shows small variation. These kinds of evolution after R-doping are related to larger ionic radius of Y^{3+} (104 pm) compared to Yb^{3+} (100.8 pm) and almost the same radius of Lu^{3+} (100.1 pm).

Temperature dependences of magnetic susceptibilities of YbB_{12}, $Yb_{0.25}R_{0.75}B_{12}$ and $Yb_{0.25}Zr_{0.75}B_{12}$ are shown in Fig. 4.4 [4.1]. The magnetic susceptibility of YbB_{12} takes the maximum value at T_{max} ~80 K. T_{max} does not so much change with Y and Lu-doping, in contrast to Zr-doped case where T_{max} largely changed due to the electron doping as discussed in Chapter 3.

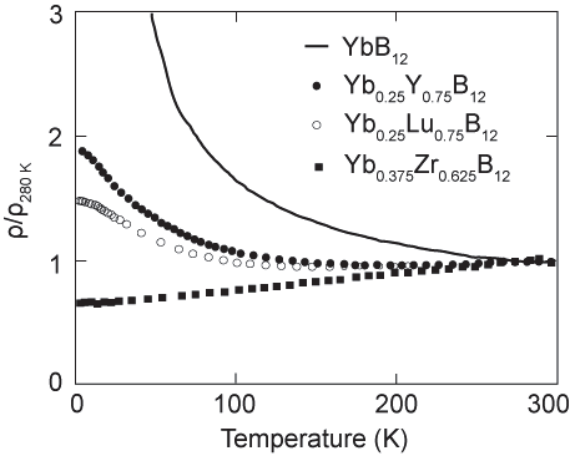

Figure 4.2: Temperature dependences of relative resistivity of YbB_{12} and $Yb_{0.25}R_{0.75}B_{12}$ normalized at 280 K. For comparison, the result of $Yb_{0.375}Zr_{0.625}B_{12}$ is also plotted [4.1].

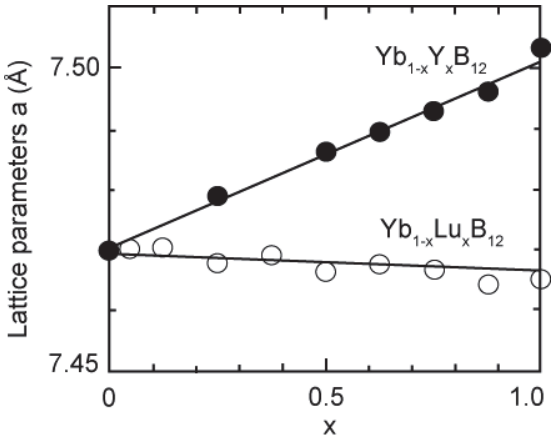

Figure 4.3: Lattice constants of $Yb_{1-x}R_xB_{12}$ as a function of x at 300 K [4.1].

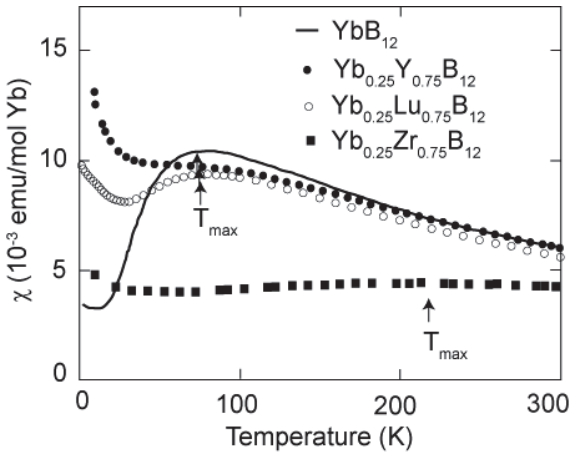

Figure 4.4: Temperature dependent magnetic susceptibilities of YbB_{12} and $Yb_{0.25}R_{0.75}B_{12}$. For comparison, the result of $Yb_{0.25}Zr_{0.75}B_{12}$ is also plotted [4.1].

In this chapter, HAXPES and LEPES measurements for $Yb_{1-x}R_xB_{12}$ will be presented. The Yb valence is estimated from Yb 3*d* HAXPES spectra and the pseudo gap is analyzed based on the LEPES spectra. These results are compared to those of $Yb_{1-x}Zr_xB_{12}$.

4.2 Experiment

Single crystals of $Yb_{1-x}R_xB_{12}$ were synthesized by the traveling-solvent floating method using an image furnace with four Xenon lamps [4.3]. The HAXPES and LEPES experiments for $Yb_{1-x}R_xB_{12}$ were performed at the undulator beamline BL15XU [4.4, 4.5] of SPring-8 and the undulator beamline BL-9A of HiSOR [4.6], respectively. The detailed experimental conditions were described in Chapter 3.

4.3 Results of HAXPES

In order to examine the sample quality, at first, we measured HAXPES spectra in the wide energy region of $Yb_{0.125}Y_{0.875}B_{12}$ and $Yb_{0.125}Lu_{0.875}B_{12}$ as shown in Figs. 4.5 (a) and (b), respectively. In the spectra of $Yb_{0.125}Y_{0.875}B_{12}$, the Y and B-derived structures are very clearly seen. Although, the O 1*s*-derived structures are observed at 531 eV, it is negligibly small compared to the other structure. No signal due to C 1*s* is detected. The same results are obtained for $Yb_{0.125}Lu_{0.875}B_{12}$ (Fig. 4.5 (b)). We clearly see the Lu and B-derived structures and the negligibly weak O 1*s* structure. Therefore, these samples have enough quality for HAXPES.

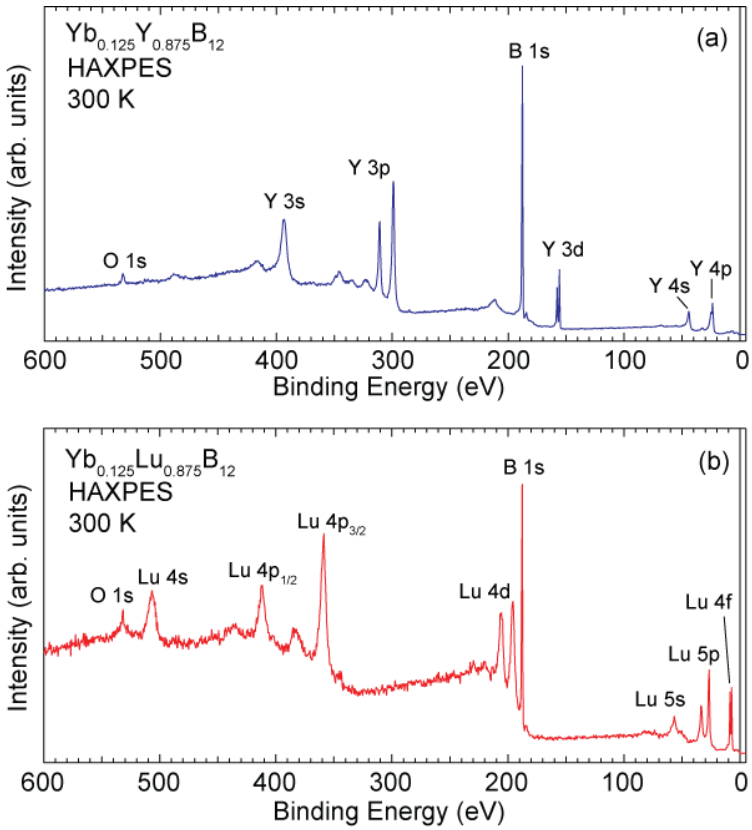

Figure 4.5: HAXPES spectra of (a) $Yb_{0.125}Y_{0.875}B_{12}$ and (b) $Yb_{0.125}Lu_{0.875}B_{12}$ in the wide energy range at 300 K, respectively.

Figures 4.6 (a) and (b) shows the x-dependences of Yb 3d HAXPES spectra of $Yb_{1-x}Y_xB_{12}$ and $Yb_{1-x}Lu_xB_{12}$ at 300 K, respectively. The Yb 3d spectra are split into $3d_{5/2}$ region at 1515-1540 eV and $3d_{3/2}$ region at 1560-1580 eV due to spin-orbit interaction. The Yb^{2+}-derived peaks are observed at 1520 and 1568 eV, while Yb^{3+}-derived multiplet structures are observed at 1524-1536 and 1570-1584 eV. The multiplet structure of Yb^{3+} is due to the $3d^9 4f^{13}$ final state. Broad structures around 1553 and 1601 eV are assigned to plasmon excitations. In case of $Yb_{1-x}Lu_xB_{12}$, the intense Lu $3d_{5/2}$ peak at ~1590 eV disturbs the spectral feature of Yb $3d_{3/2}$ part. For that reason, the enlargement spectra in the Yb $3d_{5/2}$ region is shown in Fig. 4.6 (c). In all the spectra, we can clearly see the intensity of the Yb^{2+} 3d peaks are much weaker than the Yb^{3+} 3d peaks, meaning that the Yb valence is close to 3+. The intensity of the Yb^{2+} 3d peak gradually increases and that of the Yb^{3+} 3d structures decreases with increasing x. In Figs. 4.6 (a) and (c), the spectrum of x=0.875 is compared with that of YbB_{12} (x=0) with a dashed line. The Yb^{2+} (Yb^{3+}) intensity of x=0.875 increases (decreases) compared with that of x=0. This reveals that the Yb valence decreases by R-doping, and the valence fluctuations become stronger.

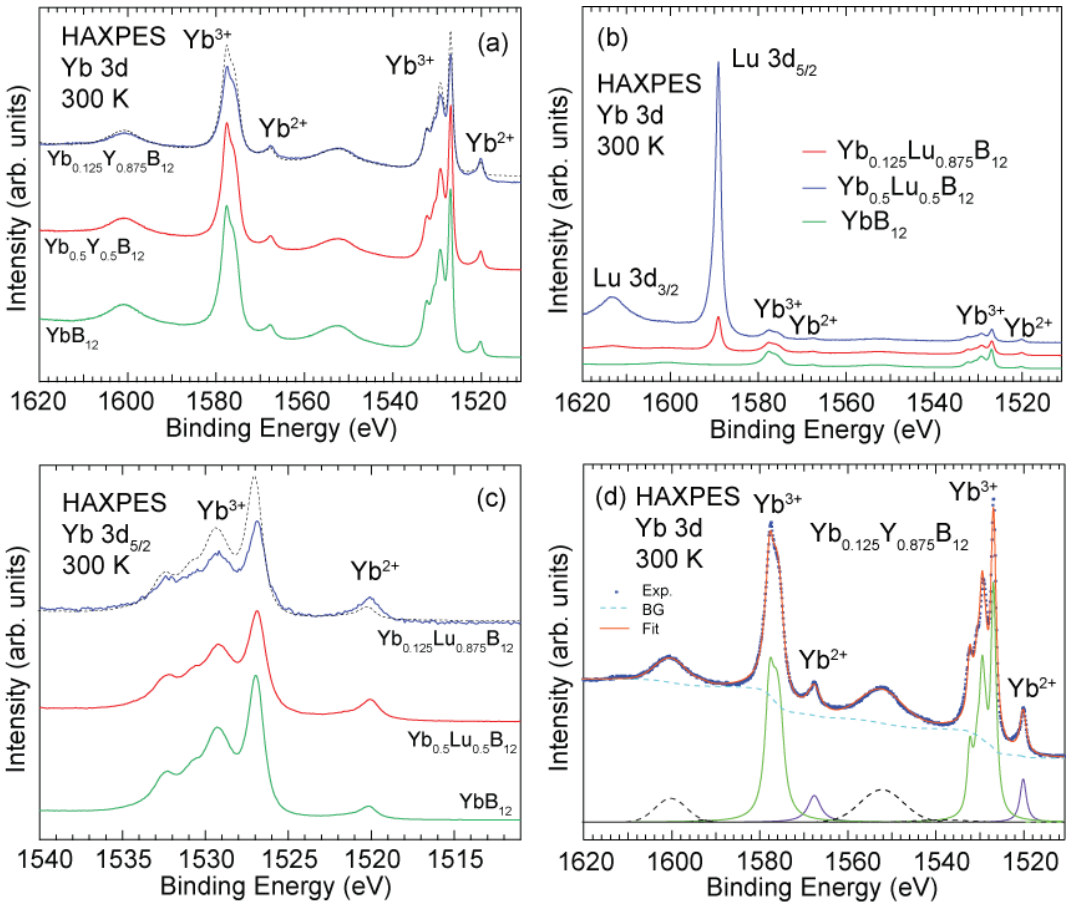

Figure 4.6: (a) Y-concentration dependence of Yb 3*d* HAXPES spectra of $Yb_{1-x}Y_xB_{12}$ measured at 300 K. A dashed line on the spectrum of x=0.875 is that of YbB_{12} for comparison. (b) Lu-concentration dependence of Yb 3*d* HAXPES spectra of $Yb_{1-x}Lu_xB_{12}$ measured at 300 K. (c) Enlarged spectra of (b) at 1511 - 1540 eV. A dashed line on the spectrum of x=0.875 is that of YbB_{12} for comparison. (d) The curve fitting of Yb 3*d* spectrum of $Yb_{0.125}Y_{0.875}B_{12}$ measured at 300 K.

In order to estimate the Yb valences in these compounds, we performed fitting analyses for the Yb 3*d* spectra using calculated line spectra convolved with a Lorentzian function for life time broadening and Gaussian function for instrumental resolution [4.7]. Plasmon-derived structures are assumed as the Gaussian function distribution, and the background contribution of the secondary electrons was estimated from Shirley's method [4.8]. The fitting result of $Yb_{0.125}Y_{0.875}B_{12}$ measured at 300 K is shown in Fig. 4.6 (d). Then the Yb valence is evaluated with the same method as described in Chapter 3.

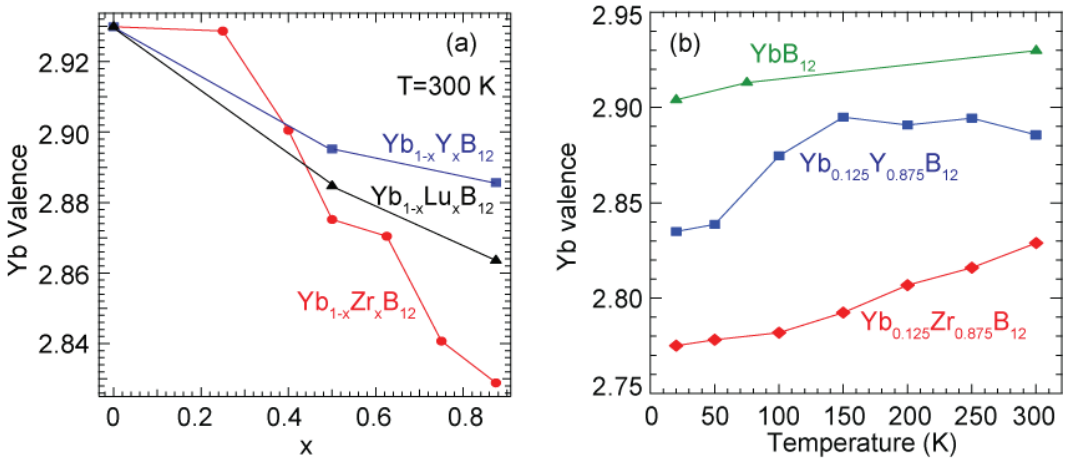

Figure 4.7: (a) R-concentration dependences of Yb valences of $Yb_{1-x}R_xB_{12}$ at 300 K. For comparison, the Yb valences of $Yb_{1-x}Zr_xB_{12}$ are also plotted. (b) Temperature dependent Yb valence of $Yb_{0.125}Y_{0.875}B_{12}$ (x=0.875) evaluated from the fitting analysis of the Yb 3*d* HAXPES spectra. For comparison, the results of YbB_{12} and $Yb_{0.125}Zr_{0.875}B_{12}$ are also plotted. The Yb valences of YbB_{12} at 75 and 20 K are taken from Ref. 4.9.

The evaluated Yb valences are summarized in Figs. 4.7 (a) and 4.7 (b) as functions of x and temperature, respectively. For comparison, the results of $Yb_{1-x}Zr_xB_{12}$ [4.9] also plotted. From Fig. 4.7. (a), the Yb valence of YbB_{12} at 300 K is 2.93 and gradually decreases with increasing x. The Yb valences of $Yb_{0.125}Y_{0.875}B_{12}$ and $Yb_{0.125}Lu_{0.875}B_{12}$ are 2.88 and 2.86 at 300 K, respectively. The decreases in the Yb valence of $Yb_{1-x}Zr_xB_{12}$ is sharper than $Yb_{1-x}R_xB_{12}$. These results indicate that the Yb valence fluctuation develops with R-doping, but the decrement of the valence is smaller than that for the Zr-doping case. Figure 4.7 (b) shows the temperature dependence of the Yb valence in $Yb_{0.125}Y_{0.875}B_{12}$ together with those of YbB_{12} and $Yb_{0.125}Zr_{0.875}B_{12}$ for comparison. The valences of YbB_{12} at 75 and 20 K are taken from Ref. 4.9. The Yb valences of YbB_{12} and $Yb_{0.125}Lu_{0.875}B_{12}$ are 2.90 and 2.86 at 20 K, respectively. In all these compounds, the Yb valence gradually decreases with decreasing temperature indicating valence fluctuation.

Figure 4.8 (a) shows valence-band HAXPES spectra of YbB_{12}, $Yb_{0.125}R_{0.875}B_{12}$ and $Yb_{0.125}Zr_{0.875}B_{12}$ measured at 300 K. The valence-band spectra of all the samples show clear Yb^{2+} 4*f* and Yb^{3+} 4*f*-derived structures. The prominent peaks near Fermi level (E_F) is due to the Yb^{2+} $4f_{7/2}$ state and its spin-orbit interaction partner Yb^{2+} $4f_{5/2}$ is observed at ~1.35 eV. On the other hand, the Yb^{3+} 4*f* state is observed at 5.5 -11.5 eV as multiplet structure due to the $4f^{12}$ final state. The broad structure at 2 - 4 eV is derived from the B 2*sp* states [4.9], as we discussed it in detail in Chapter 3. The intensity of Yb^{2+} 4*f* peaks is lower than Yb^{3+} 4*f* peaks

indicates Yb valence close to 3+ in consistent with the Yb 3*d* HAXPES results. In case of $Yb_{0.125}Lu_{0.875}B_{12}$, the strong peaks in 7.3 and 8.8 eV are derived from Lu 4*f* states [4.9]. We find no clear energy shifts in Yb^{2+} 4*f* structures, while some energy shifts of Yb^{3+} 4*f* structures are observed. In order to clearly see the energy shifts of Yb^{3+} 4*f* structures, the expanded spectra at 5.0 - 7.0 eV are shown in Fig. 4.8 (b). Compared to YbB_{12} spectra, the Yb^{3+} 4*f* multiple structures of $Yb_{0.125}R_{0.875}B_{12}$ slightly shift to deeper E_B side, and in particular, those of $Yb_{0.125}Zr_{0.875}B_{12}$ drastically shift by ~0.16 eV to deeper E_B side. The peak shifts in Yb^{3+} 4*f* structure suggests that the Yb^{3+} 4*f* hole level (ε_f) above E_F gets closer to E_F [4.10,4.11,4.12]. As discussed in Chapter 3, E_B of Yb^{3+} peak is given by $-\varepsilon_f+U$, where U is the intera-atomic Coulomb interaction energy between the 4*f* holes. Since U is considered to be unchanged among $Yb_{1-x}R_xB_{12}$ and $Yb_{1-x}Zr_xB_{12}$, the large energy shifts in $Yb_{0.125}Zr_{0.875}B_{12}$ suggest that the Yb^{3+} 4*f* hole level closer to E_F compared to those of $Yb_{1-x}R_xB_{12}$, and conduction electron more easily transfer into the holes, resulting that the Yb valence of $Yb_{1-x}Zr_xB_{12}$ largely decreases compared to those of $Yb_{0.125}R_{0.875}B_{12}$ as shown in Fig. 4.7.

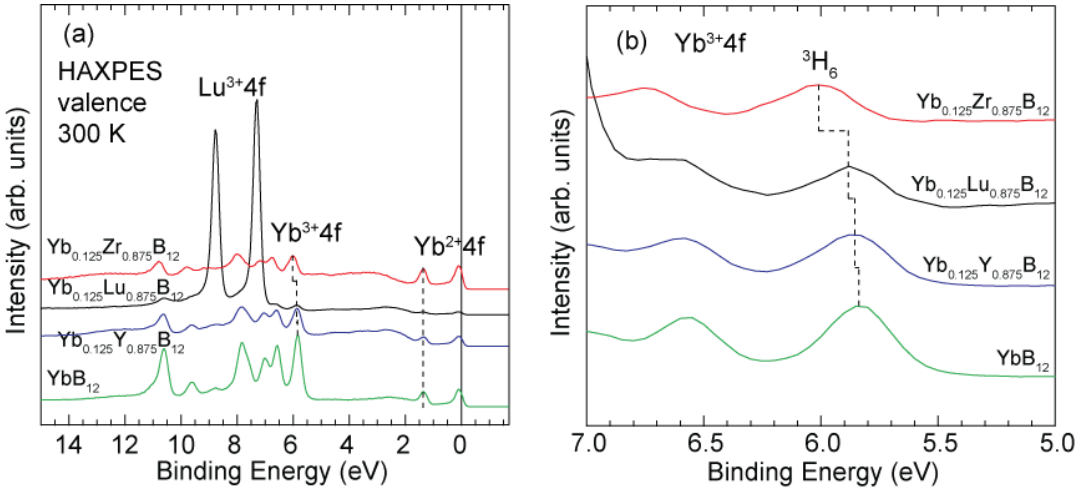

Figure 4.8: (a) Valence-band HAXPES spectra of YbB_{12}, $Yb_{0.125}R_{0.875}B_{12}$ and $Yb_{0.125}Zr_{0.875}B_{12}$ measured at 300 K. (b) The expanded spectra of (a) at 5.0-7.0 eV.

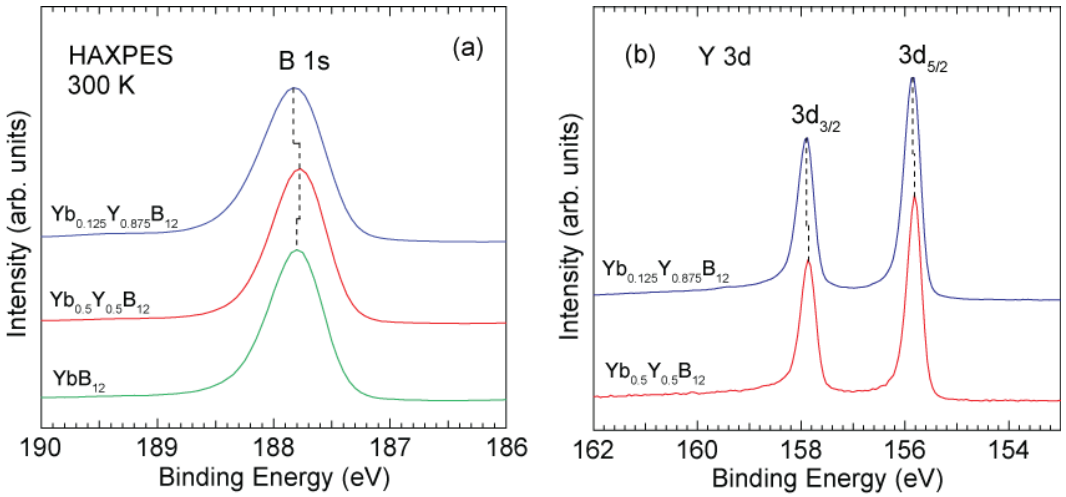

Figure 4.9: Y-concentration dependences of (a) B 1*s* and (b) Y 3*d* HAXPES spectra of $Yb_{1-x}Y_xB_{12}$ measured at 300 K.

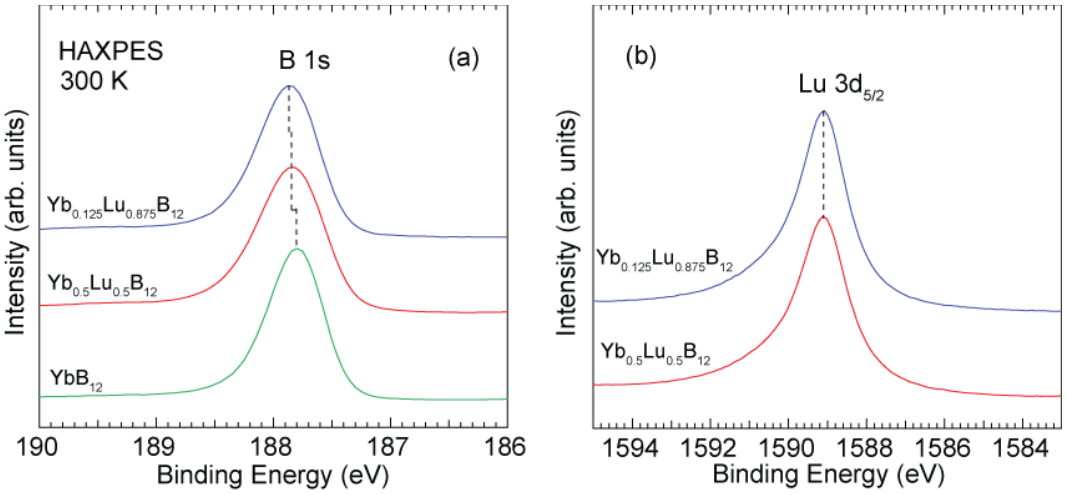

Figure 4.10: Lu-concentration dependences of (a) B 1*s* and (b) Lu $3d_{5/2}$ HAXPES spectra of $Yb_{1-x}Lu_xB_{12}$ measured at 300 K.

In order to investigate the charge distribution of the conduction electrons around the B, Y and Lu atoms, we measured B 1*s*, Y 3*d* and Lu $3d_{5/2}$ HAXPES spectra at 300 K. The Y-concentration dependences of B 1*s* and Y 3*d* HAXPES spectra are shown in Figs. 4.9 (a) and (b), respectively. The B 1*s* peak of YbB_{12} is located at 187.82 eV and is slightly shifted to higher E_B side with Y-doping for x=0.875. The Y $3d_{3/2}$ and $3d_{5/2}$ peaks of $Yb_{0.5}Y_{0.5}B_{12}$ observed at 155.82 and 157.87 eV, respectively, also slightly shift to deeper E_B side for x=0.875. For comparison, Lu-concentration dependences of B 1*s* and Lu $3d_{5/2}$ HAXPES spectra of $Yb_{1-x}Lu_xB_{12}$ are shown in Figs. 4.10 (a) and (b), respectively. The B 1*s* spectra also slightly shift to lower E_B side as observed in $Yb_{1-x}Y_xB_{12}$. On the other hand, we

find no energy shifts in Lu $3d_{5/2}$ spectra at 1589.1 eV. We assume this kind of energy shifts are originated from the conduction electron transferred mainly from the B site to Yb site. Consequently, it leads to decrease of Yb valence and simultaneously induces the chemical shifts in the B 1*s*, Y 3*d* and Lu $3d_{5/2}$ levels toward lower E_B.

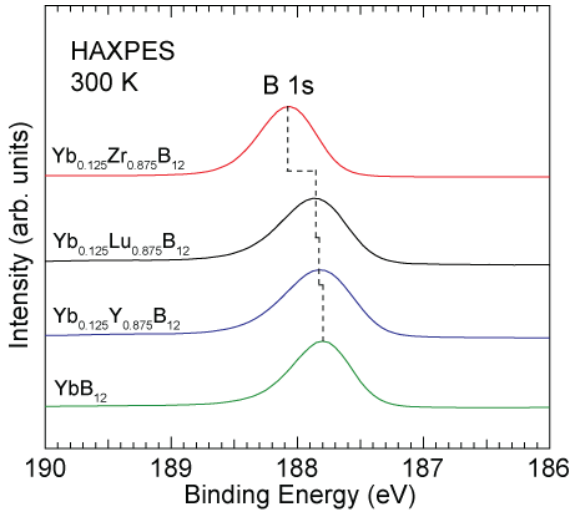

Figure 4.11: B 1*s* HAXPES spectra of YbB_{12}, $Yb_{0.125}R_{0.875}B_{12}$ and $Yb_{0.125}Zr_{0.875}B_{12}$ measured at 300 K.

We compare the B 1*s* HAXPES spectra of YbB_{12}, $Yb_{0.125}R_{0.875}B_{12}$ and $Yb_{0.125}Zr_{0.875}B_{12}$ measured at 300 K in Fig. 4.11. The B 1*s* peak slightly shifts to higher E_B side with Y and Lu-doping, and, in particular, largely shifts with Zr-doping. The larger change for the Zr-doping samples is also observed for the Yb valence (Fig. 4.7 (a)). Note that the nominal valences of R are trivalent while that of Zr is trivalent. Since the Yb valence in YbB_{12} is close to trivalent, the Zr substitution works as the electron doping, while the number of the conduction electrons are almost unchanged with the R substitution. The larger changes in the Yb valence and B 1*s* peak shift for Zr-doping samples compared to the R-doping samples are well described as the results of the electron doping. The slight-change in the Yb valence and B 1s peak shift of $Yb_{0.125}R_{0.875}B_{12}$ suggest the charge transfer from the B site to Yb site.

4.4 Results of LEPES

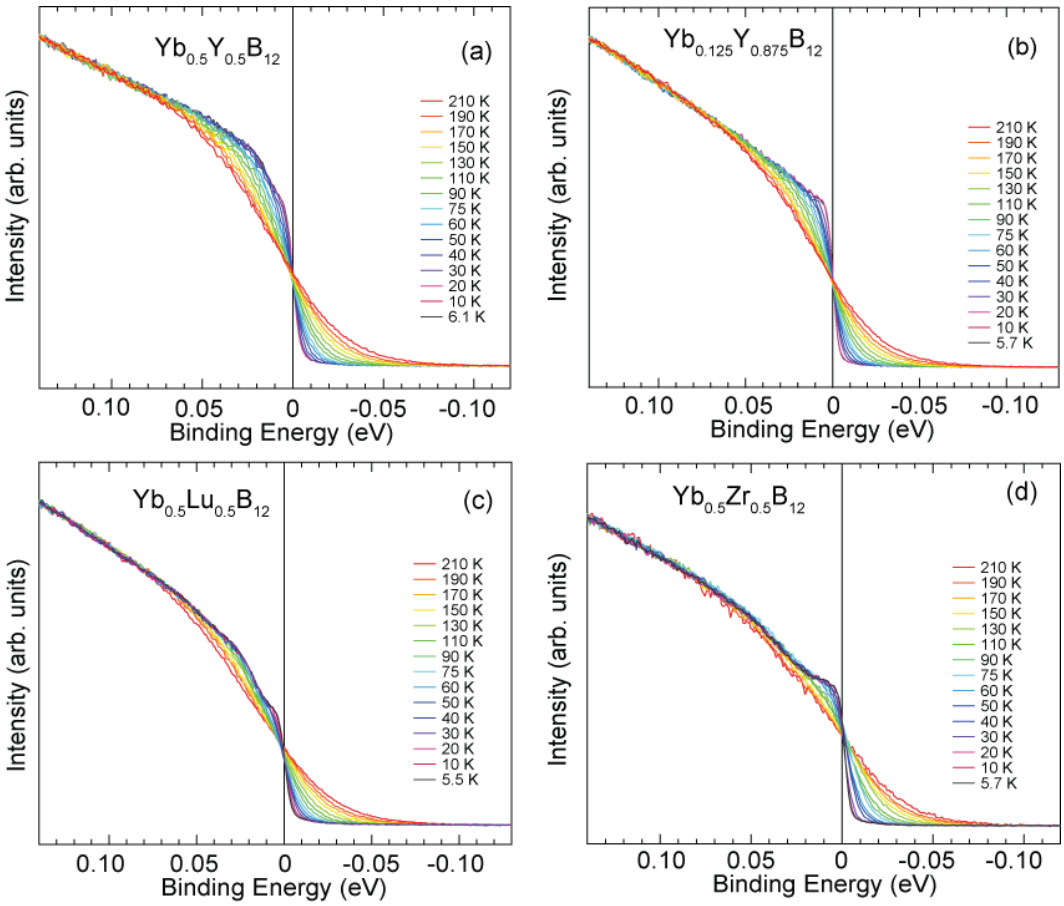

Figure 4.12: Temperature dependent LEPES spectra of (a) $Yb_{0.5}Y_{0.5}B_{12}$, (b) $Yb_{0.125}Y_{0.875}B_{12}$, (c) $Yb_{0.5}Lu_{0.5}B_{12}$ and (d) $Yb_{0.5}Zr_{0.5}B_{12}$ taken at 7 eV.

In order to investigate the evolution of the pseudo gap, we performed LEPES measurements on $Yb_{1-x}R_xB_{12}$. Figures 4.12 (a), (b), (c) and (d) show the temperature dependences of LEPES spectra of $Yb_{0.5}Y_{0.5}B_{12}$, $Yb_{0.125}Y_{0.875}B_{12}$, $Yb_{0.5}Lu_{0.5}B_{12}$ and $Yb_{0.5}Zr_{0.5}B_{12}$ taken at 7 eV from 210 to 6 K, respectively. The spectra were normalized with the spectral intensity around 0.14 eV where the spectra show no temperature dependence and the thermal effect is negligible. In these spectra, the *c-f* hybridization peak at 15 meV and Yb^{2+} $4f_{7/2}$ peak at 45 meV are not observed, which are clearly seen in the LEPES spectra of YbB_{12} (Fig. 3.14 (a)), we notice some differences of the spectral feature near E_F among those spectra.

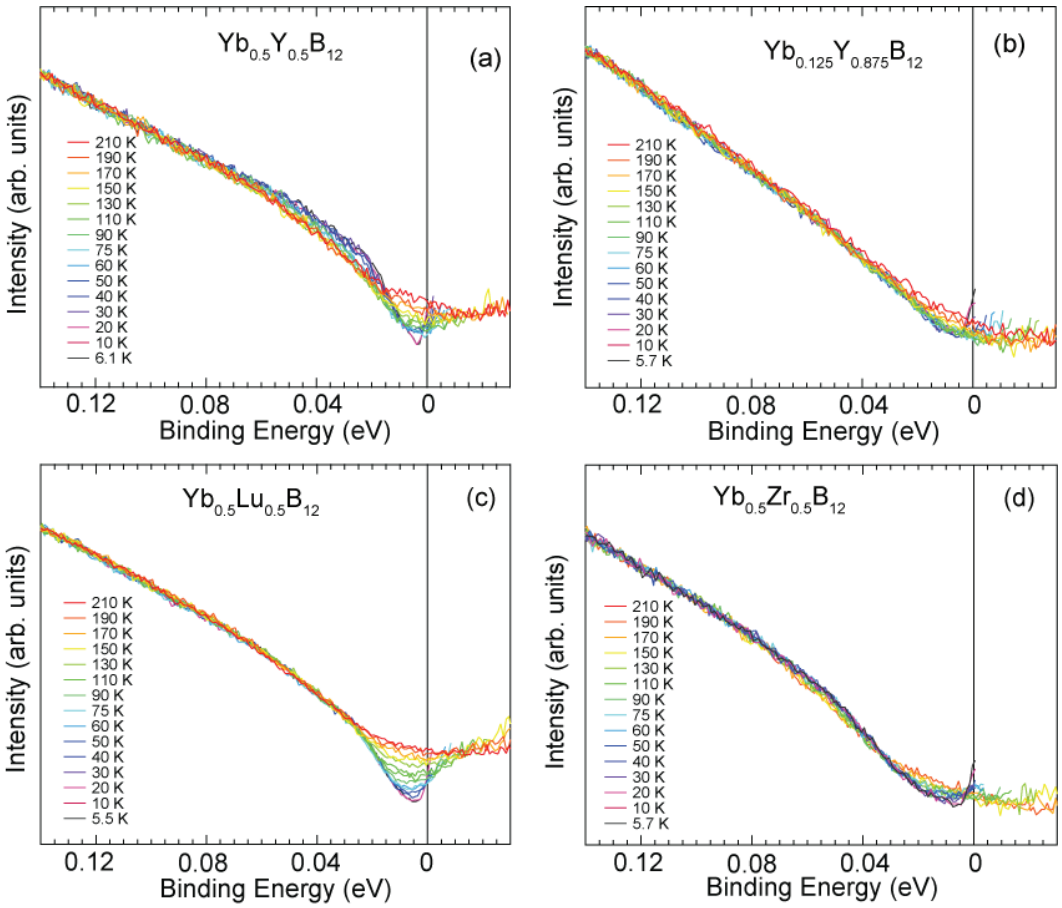

Figures 4.13: Spectral DOS of (a) $Yb_{0.5}Y_{0.5}B_{12}$, (b) $Yb_{0.125}Y_{0.875}B_{12}$, (c) $Yb_{0.5}Lu_{0.5}B_{12}$, and (d) $Yb_{0.5}Zr_{0.5}B_{12}$ obtained from Fig. 4.12.

In order to further discuss on the doping and temperature dependences of the pseudo gap, the spectral DOS of $Yb_{1-x}R_xB_{12}$ were obtained by dividing the LEPES spectra by a Gaussian-broadened Fermi-Dirac distribution function. The results are displayed in Fig. 4.13. In the $Yb_{0.5}Y_{0.5}B_{12}$ spectra (Fig. 4.13 (a)), the spectral weight near E_F decreases from ~130 K and it reflects the pseudo gap opening. With increasing the Y-concentration to 0.875, the spectral weight is almost recovered and the pseudo gap is closed (Fig. 4.13 (b)). Figure 4.13 (c) shows the spectral DOS of $Yb_{0.5}Y_{0.5}B_{12}$ and we can see the pseudo gap opening. In contrast, as discussed in Chapter 3, in $Yb_{0.5}Zr_{0.5}B_{12}$ spectra (Fig. 4.13 (d)), the pseudo gap is almost closed. As discussed before, in R-doping system, the almost trivalent Yb is substituted with trivalent R, which almost does not change the number of the conduction electrons. In contrast, Zr is tetravalent, and the Zr substitution works as the electron doping. The pseudo gap is closed more rapidly for Zr-doping system than R-doping system, most likely due to larger number of conduction electrons. Therefore, we can conclude that the electron doping plays significant

role in the pseudo gap closing as well as the larger change in the Yb valence, the energy shift of the B 1*s* peak and T_{max} of the magnetic susceptibility.

4.5 Conclusion

The Yb 3*d*, valence-band, B 1*s*, Y 3*d* and Lu $3d_{5/2}$ HAXPES spectra of $Yb_{1-x}R_xB_{12}$ were measured at $\hbar\omega$=5.95 keV. Both Yb^{2+} and Yb^{3+}-derived structures are clearly seen in the Yb 3*d* spectra. The intensity of Yb^{2+} components gradually increases and that of Yb^{3+} gradually decreases with increasing *x*. The Yb valence of YbB_{12} evaluated from the Yb 3*d* spectra is 2.93 at 300 K. With R-doping, the Yb valence gradually decrease to ~2.89 for $Yb_{0.125}Y_{0.875}B_{12}$ and ~2.86 for $Yb_{0.125}Lu_{0.875}B_{12}$, respectively. The Yb valences of $Yb_{0.125}R_{0.875}B_{12}$ gradually decrease on cooling. In the valence-band HAXPES spectra at 300 K, we can clearly see the Yb^{2+} 4*f* and Yb^{3+} 4*f*-derived structures near E_F and at 6 - 12 regions, respectively. With R-doping the Yb^{3+} 4*f* multiplet structures gradually shifts to higher E_B side, which suggests the Yb 4*f* hole level gradually closer to E_F. In the B 1*s* spectra, the similar energy shifts to higher E_B side with R-doping are also observed. The chemical shifts in the core level suggest that the conduction electron is transferred mainly from B site to Yb site. The amount of the shifts are less compared to Zr-doping system, because Y and Lu is trivalent as Yb in YbB_{12}.

Temperature dependent LEPES was also performed for $Yb_{1-x}R_xB_{12}$ at 7 eV. We can clearly see the pseudo gap opening in $Yb_{0.5}Y_{0.5}B_{12}$ and $Yb_{0.5}Lu_{0.5}B_{12}$, while the gap is already closed in $Yb_{0.5}Zr_{0.5}B_{12}$. The gap is closed in $Yb_{0.125}Y_{0.875}B_{12}$. These results suggest that the electron doping plays significant role in the pseudo gap closing as well as the larger change in the Yb valence, the energy shift of the B 1*s* peak and T_{max} of the magnetic susceptibility.

Reference:

[4.1] K. Hayashi, K. Ishii, F. Iga, T. Noguchi, T. Takabatake, A. Kondo, and K. Kindo, JPS Conf. Proc. **3**, 011050 (2014).

[4.2] F. Iga, M. Kasaya, and T. Kasuya, J. Magn. Magn. Mat. **76**, 156 (1988).

[4.3] F. Iga, N. Shimizu, and T. Takabatake, J. Magn. Magn. Mater. **177**, 337 (1998).

[4.4] S. Ueda, Y. Katsuya, M. Tanaka, H. Yoshikawa, Y. Yamashita, S. Ishimaru, Y. Matsushita, and K. Kobayashi, AIP Conf. Proc. **1234**, 403 (2010).

[4.5] K. Kobayashi, M. Yabashi, K. Tamasaku, D. Miwa, T. Ishikawa H. Nohira, T. Hattori, Y. Sugita, O. Nakatsuka, A. Sakai, and S. Zaima, Appl. Phys. Lett. **83**, 1005 (2003).

[4.6] M. Arita, K. Shimada, H. Namatame, and M. Taniguchi, Surf. Rev. Lett. **9**, 535 (2002).

[4.7] H. Sato, K. Shimada, M. Arita, K. Hiraoka, K. Kojima, Y. Takeda, K. Yoshikawa, M. Sawada, M. Nakatake, H. Namatame, M. Taniguchi, Y. Takata, E. Ikenaga, S. Shin, K. Kobayashi, K. Tamasaku, Y. Nishino, D. Miwa, M. Yabashi, and T. Ishikawa, Phys. Rev. Lett. **93**, 246404 (2004).

[4.8] D. A. Shirley, Phys. Rev. B **5**, 12 (1972).

[4.9] Yamaguchi, A. Sekiyama, S. Imada, H. Fujiwara, M. Yano, T. Miyamachi, G. Funabashi, M. Obara, A. Higashiya, K. Tamasaku, M. Yabashi, T. Ishikawa, F. Iga, T. Takabatake, and S. Suga, Phys. Rev. B **79**, 125121 (2009).

[4.10] H. Sato, K. Yoshikawa, K. Hiraoka, M. Arita, K. Fujimoto, K. Kojima, T. Muro, Y. Saitoh, A. Sekiyama, S. Suga, and M. Taniguchi, Phys. Rev. B **69**, 165101 (2004).

[4.11] Y. Utsumi, H. Sato, S. Ohara, T. Yamashita, K. Mimura, S. Motonami, K. Shimada, S. Ueda, K. Kobayashi, H. Yamaoka, N. Tsujii, N. Hiraoka, H. Namatame, and M. Taniguchi, Phys. Rev. B **86**, 115114 (2012).

[4.12] H. Sato, Y. Utsumi, J. Kodama, H. Nagata, M. A. Avila, R. A. Ribeiro, K. Umeo, T. Takabatake, K. Mimura, S. Motonami, H. Anzai, S. Ueda, K. Shimada, H. Namatame, and M. Taniguchi, Phys. Status Solidi C **12**, 620 (2015).

Chapter 5: Photoemission study of Kondo lattices $Yb_2Pt_6X_{15}$ (X=Al, Ga)

5.1 Introduction

Yb-based Kondo lattices show a wide variety of interesting physical phenomena such as heavy fermion behavior, valence fluctuation, and superconductivity. The ground state of such systems is believed to be determined by the competition between the inter-site Ruderman-Kittel-Kasuya-Yosida (RKKY) interaction and on-site Kondo effect, both arising from the *c-f* hybridization, as discussed in Chapter 1. When the RKKY interaction is dominant, the 4*f* electrons interact indirectly with each other mediated by the conduction electrons and a magnetic ordered state is formed at low temperature. On other hand, when the Kondo effect is dominant, the 4*f* moments are screened by the conduction electrons, leading to a non-magnetic Fermi-liquid (FL) ground state. This competition between the two interactions is well described in the so-called Doniach phase diagram [5.1].

Recently, Matsumoto *et al*. successfully synthesized Yb-based Kondo lattices $Yb_2Pt_6X_{15}$ (X=Al, Ga) and their physical properties significantly change when X goes from Al to Ga [5.2, 5.3]. They have a quasi-two-dimensional $Sc_{1.2}Fe_4Si_{9.8}$-type crystal structure (space group $P6_3$ *mmmc*) as shown in Fig. 5.1(a) [5.2]. The lattice parameters of $Yb_2Pt_6Al_{15}$ are a=4.266 and c=16.361 Å, and those of $Yb_2Pt_6Ga_{15}$ are a=4.278 and c=16.637 Å, respectively. The structure consists of Yb_4X_6 and Pt_6X_{12} layers, stacking along c-axis in order of Yb_4X_6-Pt_6X_{12}-Pt_6X_{12}-Yb_4X_6. As shown in Fig. 5.1 (b), the Yb_4X_6 layers are almost planar and consist of Yb atoms arranged at hexagons centered by triangular Al_3 units. The Pt_6X_{12} layers are consist of three adjacent X_6-Pt_6-X_6 layers and the Pt_6 and X_6 layers are shown in Fig. 5.1 (c).

For $Yb_2Pt_6Al_{15}$, several transport measurements were carried out [5.3] and temperature dependent magnetic susceptibilities are shown in Fig. 5.2 (a). The magnetic susceptibility at high temperature shows the Curie-Weiss behavior with an effective magnetic moment of $\mu_{eff} \sim 4.1\ \mu_B$, close to the value of the free Yb^{3+} ion of μ_{eff}=4.54 μ_B. After getting its maximum value at $T_{max} \sim 30$ K, the

susceptibility drops and becomes almost temperature independent at lower temperature region with a non-magnetic ground state. The experimental data are well fitted with the CoqblinSchrieffer model for J=7/2 of Yb^{3+} with the Kondo temperature of T_K=64 K [5.3].

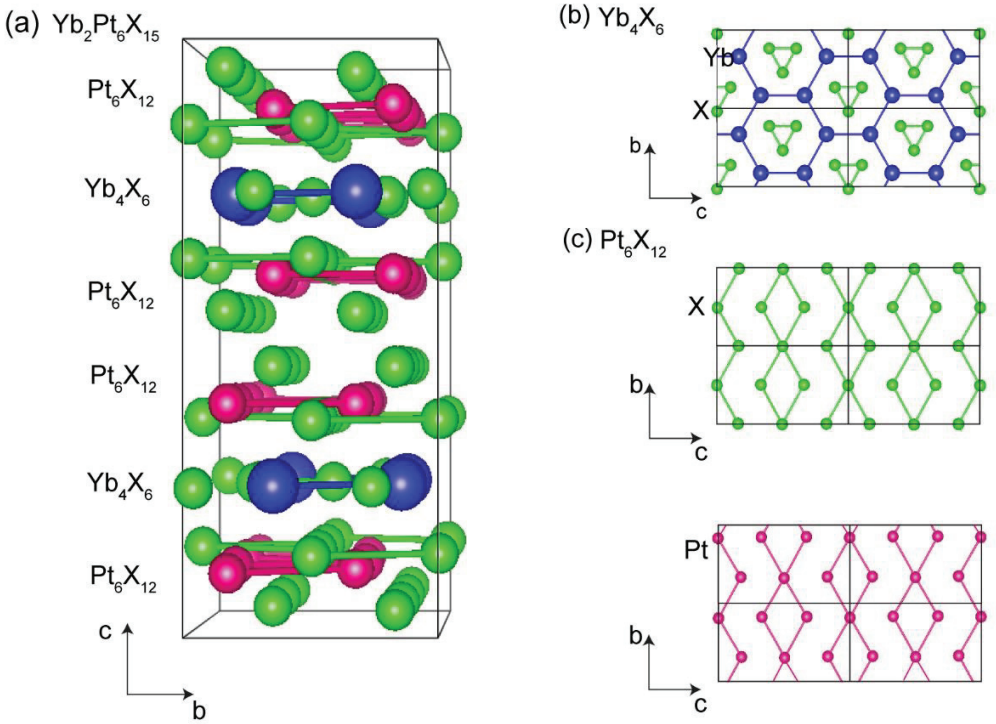

Figure 5.1. (a) $Sc_{1.2}Fe_4Si_{9.8}$-type crystal structure of $Yb_2Pt_6X_{15}$ with two kinds of layers. (b) Yb_4X_6 layer consists of Yb hexagon centered by triangular Al_3 units. (c) Pt_6X_{12} layer consists of X_6 and Pt_6 layers [5.2].

On the other hand, the physical properties of $Yb_2Pt_6Ga_{15}$ have not been reported except for the lattice constant and heat capacity measurements [5.2]. The temperature dependences of magnetic susceptibilities measured in a magnetic field of H=10 kOe for $H \| a$ and $H \| c$ directions are shown in Fig. 5.2 (a) [5.4]. The magnetic susceptibility continuously decreases from 330 K and almost becomes constant at 200 K. Below 30 K, it sharply increases most likely due to magnetic impurities, such as Yb_2O_3. T_{max} of magnetic susceptibility is above 330 K, which gives us lower limit of T_K at least 1000 K from $T_K \approx 3T_{max}$.

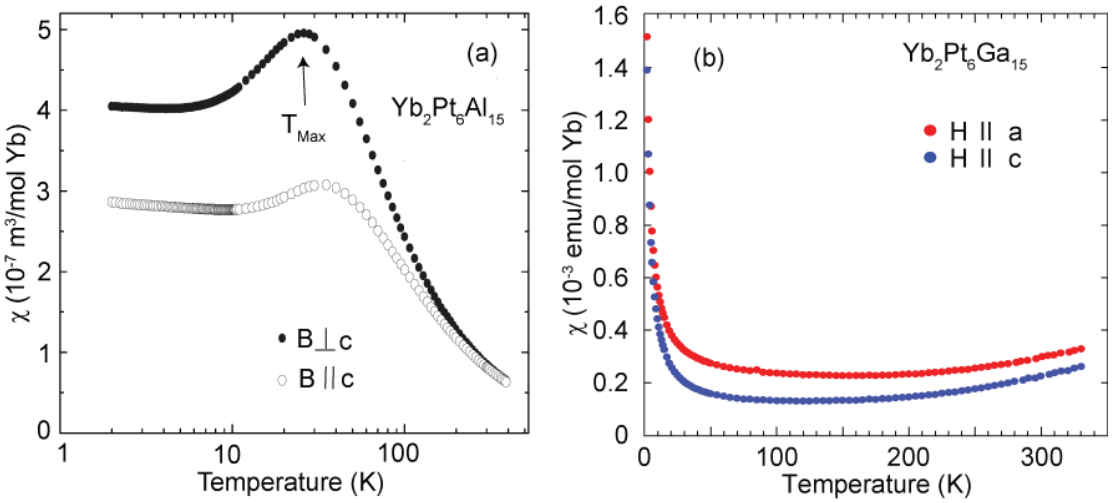

Figures 5.2. Temperature dependences of magnetic susceptibilities of (a) $Yb_2Pt_6Al_{15}$ [5.3] and (b) $Yb_2Pt_6Ga_{15}$ [5.4].

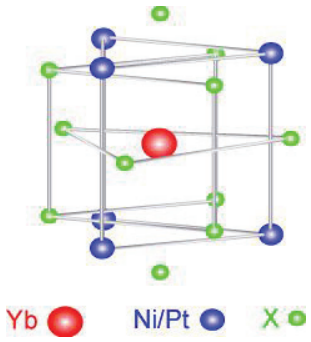

Figure 5.3: Local coordination around the Yb ion of $Yb_2Pt_6X_{15}$ and $YbNi_3X_9$.

The Al and Ga ions are isovalent and their nominal electronic configurations are Al $3s^23p^1$ and Ga $4s^24p^1$, respectively. Although they have same crystal structure with isovalent Al and Ga elements, the Kondo temperature T_K in $Yb_2Pt_6X_{15}$ is significantly changed by exchanging Ga for Al. This situation is similar to the Kondo lattices $YbNi_3X_9$ [5.5, 5.6]. Recently, Utsumi *et al*. reported hard x-ray photoemission spectroscopy (HAXPES) study on $YbNi_3X_9$ [5.7]. It has $ErNi_3Al_9$-type crystal structure and it is similar to that of $Yb_2Pt_6X_{15}$; the both systems have a layered structure with the Yb_4X_6 and Pt_6/Ni_6X_{12} layers. Moreover, the local coordination around the Yb ion in both compounds are same as shown in Fig. 5.3. The T_K-values of $YbNi_3X_9$ change from 2.7 K for $YbNi_3Al_9$ to 570 K for $YbNi_3Ga_9$ [5.5, 5.6]. $YbNi_3Al_9$ exhibits an antiferromagnetic (a chiral helical order) ground state and the Néel temperature is T_N=3.4 K [5.8], while $YbNi_3Ga_9$ exhibits valence fluctuation within the non-magnetic ground state. Thus, depending on X, $YbNi_3X_9$ is located in different phases separated by a quantum critical point (QCP)

in the Doniach phase diagram. However, the $YbNi_3Ga_9$ shows an antiferromagnetic order under 9 GPa [5.9], indicating its state being close to the QCP. Although both $Yb_2Pt_6X_{15}$ compounds are in the nonmagnetic region of the phase diagram, the X dependence of T_K indicates that $Yb_2Pt_6X_{15}$ occupy different positions; $Yb_2Pt_6Al_{15}$ is close to a magnetic phase transition, while $Yb_2Pt_6Ga_{15}$ is further away from a magnetic transition. According to T_K of $Yb_2Pt_6X_{15}$ and $YbNi_3X_9$ systems, they are located different positions in Doniach phase diagram as shown in Fig. 5.4. From $YbNi_3Al_9$ to $Yb_2Pt_6Ga_{15}$, the ground state gradually moves from magnetic to non-magnetic. This situation should be originated from the difference of their electronic structure.

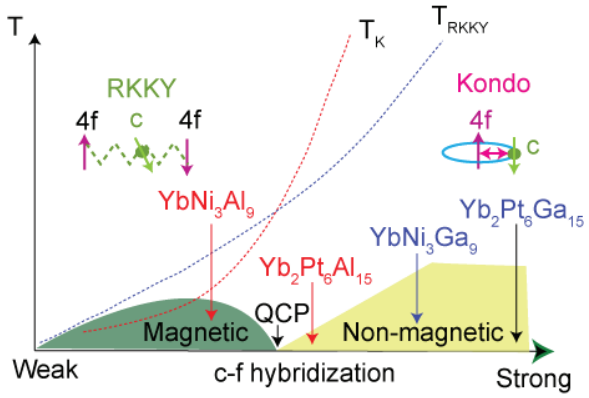

Figure 5.4: Doniach phase diagram and positions of $Yb_2Pt_6X_{15}$ and $YbNi_3X_9$ [5.1].

In this chapter, in order to investigate the electronic structure of $Yb_2Pt_6X_{15}$ in comparison with those of $YbNi_3X_9$, we performed HAXPES with $\hbar\omega$=5.95 keV, vacuum ultraviolet photoemission spectroscopy (VUVPES) with $\hbar\omega$=182 and low-energy photoemission spectroscopy (LEPES) with $\hbar\omega$=7 eV. We illustrated the differences in electronic structure of $Yb_2Pt_6X_{15}$ and $YbNi_3X_9$ by a schematic electronic model. Moreover, we performed angle-resolved photoemission spectroscopy (ARPES) with $\hbar\omega$=35 eV and successfully observed very clear band dispersion derived from the *c-f* hybridization. Based on periodic Anderson model (PAM) without taking into account the Coulomb interaction between 4*f* electrons, the *c-f* hybridization energy and mass enhancement factor were estimated.

5.2 Experiment

The HAXPES experiments for $Yb_2Pt_6X_{15}$ were performed at the undulator beamline BL15XU [5.10] of SPring-8. Synchrotron radiation was monochromatized to 5.95 keV with Si 111 double crystal and Si 333 channel-cut

monochromators [5.11]. The VUVPES, LEPES and ARPES measurements were performed at the bending beamline BL-7, the undulator beamlines BL-9A [5.12] and BL-1 [5.13] of HiSOR [5.14], respectively. The hemispherical photoelectron analyzers were used (VG Scienta R4000 at Spring8/BL-9A/BL-1 and SES 2002 at BL-7). The total energy resolution of HAXPES measurements was 240 meV and those of VUVPES, LEPES and ARPES were ~30, ~5 and ~40 meV, respectively. Binding energy (E_B) calibrated with Fermi edge of Au spectra.

Single crystals of $Yb_2Pt_6X_{15}$ (X=Al, Ga) were synthesized by means of the self-flux method. The precursor materials were mixed with molar ratio of Yb:Pt:X=1:3:30. Then the mixed materials were put in an alumina crucible and it is sealed in an evacuated quartz tube. For $Yb_2Pt_6Al_{15}$, the tube was heated to 1150 ˚C and kept for 5 hours. And then it was cooled to 850 ˚C in 1 hour, again heated to 900 ˚C in 1 hour, and cooled to 750 ˚C in 30 hours. The excess Al was removed in a centrifuge and further washed out in NaOH solution. For $Yb_2Pt_6Ga_{15}$, the tube was heated to 1100 ˚C and soaked for 5 hours, and then cooled down to 300 ˚C in 160 hours. The excess Ga was spun off in centrifuge and then washed out in distilled water [5.3]. The single phase of the grown sample was verified by x-ray powder diffraction. No diffraction due to impurity phases was detected.

5.3 Results of HAXPES and VUVPES

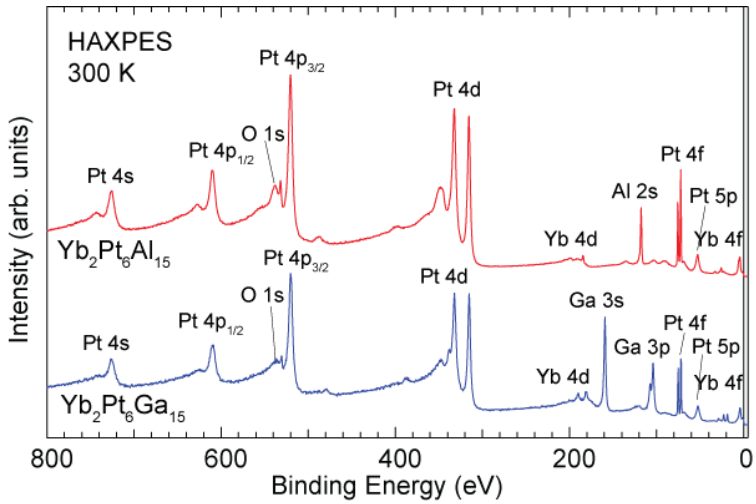

Figure 5.5: HAXPES spectra of $Yb_2Pt_6X_{15}$ in the wide energy range measured at 300 K.

The HAXPES spectra of $Yb_2Pt_6X_{15}$ in the wide energy range measured at 300 K are shown Fig. 5.5. Although the O 1*s* derived structures are observed at 531 eV,

it is negligibly small compared to the other Yb, Pt and Al/Ga derived structures. No signal due to C 1*s* is not detected. The both sample has good enough quality for the HAXPES measurement.

Figure 5.6 shows Yb 3*d* HAXPES spectra of $Yb_2Pt_6Al_{15}$ measured at 20 K. The Yb 3*d* spectra are separated into the $3d_{5/2}$ part at 1515-1540 eV and $3d_{3/2}$ part at 1560-1590 eV. We can see the Yb^{2+} 3*d* structures at ~1520 and 1570 eV as a single peak, and the Yb^{3+} 3*d* components at ~1530 and ~1576 eV as multiplet structures due to the Coulomb interaction between the 3*d*-photohole and Yb^{3+} 4*f* hole in the $3d^9 4f^{13}$ final state. The intense peak due to Al 1*s* core states is visible at 1559.5 eV and the tail strongly disturbs the spectral feature in the $3d_{3/2}$ region. Therefore, we only measured the Yb $3d_{5/2}$ region below 1545 eV for $Yb_2Pt_6Al_{15}$.

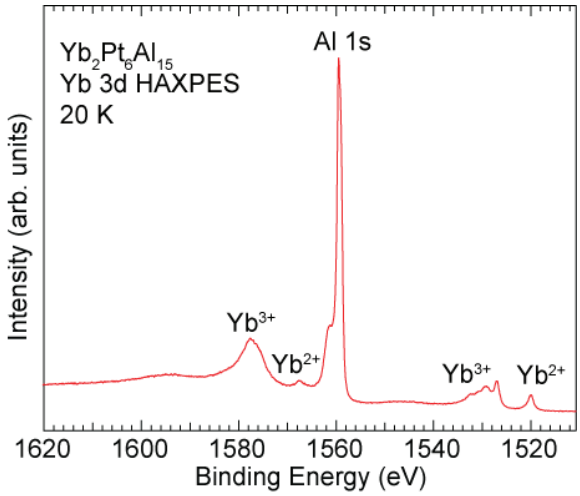

Figure 5.6: Yb 3*d* HAXPES spectra of $Yb_2Pt_6Al_{15}$ measured at 20 K.

Temperature dependent Yb 3*d* HAXPES spectra of $Yb_2Pt_6Al_{15}$ and $Yb_2Pt_6Ga_{15}$ are displayed in Figs. 5.7 (a) and 5.7 (b), respectively. The Yb $3d_{5/2}$ spectra of $Yb_2Pt_6Al_{15}$ exhibit clear temperature dependence between 250 and 20 K. The spectral feature is similar to that of other Yb compounds [5.7,5.15]. The Yb^{2+} single peak at 1520 eV gradually increases with decreasing temperature. In contrast, the Yb^{3+}-derived multiplet structures at 1524-1536 eV are gradually reduced. The temperature dependence of the spectra indicates that the Yb valence is gradually shifted to the divalent side on cooling, which is a clear evidence of valence fluctuation in $Yb_2Pt_6Al_{15}$.

In contrast, the temperature dependence of the Yb 3*d* spectra of $Yb_2Pt_6Ga_{15}$ is much weaker as seen from Fig. 5.7 (b). The $3d_{3/2}$ region is also divided into the Yb^{2+} peak at 1568 eV and Yb^{3+} multiplet structures at 1574-1582 eV. The intensities of the Yb^{3+} structures are significantly weak compared to the Yb^{2+}

peaks, indicating the Yb-ion in $Yb_2Pt_6Ga_{15}$ is closer to divalent. The tiny peaks shown by the vertical bars at 1537 and 1584 eV come from the Yb^{2+}-derived plasmon satellites [5.7]. In this case, we cannot observe Yb^{3+}-derived plasmon satellite structures as in $Yb_{1-x}Zr_xB_{12}$ in Chapter 3, because of the small amount of Yb^{3+}.

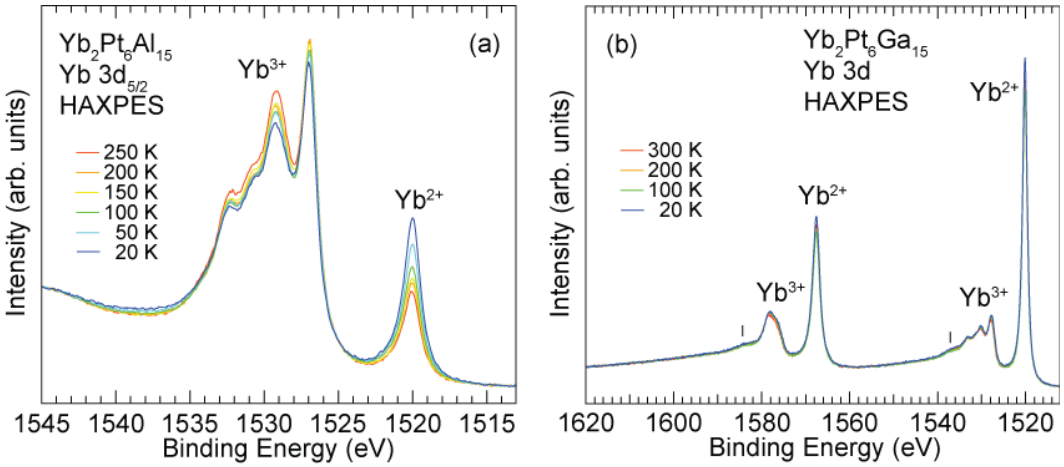

Figure 5.7: (a) Temperature dependence of Yb $3d_{5/2}$ HAXPES spectra of $Yb_2Pt_6Al_{15}$ measured between 250 and 20 K. (b) Temperature dependence of Yb $3d$ HAXPES spectra of $Yb_2Pt_6Ga_{15}$ measured between 300 and 20 K. Vertical bars indicate the plasmon satellite structures.

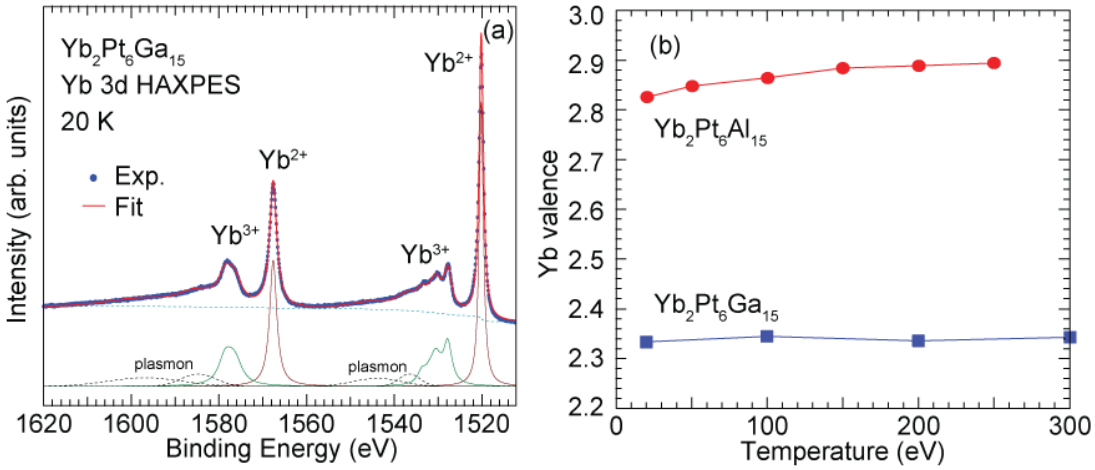

Figures 5.8: (a) Fit of Yb $3d$ HAXPES spectrum of $Yb_2Pt_6Ga_{15}$ measured at 20 K. (b) Yb valences of $Yb_2Pt_6X_{15}$ estimated from the fits of the spectra as a function of temperature.

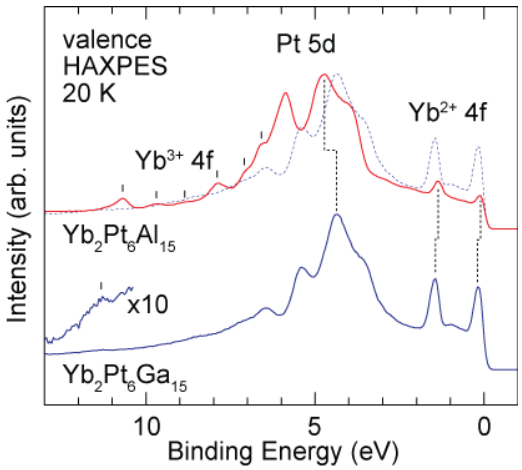

Figure 5.9: Valence-band HAXPES spectra of $Yb_2Pt_6X_{15}$ measured at 20 K. The dashed line on the spectrum of $Yb_2Pt_6Al_{15}$ represents that of $Yb_2Pt_6Ga_{15}$ for comparison.

Since the Yb^{2+} and Yb^{3+}-derived structures are clearly resolved in the Yb 3*d* spectrum, the Yb valence can precisely be estimated from their relative intensity. In order to evaluate Yb valence, we carried out the fits of the Yb 3*d* spectra. Figure 5.8 (a) shows an example of the fitting result for $Yb_2Pt_6Ga_{15}$ at 20 K. The detailed fitting procedures were already explained in Chapter 3. The evaluated Yb valences of $Yb_2Pt_6X_{15}$ are summarized in Fig. 5.8 (b). The Yb valence of $Yb_2Pt_6Al_{15}$ is 2.89 at 250 K and gradually decreases on cooling to 2.83 at 20 K. On the other hand, the valence of $Yb_2Pt_6Ga_{15}$ is 2.34 at 300 K and it is almost constant in the whole temperature region. The different temperature dependence of the valence in the two compounds can be understood from their different T_K. According to theoretical calculation using the non-crossing approximation, the Yb valence changes significantly around T_K [5.17]. Since T_K of $Yb_2Pt_6Al_{15}$ is ~60 K [5.3], its valence changes within the measured temperature region, while the Yb valence of $Yb_2Pt_6Ga_{15}$ with T_K > 1000 K is almost constant below 300 K [5.4]. The constant Yb valence (~2.2) below 300 K is also reported for $YbAl_2$ with T_K = 2000 - 2600 K [5.18].

In order to investigate the electronic states near Fermi level (E_F) including the Yb 4*f* states, we measured the valence-band HAXPES spectra of $Yb_2Pt_6X_{15}$ as shown in Fig. 5.9. A dashed line on the spectrum of $Yb_2Pt_6Al_{15}$ represents that of $Yb_2Pt_6Ga_{15}$ normalized with the intense peak at 4-5 eV for comparison. Taking into account the photoionization cross sections at $\hbar\omega$=6 keV [5.19], the spectra are mainly derived from the Pt 5*d*, Yb 4*f*, Ga 4*s* and Al 3*s* states with ratio of 14.5 : 2.6 : 3.3: 1. Note that the delocalized *s* states distribute in the wide E_B range, while the localized *d* and *f* states in the narrow E_B range. The strongest structures at 3 - 6

eV are assigned to the Pt 5*d* states. The Yb^{2+} $4f_{7/2}$ and $4f_{5/2}$ states are observed in the vicinity of E_F and 1.3 eV, respectively. The Yb^{2+} 4*f* peaks of $Yb_2Pt_6Al_{15}$ have higher intensity compared to those of $Yb_2Pt_6Ga_{15}$, reflecting an almost trivalent Yb ion of $Yb_2Pt_6Al_{15}$. On the other hand, the Yb^{3+} 4*f* multiplet structures, caused by Yb^{3+} 4*f* photoemission final states with $4f^{12}$ electronic configurations, are buried in the intense Pt 5*d* peak above 5 eV. Some Yb^{3+} 4*f* peaks are observed in the $Yb_2Pt_6Al_{15}$-spectrum as indicated by vertical bars. Almost no structure is found in the $Yb_2Pt_6Ga_{15}$-spectrum in the corresponding region, reflecting that the Yb valence is close to divalent. Only one peak is very weakly detected at 11.3 eV as we see in the enlarged spectrum in Fig. 5.9. This peak is considered to corresponds to the peak at 10.7 eV in the $Yb_2Pt_6Al_{15}$-spectrum.

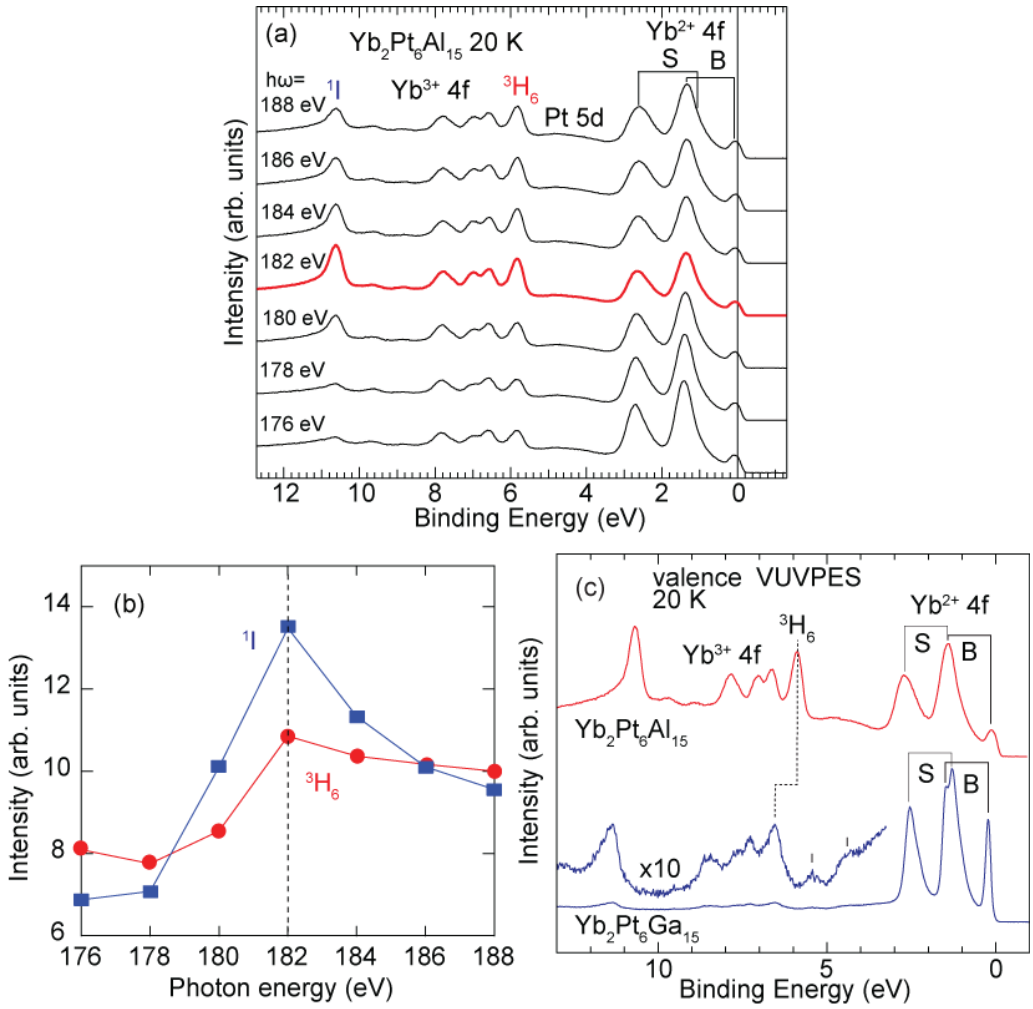

Figures 5.10: (a) Valence-band VUVPES spectra of $Yb_2Pt_6Al_{15}$ measured at 20 K between $\hbar\omega$=176 - 188 eV. The bulk and surface Yb^{2+} 4*f* components are indicated with "B" and "S", respectively. (b) The intensities of $^3H_6$ and ^1I peaks as a function of photon energy. (c) Valence-band VUVPES spectra of $Yb_2Pt_6X_{15}$

measured at 20 K and $\hbar\omega$=182 eV, just at Yb 4*d*-4*f* resonance energy. Two peaks of the enlarged spectrum of $Yb_2Pt_6Ga_{15}$ shown by vertical bars correspond to Pt 5*d* peak in the HAXPES spectrum.

In order to clearly detect the Yb^{3+} 4*f* multiplet structures, we measured valence-band VUVPES spectra for $Yb_2Pt_6Al_{15}$ at $\hbar\omega$=176 - 188 eV in Fig. 5.10 (a). As the valence-band HAXPES spectra, the valence-band VUVPES spectra shows Yb^{2+} and Yb^{3+}-derived structures. The Yb^{2+} 4*f* peaks are observed near E_F and the Yb^{3+} 4*f* multiplet structures are seen at 5 - 12 eV. Because of the much reduced inelastic mean free path of photoelectrons for VUVPES compared to that of HAXPES, the surface components are observed in the Yb^{2+} 4*f* spectra. The Yb^{2+}-derived surface state components are located deeper E_B than the bulk components and they are observed in the valence-band VUVPES spectra as indicated in Fig. 5.10 (a), which will be again described later. Moreover, the intensity of the Yb^{3+} 4*f* multiplet structures are significantly enhanced with increasing photon energy from $\hbar\omega$=176 eV and they get maximum intensity at $\hbar\omega$=182 eV. Figure 5.10 (b) shows the intensity of the shallowest ($^3H_6$) and the deepest (^1I) peaks of Yb^{3+} 4*f* multiplet structures as a function of photon energy. With increasing the photon energy from $\hbar\omega$=176 eV, the intensity of these peaks gradually increases and reaches maximum value with $\hbar\omega$=182 eV. The enhancement takes place due to the Yb 4*d*-4*f* resonance effect [5.20]

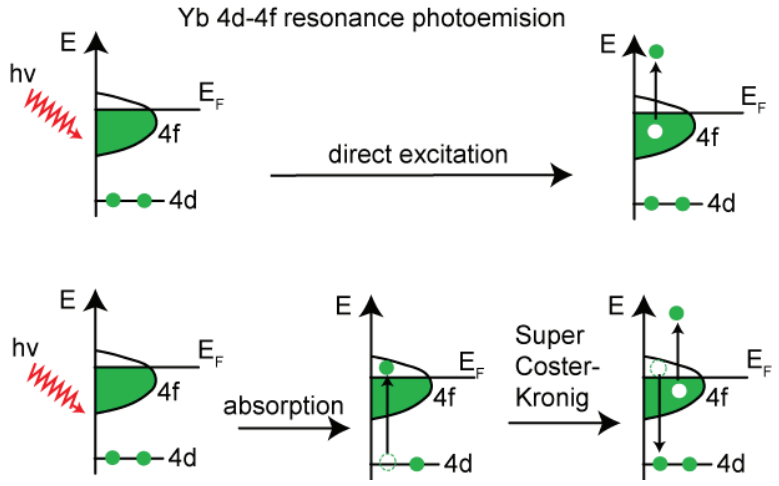

Figure 5.11: Schematic image of Yb 4*d*-4*f* resonance PES.

Figure 5.11 shows schematic image of the Yb 4*d*-4*f* resonance process. In off resonance case, the 4*f* electron directly excited from $4d^{10}4f^{13}$ initial state to $4d^{10}4f^{12}$ final state. When adjusting the photon energy to near 180 eV which is close to the energy difference between the 4*d* and 4*f* level, one of the 4*d* electrons is excited to 4*f* hole state by 4*d*-4*f* absorption, where the $4d^{10}4f^{13}$ is initial state and

$4d^9 4f^{14}$ is intermediate state. After the absorption, the 4*f* electron fills the 4*d* hole, and at the same time, one of 4*f* electron is excited to vacuum level by super Coster-Kronig process. The final state is $4d^{10}4f^{12}$ and it is same as that of direct excitation process. The two processes interference each other and the Yb^{3+} 4*f* structure is enhanced.

The VUVPES spectra of $Yb_2Pt_6X_{15}$ are compared in Fig. 5.10 (c). The all features of the Yb^{3+} 4*f* multiplet structures of $Yb_2Pt_6Al_{15}$ including the relative intensity are consistent with that observed for other Yb compounds [5.21]. The shallowest peak at 5.8 eV, which is completely overlapped with the Pt 5*d* peak in the HAXPES spectrum in Fig. 5.9, corresponds to the $^3H_6$ multiplet. Although the Yb^{3+} 4*f* structures are still weak in the $Yb_2Pt_6Ga_{15}$-spectrum, those are clearly observed in the enlarged spectrum. A peak at 6.5 eV corresponds to the $^3H_6$ multiplet and a peak at 11.3 eV corresponds to the 10.7 eV (^1I) peak in the $Yb_2Pt_6Al_{15}$-spectrum.

The Yb^{2+} 4*f* region between E_F and 3.5 eV in the Yb 4*d*-4*f* resonance spectra in Fig. 5.10 (c) is composed of the surface components as well as the bulk components. The peak just below E_F is due to bulk Yb $4f_{7/2}$ states as observed in the bulk-sensitive HAXPES spectra in Fig. 5.9. In contrast, the peak around 2.5 - 3.0 eV is due to surface $4f_{5/2}$ states. The bulk $4f_{5/2}$ and surface $4f_{7/2}$ states contribute to the structure around 1.3 eV and are resolved in the case of $Yb_2Pt_6Ga_{15}$; the shallower peak at 1.3 eV is derived from the surface $4f_{7/2}$ states and the shoulder at 1.45 eV from the bulk $4f_{5/2}$ states.

There is almost no structure around 5 eV in the Yb 4*d*-4*f* resonance spectra in Fig. 5.10 (c). As indicated by vertical bars in the enlarged spectrum of $Yb_2Pt_6Ga_{15}$, the two peaks are detected at corresponding energies of the Pt 5*d* attributed peaks in the HAXPES spectrum in Fig. 5.9. Already in the off resonant case, the contribution by the Pt 5*d*, Ga 4*s* and Al 3*s* states to the valence band VUVPES spectra is less than 5% compared to Yb 4*f* at $\hbar\omega$=180 eV [5.22]. The Yb 4*f* signal is further increased by the resonant condition, making Yb 4*f* the dominant contribution to the valence-band spectra at this photon energy. The VUVPES therefore clarifies that the most noticeable peak at 3 - 6 eV in the HAXPES spectra is originated from the Pt 5*d* states. By the comparison between HAXPES and VUVPES spectra, thus, we can clearly specify the Yb^{3+} 4*f* and Pt 5*d* peaks in the valence bands.

The Yb^{2+} 4*f* peaks of $Yb_2Pt_6Ga_{15}$ are located away from E_F compared to $Yb_2Pt_6Al_{15}$. The Yb^{2+} $4f_{7/2}$ peak is assigned to the so-called Kondo peak, the deeper E_B reflects the higher T_K in $Yb_2Pt_6Ga_{15}$ because the E_B of $4f_{7/2}$ is roughly

equal to $k_B T_K$. The peak position of 0.18 eV corresponds to T_K ~2100 K. The Yb^{3+} 4*f* multiplet structures for $Yb_2Pt_6Ga_{15}$ are also shifted to deeper E_B by ΔE_B = 0.6 eV. Its energy position is related to the Yb^{3+} 4*f* hole level (ε_f) above E_F as discussed in Chapter 3. In the multi-electron picture, $\varepsilon_f > 0$ corresponds to the energy for $f^{13} \rightarrow f^{14}$ transition and the Yb^{3+} 4*f* peaks in the photoemission spectra ($f^{13} \rightarrow f^{12}$ transition) are roughly located at $-\varepsilon_f + U$ with U being the Coulomb repulsion energy between the 4*f* holes in the f^{12} final states. Since U is expected to be almost intra-atomic and unchanged for $Yb_2Pt_6X_{15}$, the deeper E_B of the Yb^{3+} 4*f* peaks for $Yb_2Pt_6Ga_{15}$ suggests smaller ε_f, that is, the Yb^{3+} 4*f* hole level being closer to E_F. This observation is consistent with the nearly divalent Yb in $Yb_2Pt_6Ga_{15}$ because of the smaller energy required for the transfer of the conduction electrons to the Yb^{3+} 4*f* hole. In the Pt 5*d* peak a shift to shallower E_B by ΔE_B = 0.3 eV is detected for $Yb_2Pt_6Ga_{15}$.

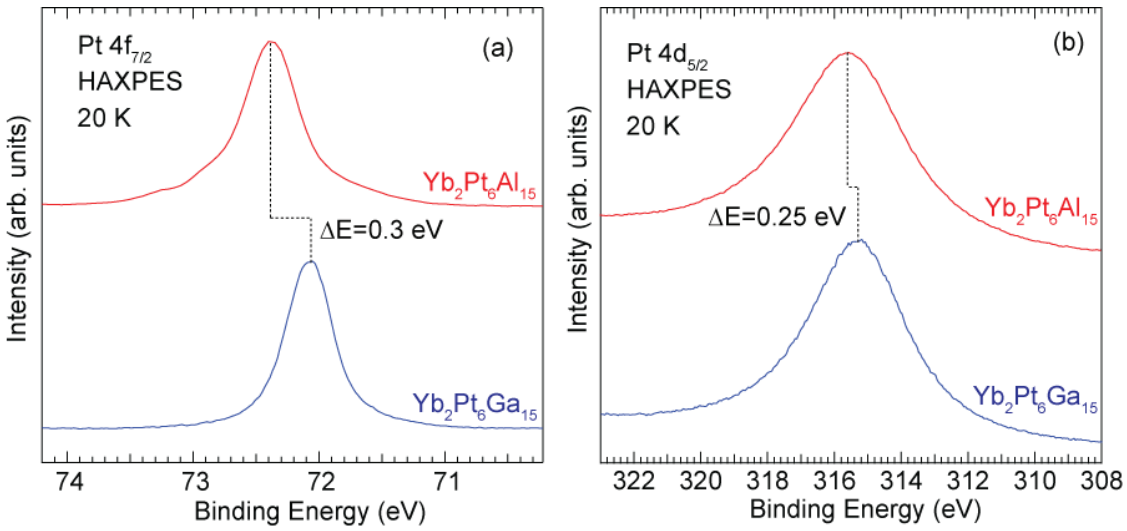

Figure 5.12: (a) Pt $4f_{7/2}$ and (b) Pt $4d_{5/2}$ HAXPES spectra of $Yb_2Pt_6X_{15}$ measured at 20 K.

In order to investigate the X-dependence of the conduction states from the peak shifts of the core levels, we measured the Pt $4f_{7/2}$ and Pt $4d_{5/2}$ HAXPES spectra of $Yb_2Pt_6X_{15}$ at 20 K as shown in Fig. 5.12 (a) and (b), respectively. Because of their spectral line width is sufficiently narrow, the peak shift is clearly detected. The Pt $4f_{7/2}$ and $4d_{5/2}$ peaks of $Yb_2Pt_6Ga_{15}$ are located at 72.0 and 315.3 eV, respectively, those of $Yb_2Pt_6Al_{15}$ are shifted deeper E_B side by ΔE_B=0.3 and 0.25 eV, respectively. The direction of the energy shifts are the same as observed for the Pt 5*d* peaks in Fig. 5.9 and their amounts are comparable, which indicate that the E_F-position of the conduction-band DOS moves to the lower energy side on going from $Yb_2Pt_6Al_{15}$ to $Yb_2Pt_6Ga_{15}$.

5.4 Results of LEPES

Figure 5.13 shows temperature dependent LEPES spectra of $Yb_2Pt_6X_{15}$ measured with $\hbar\omega$=7 eV. The spectra have been normalized using spectral intensity around 0.4 eV for $Yb_2Pt_6Al_{15}$ and 0.6 eV for $Yb_2Pt_6Ga_{15}$, respectively, where the spectra show no temperature dependence, and the thermal effect is negligible. Since the photoionization cross section of Yb 4*f* states is negligible at photon energy $\hbar\omega$=7 eV, the LEPES spectra mainly reflects conduction-band (CB) states [5.22,5.23]. In LEPES spectra of $Yb_2Pt_6Al_{15}$, the Kondo peak is clearly seen below 60 K at ~40 meV as shown a vertical bar in Fig. 5.13 (a). It gradually shifts to E_F side and its intensity slightly increases on cooling. At 10 K, the peak position is 20 meV, corresponding to T_K~230 K, higher than 64 K [5.2]. As shown in Fig. 5.13 (b), the Kondo peak of $Yb_2Pt_6Ga_{15}$ is prominently observed at ~0.2 eV at 300 K and its position almost unchanged on cooling. This value is consistent with Yb^{2+} $4f_{7/2}$ peak energy in the HAXPES spectra in Fig. 5.9. These results are consistent with HAXPES results that the Yb valence of $Yb_2Pt_6Al_{15}$ is close to trivalent with temperature dependence, while that of $Yb_2Pt_6Ga_{15}$ is closer to divalent without temperature dependence, as shown in Fig. 5.8 (b).

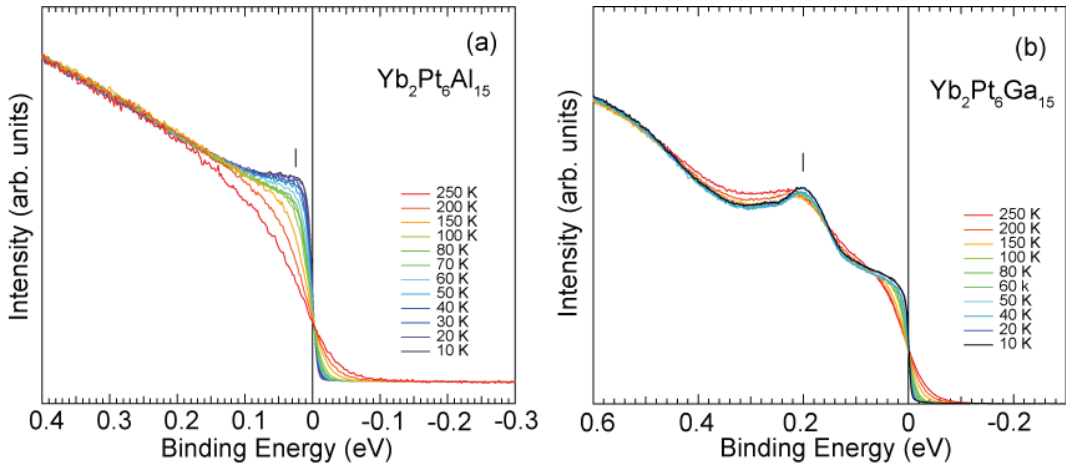

Figure 5.13: Temperature dependences of LEPES spectra of (a) $Yb_2Pt_6Al_{15}$ and (b) $Yb_2Pt_6Ga_{15}$ measured at $\hbar\omega$=7 eV.

5.5 Comparison with $YbNi_3X_9$

The HAXPES results obtained for $Yb_2Pt_6X_{15}$ are comparable with those previously reported for $YbNi_3X_9$ [5.7] with the similar X-dependence of T_K; 570

K for $YbNi_3Ga_9$ and 2.7 K for $YbNi_3Al_9$ [5.5, 5.6]. Note again that $Yb_2Pt_6X_{15}$ and $YbNi_3X_9$ possess similar crystal structures and local coordinate around the Yb-ion. Yb 3*d* HAXPES revealed that $YbNi_3Ga_9$ exhibits strong valence fluctuation behavior and the Yb valence is estimated to be 2.59 at 300 K with a decrease on cooling to 2.43 at 22 K. The valence of $YbNi_3Al_9$ is nearly 3 (~2.97) with little temperature dependence. In both systems, $Yb_2Pt_6X_{15}$ and $YbNi_3X_9$, the valence is shifted to the divalent side with exchanging Al to Ga.

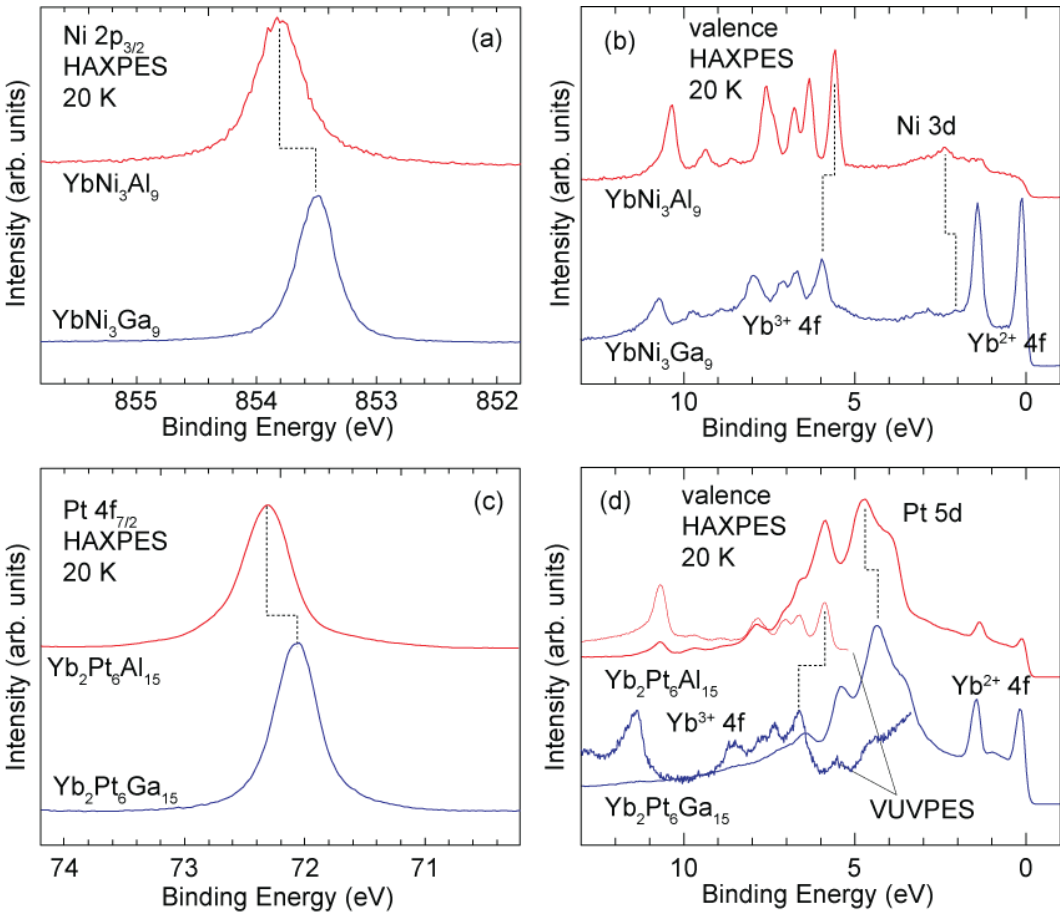

Figure 5.14: Comparison of HAXPES spectra measured at 20 K between $Yb_2Pt_6X_{15}$ and $YbNi_3X_9$. (a) Ni $2p_{3/2}$ and (b) Valence-band spectra of $YbNi_3X_9$ [5.7], and (c) Pt $4f_{7/2}$ and (d) valence-band spectra of $Yb_2Pt_6X_{15}$. The thin lines in (d) depict VUVPES spectra in the Yb^{3+} 4*f* region.

Again, similar X-dependences are observed in the core level and valence-band HAXPES spectra as well as the Yb valence for $Yb_2Pt_6X_{15}$ and $YbNi_3X_9$. Figures 5.14 (a) and 5.14 (b) exhibit the Ni $2p_{3/2}$ and valence-band spectra of $YbNi_3X_9$, respectively [5.7], and Figs. 5.14 (c) and 5.14 (d) the Pt $4f_{7/2}$ and valence-band spectra of $Yb_2Pt_6X_{15}$ for comparison. The Ni $2p_{3/2}$ peak of $YbNi_3Ga_9$ is shifted to

shallower E_B by ΔE_B = 0.3 eV and the energy shift to the same direction is observed in the Ni 3*d* peak within the valence bands. By contrast, the Yb^{3+} 4 *f* multiplet structures exhibit an opposite energy shift by ΔE_B = 0.4 eV. From their HAXPES results, Utsumi *et al.* described the X-dependence of physical properties of $YbNi_3X_9$ by the differences of the Ni 3*d* DOS at E_F and the Yb^{3+} 4*f* hole level relative to E_F [5.7]. The increased Ni 3*d* DOS at E_F and the 4*f* hole level closer to E_F for $YbNi_3Ga_9$ enhance the *c-f* hybridization, that is, an increase of T_K and induce the strong valence fluctuation.

The X-dependence of the Yb valence and the energy shifts in the Pt 4*f*, Pt 5*d* and Yb^{3+} 4*f* peaks found for $Yb_2Pt_6X_{15}$ are similar to those for $YbNi_3X_9$ [5.7]. For both case, the substitution of X-ion from Al to Ga decreases the Yb valence, and shifts the Pt 4*f* snd Pt 5*d* (Ni $2p_{3/2}$ and Ni 3*d*) peaks toward shallower E_B and the Yb^{3+} 4*f* peaks deeper E_B. In line with the argument for $YbNi_3X_9$ [5.7], the increased Pt 5*d* DOS at E_F and Yb^{3+} 4*f* hole level closer to E_F for $Yb_2Pt_6Ga_{15}$ increases the *c-f* hybridization and T_K, and decreases the Yb valence. Although the Pt 5*d* states mainly distribute at 3-6 eV in Fig. 5.14 (d), we can see that the Pt 5*d* DOS has a long tail toward E_F. Assuming the similar tail feature for both compounds, $Yb_2Pt_6Ga_{15}$ with its shallower Pt 5*d* peaks is expected to have a larger Pt 5*d* DOS at E_F, which might be reflected in the increased spectral intensity around 1 eV in $Yb_2Pt_6Ga_{15}$. The similarities between the X-dependent spectra of $YbNi_3X_9$ and $Yb_2Pt_6X_{15}$ suggest some systematic changes in the electronic structure when the compounds with the same crystal structure and similar conduction electron states move from nonmagnetic state to magnetic regions in the Doniach phase diagram.

We compare the electronic structure of $Yb_2Pt_6X_{15}$ and $YbNi_3X_9$ [5.7]. We recall T_K of these materials; 2.7 K for $YbNi_3Al_9$, 64 K for $Yb_2Pt_6Al_{15}$, 570 K for $YbNi_3Ga_9$ and ~2100 K for $Yb_2Pt_6Ga_{15}$ derived from the Yb^{2+} $4f_{7/2}$ peak energy. The Yb valences at 300 K are 2.97 for $YbNi_3Al_9$, 2.89 for $Yb_2Pt_6Al_9$, 2.59 for $YbNi_3Ga_9$ and 2.34 for $Yb_2Pt_6Ga_{15}$, and the $^3H_6$ peak positions are 5.5, 5.8, 6.0, and 6.6 eV, respectively. Figures 5.15 (a) and (b) show the Yb valence as functions of $^3H_6$ peak position and T_K, respectively. Figure 5.15 (a) clearly reveals the correlation between the Yb valence and $^3H_6$ peak energies. This trend can be understood assuming that the deeper $^3H_6$ peak reflects the Yb^{3+} 4*f* hole level closer to E_F as mentioned above. The conduction electrons more easily transfer into the Yb^{3+} 4*f* hole and the Yb valence is shifted to divalent side. Figure 5.15 (b) shows the Yb valence also systematically decreases with increasing T_K. As discussed before, the Yb valence significantly changes around T_K. For high T_K, the Yb valence starts to decrease from a specific high temperature and it becomes small at

the temperature in the measurement region. Therefore, the high T_K corresponds to small Yb valence, and the low T_K one corresponds to large Yb valence.

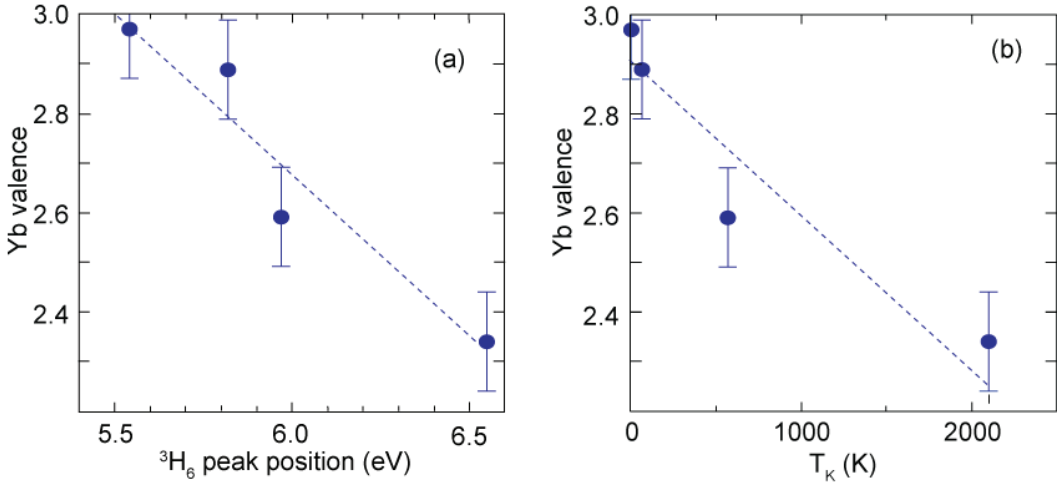

Figure 5.15: Yb valences plotted for (a) $^3H_6$ peak position and (b) T_K for $Yb_2Pt_6X_{15}$ together with those of $YbNi_3X_9$. Dashed lines are guides for eye.

Table I: Atomic and two interlayer distances of $Yb_2Pt_6X_{15}$ and $YbNi_3X_9$ in units of Å. See text.

	$Yb_2Pt_6Al_{15}$	$Yb_2Pt_6Ga_{15}$	$YbNi_3Al_9$	$YbNi_3Ga_9$
R(Yb-X)	3.22	3.13	2.97	2.96
L(Yb_2X_3-X)	1.94	1.94	1.82	1.82
L(Yb_2X_3-Ni/Pt)	2.28	2.38	2.22	2.26

According to Harrison, the hybridization strength increases with increasing the effective radii of the respective orbitals and with decreasing the interatomic distance [5.24]. The effective radii of *d* orbitals of Pt and Ni are estimated to be r_d(Pt)=1.04 and r_d(Ni)=0.71, respectively [5.24]. Those of *p* orbitals of Al and Ga (r_p(Al) and r_p(Ga)) could not be found in the literature. Since r_p(Si)<r_p(Ge), r_p(P)<r_p(As) and r_p(S)<r_p(Se) [5.25], we reasonably assume r_p(Al)<r_p(Ga). These facts that r_d(Ni)<r_d(Pt) and r_p(Al)<r_p(Ga) qualitatively explain that the hybridization is stronger for $Yb_2Pt_6X_{15}$ than for $YbNi_3X_9$ and stronger for $Yb_2Pt_6Ga_{15}$ ($YbNi_3Ga_9$) than for $Yb_2Pt_6Al_{15}$ ($YbNi_3Al_9$). On the other hand, Table I compares one atomic and two interlayer distances of $Yb_2Pt_6X_{15}$ and $YbNi_3X_9$ in unit of Å, taken from our XRD data. R(Yb-X) is the atomic distance between Yb and X ions in the Yb_2X_3 layer, and L(Yb_2X_3-X) and L(Yb_2X_3-Ni/Pt) are the interlayer distances between Yb_2X_3 and X, and Yb_2X_3 and Ni/Pt layers, respectively. In contrast to the discussion of the hybridization strength using the

effective radii of orbitals, we find opposite correlation between the distances and hybridization strength except for R(Yb-Al)>R(Yb-Ga) for $YbNi_3X_9$. Accordingly, the effective radii are expected to contribute more to the hybridization strength for $Yb_2Pt_6X_{15}$ and $YbNi_3X_9$.

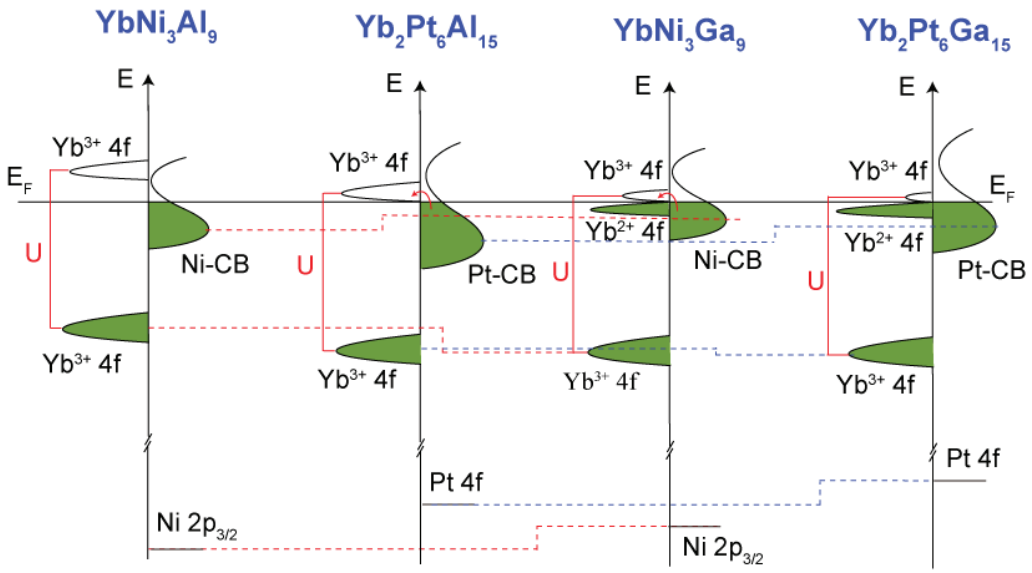

Figure 5.16: Schematic view of the electronic structure model of $Yb_2Pt_6X_{15}$ and $YbNi_3X_9$. U stands for the Coulomb interaction energy between 4f electrons. The vertical axis represents the energy relative to E_F.

Based on the HAXPES results of $Yb_2Pt_6X_{15}$ and $YbNi_3X_9$, their electronic structures are schematically shown in Fig. 5.16. The vertical axis represents the energy relative to E_F, and the Yb 4f and conduction band DOS are located left and right side of the vertical line, respectively. U is the Coulomb interaction energy between the 4f electrons. On going from left ($YbNi_3Al_9$) to right ($Yb_2Pt_6Ga_{15}$), T_K, increases. Because the Yb valence of $YbNi_3Al_9$ is close to +3, the 4f hole level exists far above from E_F, the conduction electrons are too hard to go into the 4f hole and Yb valence is almost unchanged with temperature. The energy shift of the Yb^{3+} 4f peak for $YbNi_3Al_9$ and $Yb_2Pt_6Al_{15}$ suggests that the Yb 4f hole level of $Yb_2Pt_6Al_{15}$ gets close to E_F and the conduction electrons go into the 4f hole, and as a consequence the Yb valence starts to decrease. On going further to $YbNi_3Ga_9$, the conduction electrons more easily go into the Yb 4f hole which is closer to E_F and Yb valence fluctuation gets strong. For $Yb_2Pt_6Ga_{15}$, the conduction electrons almost fill the 4f hole leading to almost Yb^{2+} and again the conduction electrons too hard to further go into the 4f hole making the Yb valence stable. The Pt 5d and Ni 3d DOS at E_F are expected to increase from $YbNi_3Al_9$ to $Yb_2Pt_6Al_{15}$ to $YbNi_3Ga_9$ and to $Yb_2Pt_6Ga_{15}$.

5.6 Results of ARPES

In order to see *c-f* hybridization band and the Fermi surface structures, we carried out APRPES measurement on $Yb_2Pt_6X_{15}$ at BL-1 and BL-9A of HiSOR. Figure 5.17 (a) shows an intensity plot of the Fermi surface map in the k_x-k_y plane of $Yb_2Pt_6Ga_{15}$ obtained by changing azimuth angle and excited with *p*-polarized light with $\hbar\omega$=35 eV at 20 K, whereas Fig. 5.17 (b) shows that with *s*-polarized light. The intensity of the Fermi surface maps was integrated within 50 meV above and below E_F. The hexagonal Fermi surfaces with even and odd symmetries centered at the Γ point of first Brillouin zone clearly observed, respectively.

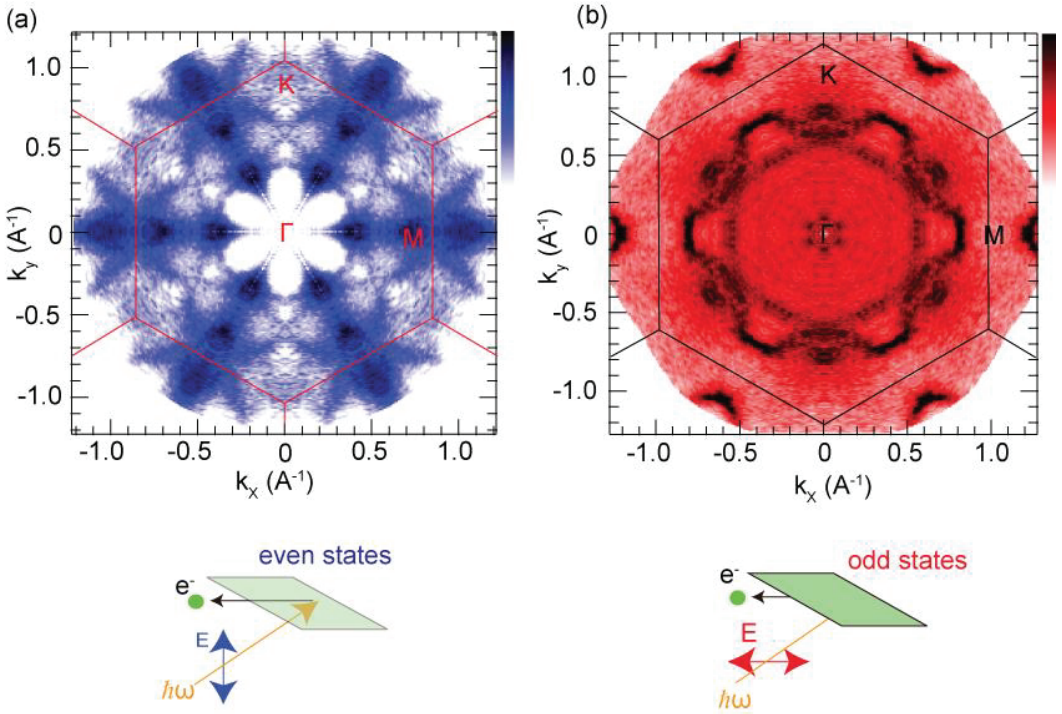

Figure 5.17. Two dimensional Fermi surface maps of $Yb_2Pt_6Ga_{15}$ in the k_x-k_y plane are taken with (a) *p*-polarized and (b) *s*-polarized lights at 20 K. Lower figures show the respective experimental configurations.

Figures 5.18 (a) and (b) show the ARPES intensity plots of $Yb_2Pt_6Al_{15}$ along Γ-M direction measured with *s*- and *p*-polarized lights with $\hbar\omega$=35 eV at 20 K. respectively. Both the dispersive conduction bands and nondispersive (localized) Yb^{2+} 4*f* bands are very clearly observed. The main peaks at 0.03 and 1.3 eV are attributed to spin-orbit coupling of the Yb^{2+} $4f_{7/2}$ and $4f_{5/2}$ components in the bulk as shown in Fig 5.18 (c), respectively. Additional broad structure in the region of

1.0~1.3 eV is derived from surface and subsurface Yb^{2+} 4*f* states [5.26]. With the *p*-polarized light, in first Brillouin zone very clear four conduction bands intersect with Yb^{2+} 4*f* bands around Γ point as shown in Fig 5.18 (a). On the other hand, in the *s*-polarized result (Fig. 5.18 (b)), the four bands almost dissappear, but, new bands are excited.

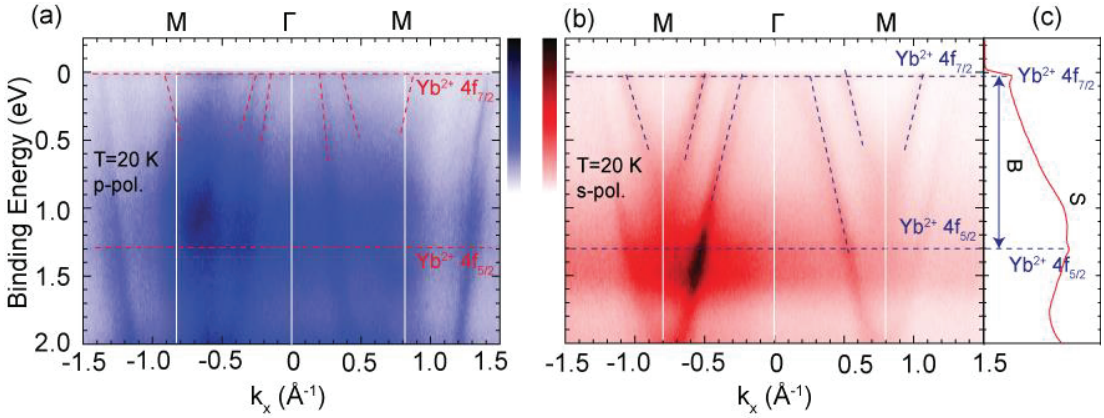

Figure 5.18. Intensity plot of ARPES spectra of $Yb_2Pt_6Al_{15}$ along Γ-M direction are taken with (a) *p*-polarized and (b) *s*-polarized ligts at $\hbar\omega$=35 eV at 20 K. The dashed lines indicate Yb^{2+} *f* and conduction bands. (c) Angle-intigrated spectrum obtained from (b). The bulk and surface Yb^{2+} 4*f* components are indicated with "B" and "S", respectively.

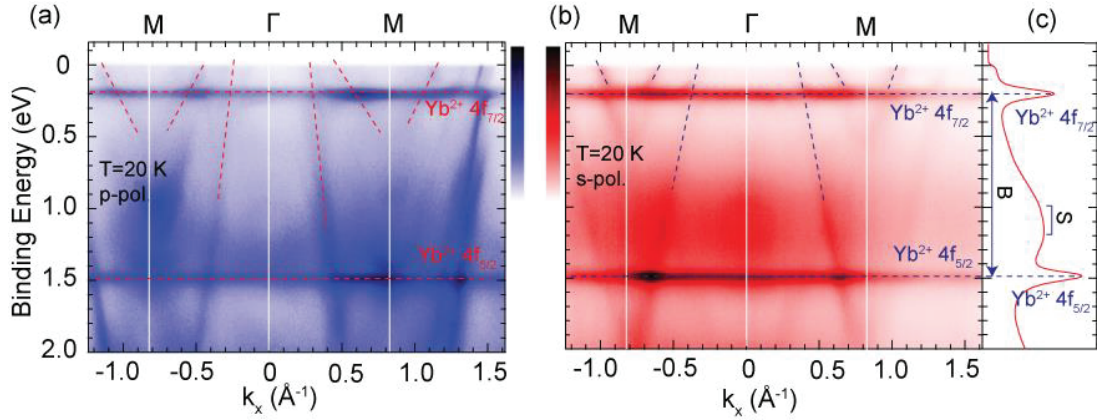

Figure 5.19. Intensity plot of ARPES spectra of $Yb_2Pt_6Ga_{15}$ along Γ-M direction taken with (a) *p*-polarized and (b) *s*-polarized ligts at $\hbar\omega$=35 eV at 20 K. The dashed lines indicate Yb^{2+} 4*f* and conduction bands. (c) Angle-intigrated spectrum obtained from (b). The bulk and surface Yb^{2+} 4*f* components are indicated with "B" and "S", respectively.

For comparison, Fig. 5.19 shows the ARPES intensity plots of $Yb_2Pt_6Ga_{15}$ along Γ-M direction measured with the same condition. The stronger bulk Yb^{2+} $4f_{7/2}$ and $4f_{5/2}$ components are observed at 0.2 and 1.5 eV, respectively. Their energy positions and intesities are deeper and strongger, respectively, than those of $Yb_2Pt_6Al_{15}$. Several conduction bands are observed with *p*-polarized light, and they intersect with flat Yb^{2+} 4*f* bands and band-bending feature is clearly observed at cross point. In contrast, when we use *s*-polarized light, as the $Yb_2Pt_6Al_{15}$ case, the bands disappear and new bands are observed.

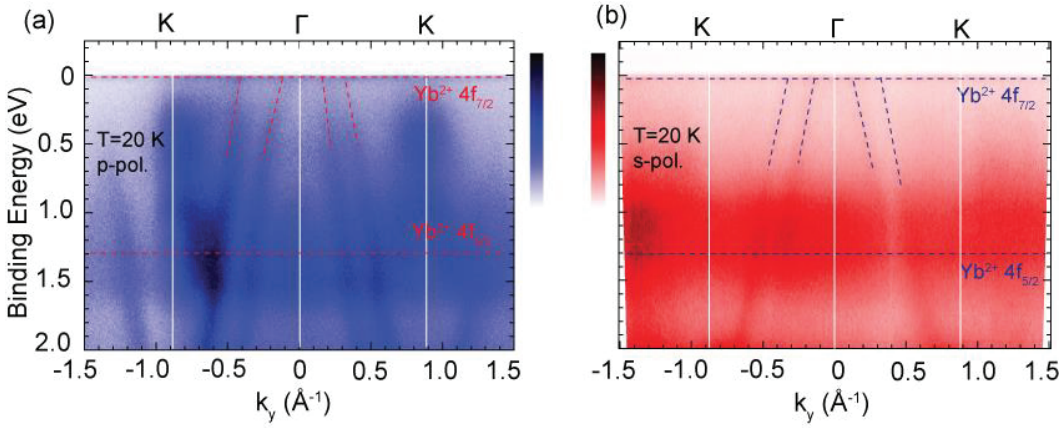

Figure 5.20. Intensity plots of ARPES spectra of $Yb_2Pt_6Al_{15}$ along Γ-K direction taken with (a) *p*-polarized and (b) *s*-polarized lights at $\hbar\omega$=35 eV at 20 K. The dashed lines indicate the Yb^{2+} 4*f* and condcution bands.

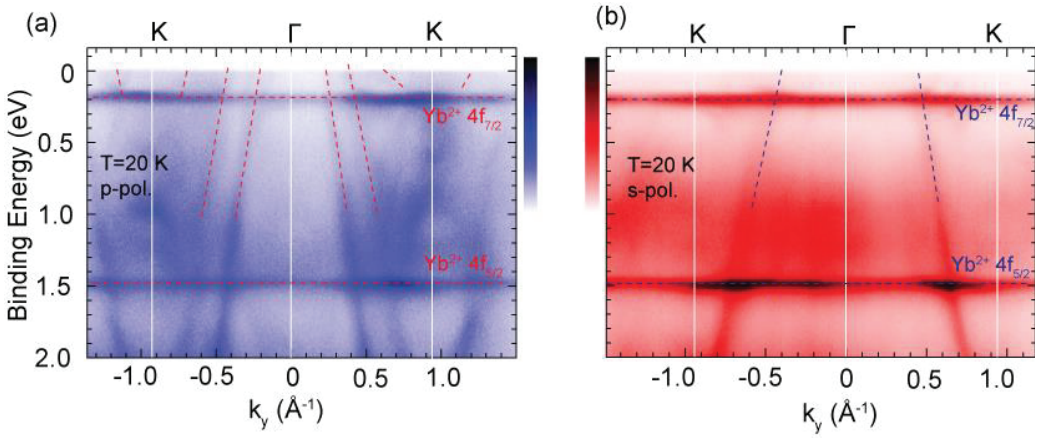

Figure 5.21. Intensity plots of ARPES spectra of $Yb_2Pt_6Ga_{15}$ along Γ-K direction are taken with (a) *p*-polarized and (b) *s*-polarized lights at $\hbar\omega$=35 eV at 20 K. The dashed lines indicate the Yb^{2+} 4*f* and conduction bands.

Figures 5.20 and 5.21 show the ARPES intensity plots of $Yb_2Pt_6Al_{15}$ and $Yb_2Pt_6Ga_{15}$, respectively, along Γ-K direction taken with *p*- and *s*-polarized lights.

We can clearly see the conduction bands hybridized with the flat Yb^{2+} 4*f* bands with *p*-polarized light. In contrast, with *s*-polarized light, the bands almost disappear or become very weak. In order to determine the origin of the conduction bands we will perform the band-strucutre calculation based on the density functional theory (DFT).

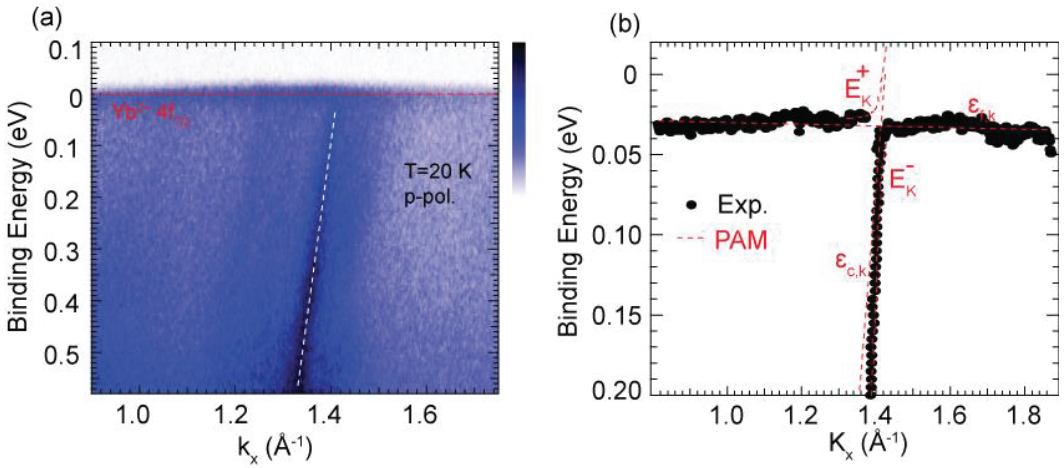

Figure 5.22. (a) *c-f* hybridization band of $Yb_2Pt_6Al_{15}$ taken along Γ-M direction. The dashed lines indicate the Yb^{2+} 4*f* and conduction bands. (b) Analysis of the *c-f* hybridization band with PAM. The experimental data points were obtained by a Lorentzian fitting of MDC or EDC spectra and the dashed lines were obtained from PAM.

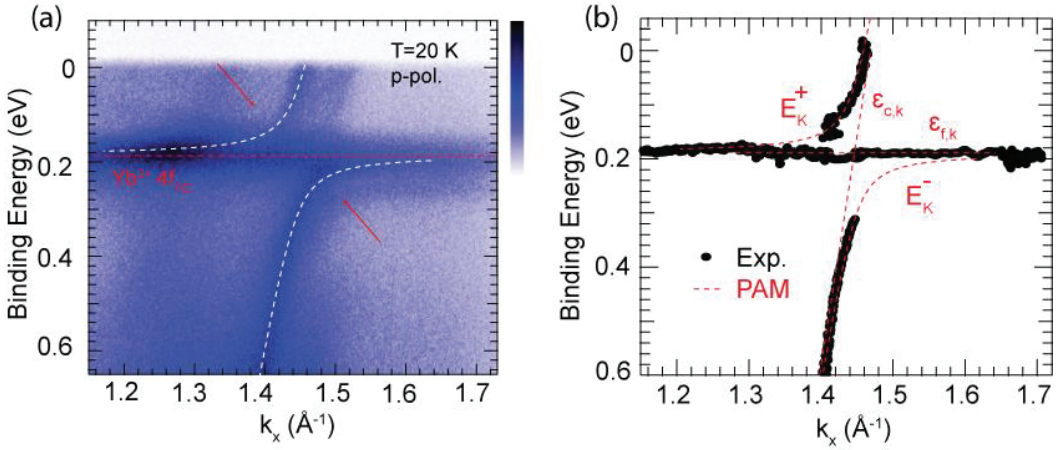

Figure 5.23. (a) *c-f* hybridization band of $Yb_2Pt_6Ga_{15}$ taken along Γ-M direction. The dashed lines indicate the Yb^{2+} 4*f* and renormalized bands. (b) Analysis of the *c-f* hybridization band with PAM. The experimental data points were obtained by the Lorentzian fitting of MDC or EDC spectra and the dashed lines were obtained from PAM.

The *c-f* hybridization bands observed for $Yb_2Pt_6Al_{15}$ and $Yb_2Pt_6Ga_{15}$ are shown in Figs. 5.22 and 5.23, respectively, which are taken with *p*-polarized light with $\hbar\omega$=35 eV and at 20 K. In the spectra of $Yb_2Pt_6Al_{15}$ as shown in Fig. 5.22 (a), the conduction band intersects with the Yb^{2+} 4*f* band at ~1.42 $Å^{-1}$ and ~0.029 eV. On the other hand, in the $Yb_2Pt_6Ga_{15}$ case as shown in Fig. 5.23 (a), the conduction band intersects with the Yb^{2+} 4*f* band at ~1.42 $Å^{-1}$ and 0.192 eV, and forms the band-bending feature.

We analyze the *c-f* hybridization band feature with PAM. Neglecting the Coloumb interaction between 4*f* electrons U=0, the band dispersion is expressed by

$$E^{\pm} = \frac{\varepsilon_{c,k}+\varepsilon_{f,k} \pm \sqrt{(\varepsilon_{c,k}-\varepsilon_{f,k})^2 - 4V_k}}{2}, \qquad (4\text{-}1)$$

where $\varepsilon_{c,k}$ and $\varepsilon_{f,k}$ are the energies of the bare conduction-band and 4*f* electrons, respectively, and V_k is hybridization energy [5.27]. As a simplification to fit the experimental data using this formula, a linear band dispersion is assumed for $\varepsilon_{c,k}$, and $\varepsilon_{f,k}$ and V_k are assumed to be constant. Figures 5.22 (b) and 5.23 (b) show the fitting results of $Yb_2Pt_6Al_{15}$ and $Yb_2Pt_6Ga_{15}$, respectively, in which the experimental data with black points were obtained by the Lorentzian fit to momentum distribution curve (MDC) or energy distribution curve (EDC) and the red dashed lines are the fitting results. They are plotted as the absolute value of k_x or k_y. We derived to be $\varepsilon_{f,k}$ ~0.029 eV and V_k ~0.0008 eV for $Yb_2Pt_6Al_{15}$, and $\varepsilon_{f,k}$ ~0.189 eV and V_k ~0.13 eV for $Yb_2Pt_6Ga_{15}$. The fitting results well reproduce the experimental dispersion. From the value of $\varepsilon_{f,k}$, T_K are estimated to be ~330 K for $Yb_2Pt_6Al_{15}$ and ~2200 K for $Yb_2Pt_6Ga_{15}$, respectively, consistent with the trend obtained by magnetic susceptibility measurement results [5.3,5.4].

The mass enhancement factor is related to the dispersion of E^+ at k_f by

$$\frac{m^*}{m_b} = \frac{v_{c,k}}{v^*} = \frac{\partial\varepsilon_{c,k}}{\partial k} \Big/ \frac{\partial E^+}{\partial k}, \qquad (4\text{-}2)$$

where m^* and m_b are hybridized and unhybridized band energy, respectively, and $v_{c,k}$ and v^* are electron velocities of unhybridized and hybridized bands, respectively. From the fitting results, the mass enhancement factor m^*/m_b are estimated to be ~1.18 for $Yb_2Pt_6Al_{15}$ and ~1.59 for $Yb_2Pt_6Ga_{15}$, respectively. These results show that $Yb_2Pt_6Al_{15}$ ($Yb_2Pt_6Ga_{15}$) has small (large) *c-f*

hybridization and mass enhancement, consistent with the difference of T_K. The results of $Yb_2Pt_6Ga_{15}$ are close to those of the Kondo lattice $YbAl_2$ [5.26].

5.7 Conclusion

The electronic structure of $Yb_2Pt_6X_{15}$ has been investigated by HAXPES with $\hbar\omega$=5.95 keV. Both Yb^{2+} and Yb^{3+}-derived structures were clearly observed in the Yb 3*d* HAXPES spectra. The intensity of the Yb^{2+} (Yb^{3+}) structures in Yb $3d_{5/2}$ spectra of $Yb_2Pt_6Al_{15}$ gradually increase (decrease) on cooling. The Yb valence is estimated to be ~2.9 at 300 K, showing valence fluctuation, and gradually decrease to ~2.8 at 20 K. On the other hand, the Yb 3*d* spectra of $Yb_2Pt_6Ga_{15}$ show almost no temperature independence with the Yb valence to be ~2.34. On going from Al to Ga in $Yb_2Pt_6X_{15}$, the Pt $4f_{7/2}$ and Pt $4d_{5/2}$ states are shifted toward lower E_B side by 0.3 and 0.25 eV, respectively. At the same time, in the valence-band spectra, we found that the Yb^{3+} 4*f* structures are located at the shallower E_B in $Yb_2Pt_6Al_{15}$ than $Yb_2Pt_6Ga_{15}$. We described the enhanced *c-f* hybridization and T_K in $Yb_2Pt_6Ga_{15}$ based on the Pt-derived DOS at E_F and the Yb^{3+} 4*f* hole level relative to E_F.

For comparison, the results of $Yb_2Pt_6X_{15}$ were compared with those of the Kondo lattices $YbNi_3X_9$ [5.7]. As $Yb_2Pt_6X_{15}$, although $YbNi_3X_9$ have similar crystal structure and same X, $YbNi_3Al_9$ has antiferromagnetic ground state (a chiral helical order) and Yb valence close to 3+, while $YbNi_3Ga_9$ exhibits a typical valence fluctuation behavior. We found similar energy shifts in the Yb^{3+} 4*f* structures of valence-band spectra and Pt $4f_{7/2}$ and Ni $2p_{3/2}$ core level states. The similarities between the X-dependent spectra of $YbNi_3X_9$ and $Yb_2Pt_6X_{15}$ suggest some systematic changes in the electronic structure when the compounds with the same crystal structure and similar conduction electron states move from nonmagnetic state to magnetic regions in the Doniach phase diagram. The origin of the higher T_K of $Yb_2Pt_6X_{15}$ compared to those of $YbNi_3X_9$ is that the Pt-derived DOS at E_F is larger than the Ni-derived DOS at E_F.

The ARPES results show the clear Fermi surface and *c-f* hybridization band structures, and *s*- and *p*-polarization dependences were observed. The *c-f* hybridization band structure is well fitted with PAM, and the hybridization energy and mass enhancement factor were estimated to be V_k~0.0008 eV and m^*/m_b~1.18 for $Yb_2Pt_6Al_{15}$, and V_k~0.13 eV and m^*/m_b~1.59 for $Yb_2Pt_6Ga_{15}$.

Reference:

[5.1] S. Doniach, Physica B&C **91**, 231 (1977).

[5.2] Y. Matsumoto, T. Ueda, and S. Ohara, J. Phys.: Conf. Ser. **683**, 012035 (2016).

[5.3] M. Deppe, S. Hartmann, M. E. Macovei, N. Oeschler, M. Nicklas, and C. Geibel, New. J. Phys. **10**, 093017 (2008)

[5.4] S. Ohara. Private communication.

[5.5] T. Yamashita, R. Miyazaki, Y. Aoki, and S. Ohara, J. Phys. Soc. Jpn. **81**, 034705 (2012).

[5.6] S. Ohara, T. Yamashita, Y. Mori, and I. Sakamoto, J. Phys.: Conf. Ser. **273**, 012048 (2011).

[5.7] Y. Utsumi, H. Sato, S. Ohara, T. Yamashita, K. Mimura, S. Motonami, K. Shimada, S. Ueda, K. Kobayashi, H. Yamaoka, N. Tsujii, N. Hiraoka, H. Namatame, and M. Taniguchi, Phys. Rev. B **86**, 115114 (2012).

[5.8] S. Ohara, S. Fukuta, K. Ohta, H. Kono, T. Yamashita, Y. Matsumoto, and J. Yamaura, JPS Conf. Proc. **3**, 017016 (2014).

[5.9] K. Matsubayashi, T. Hirayama, T. Yamashita, S. Ohara, N. Kawamura, M. Mizumaki, N. Ishimatsu, S. Watanabe, K. Kitagawa, and Y. Uwatoko, Phys. Rev. Lett. **114**, 086401 (2015).

[5.10] S. Ueda, Y. Katsuya, M. Tanaka, H. Yoshikawa, Y. Yamashita, S. Ishimaru, Y. Matsushita, and K. Kobayashi, AIP Conf. Proc. **1234**, 403 (2010).

[5.11] K. Kobayashi, M. Yabashi, K. Tamasaku, D. Miwa, T. Ishikawa H. Nohira, T. Hattori, Y. Sugita, O. Nakatsuka, A. Sakai, and S. Zaima, Appl. Phys. Lett. **83**, 1005 (2003).

[5.12] M. Arita, K. Shimada, H. Namatame, and M. Taniguchi, Surf. Rev. Lett. **9**, 535 (2002).

[5.13] H. Iwasawa, Y. Yoshida, I. Hase, K. Shimada, H. Namatame, M. Taniguchi, and Y. Aiura, Phys. Rev. Lett. **109**, 066404 (2012).

[5.14] M. Taniguchi and J. Ghijsen, J. Synchrotron Radiat. **5**, 1176 (1998).

[5.15] H. Sato, K. Shimada, M. Arita, K. Hiraoka, K. Kojima, Y. Takeda, K. Yoshikawa, M. Sawada, M. Nakatake, H. Namatame, M. Taniguchi, Y. Takata, E. Ikenaga, S. Shin, K. Kobayashi, K. Tamasaku, Y. Nishino, D. Miwa, M. Yabashi, and T. Ishikawa, Phys. Rev. Lett. **93**, 246404 (2004).

[5.16] D. A. Shirley, Phys. Rev. B **5**, 4709 (1972).

[5.17] L. H. Tjeng, S.-J. Oh, E.-J. Cho, H.-J. Lin, C. T. Chen, G.-H. Gweon, J.-H. Park, J. W. Allen, T. Suzuki, M. S. Makivic, and D. L. Cox, Phys. Rev. Lett. **71**, 1419 (1993).

[5.18] M. Matsunami, A. Chainani, M. Taguchi, R. Eguchi, Y. Takata, M. Oura, M. Yabashi, K. Tamasaku, Y. Nishino, T. Ishikawa, M. Kosaka, and S. Shin, J. Phys. Soc. Jpn. **81**, 073702 (2012).

[5.19] J. H. Scofield, Lawrence Livemore Laboratory, Tech. Rep. UCRL-51326 (1973).

[5.20] H. Yamaoka, P. Thunstrom, N. Tsujii, I. Jarrige, K. Shimada, M. Arita, H. Iwasawa, H. Hayashi, J. Jiang, H. Namatame, M. Taniguchi, N. Hiraoka, H. Ishii, K.-D. Tsuei, M. Giovannini, and E. Bauer, Phys. Rev. B **86**, 085137 (2012).

[5.21] H. Sato, K. Yoshikawa, K. Hiraoka, M. Arita, K. Fujimoto, K. Kojima, T. Muro, Y. Saitoh, A. Sekiyama, S. Suga, and M. Taniguchi, Phys. Rev. B **69**, 165101 (2004).

[5.22] J. J. Yeh and I. Lindau, At. Data Nucl. Data Tables **32**, 1 (1985).

[5.23] Yuki. Utsumi, doctoral thesis.

[5.24] W. A. Harrison, "Electronic Structure and the Properties of Solids: The Physics of the Chemical Bond", W.H. Freeman and Company, San Francisco (1980).

[5.25] W. A. Harrison and G. K. Straub, Phys. Rev. B **36**, 2695 (1987).

[5.26] M. Matsunami, T. Hajiri, H. Miyazaki, M. Kosaka, and S. Kimura, Phys. Rev. B **87**, 165141 (2013).

[5.27] A. C. Hewson, "The Kondo problem to heavy Fermions", Cambridge University press (1993).

Chapter 6: Photoemission study of Kondo lattices $YbNi_2X'_2$ (X'=Si, Ge)

6.1 Introduction

The electronic structures of the Kondo lattices $Yb_2Pt_6X_{15}$ are investigated by means of hard x-ray photoemission spectroscopy (HAXPES), vacuum ultraviolet photoemission spectroscopy (VUVPES), low-energy photoemission spectroscopy (LEPES) and angle-resolved photoemission spectroscopy (ARPES) etc., as described in Chapter 5. The Yb valences of $Yb_2Pt_6Al_{15}$ and $Yb_2Pt_6Ga_{15}$ are 2.83 and 2.34 at 20 K, respectively. In the valence-band spectra, the Yb^{3+} 4*f* multiplet structures are shifted to a higher binding energy (E_B) side by ~0.4 eV on going from X=Al to Ga, and the Pt $4d_{5/2}$ and Pt $4f_{7/2}$ spectra are shifted to lower E_B side. These energy shifts can be explained by the Fermi level (E_F) shift in the Pt-derived conduction band states. The increased Pt 5*d* density of states (DOS) at E_F and the Yb 4*f* hole level closer to E_F for $Yb_2Pt_6Ga_{15}$ enhance the *c-f* hybridization, that is, an increase of T_K and decrease the Yb valence. The results of $Yb_2Pt_6X_{15}$ are well compared with previous study on the Kondo lattices $YbNi_3X_9$ [6.1].

$YbNi_2X'_2$ (X'=Si, Ge) have tetragonal $ThCr_2Si_2$-type crystal structure as shown in Fig. 6.1. The nominal electronic configurations of Si and Ge are $3s^23p^2$ and $4s^24p^2$, respectively. Although they have same crystal structure and similar electronic configurations, they exhibit different physical properties as $Yb_2Pt_6X_{15}$ and $YbNi_3X_9$. Figure 6.2 (a) shows temperature dependent magnetic susceptibility of $YbNi_2Si_2$ measured in H=920 Oe [6.2]. The susceptibility around 30 K shows Curie-Weiss behavior with an effective magnetic moment of μ_{eff}=4.5 μ_B, which is close to the value of μ_{eff}=4.54 μ_B for the free Yb^{3+} ion. An antiferromagnetic order is observed at ~2.3 K. Fig. 6.2 (b) shows the temperature dependent magnetic susceptibilities of $YbNi_2Ge_2$ measured in H=10 kG, and it takes maximum at ~50 K [6.3]. The effective magnetic moment is estimated to be μ_{eff}=3.51 μ_B and is lower than the expected value of μ_{eff}=4.54 μ_B for Yb^{3+} ion, suggesting intermediate valence state of Yb in $YbNi_2Ge_2$. The Kondo temperature T_K of $YbNi_2Si_2$ and $YbNi_2Ge_2$ are a few K and ~150 K (from T_K=3T_{max}), respectively. In this chapter, HAXPES studies of $YbNi_2X'_2$ are presented for comparison with $Yb_2Pt_6X_{15}$ and $YbNi_3X_9$.

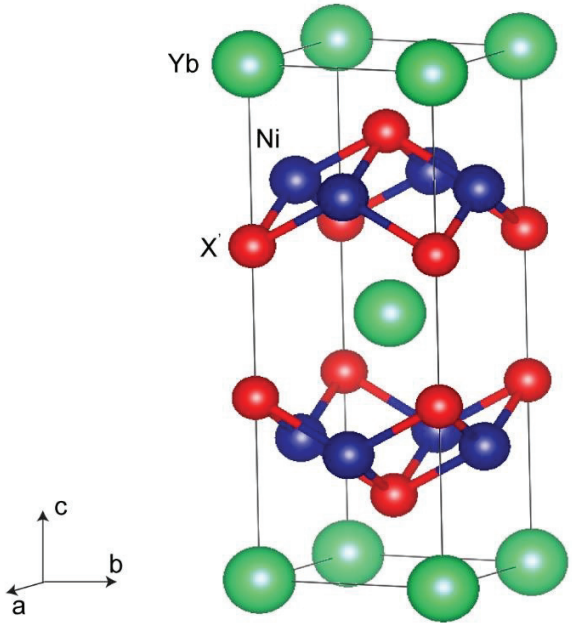

Figure 6.1: Tetragonal $ThCr_2Si_2$-type crystal structure of $YbNi_2X'_2$.

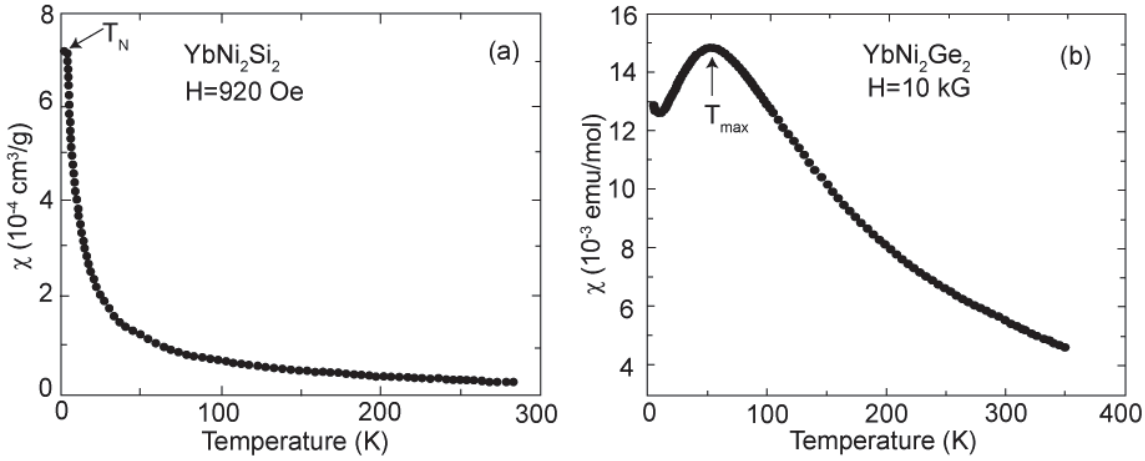

Figure 6.2: Temperature dependent magnetic susceptibility of (a) $YbNi_2Si_2$ [6.2] and (b) $YbNi_2Ge_2$ [6.3].

6.2 Experiment

The HAXPES experiments for $YbNi_2X'_2$ were performed at the undulator beamline BL15XU [6.4, 6.5] of SPring-8. The experiments were carried out under the same conditions as described in Chapter 3. Single crystals of $YbNi_2X'_2$ were

synthesized by the self-flux method by Ohara group at Nagoya institute of technology.

6.3 Results of HAXPES

Figure 6.3 shows HAXPES spectra of $YbNi_2X'_2$ in the wide energy region measured at 300 K. In both spectra, Yb, Ni, Si and Ge-derived structures are very clearly seen. Although the O 1*s*-derived structures are observed at 531 eV, it is negligibly weak compared to the other structure. No signal due to C 1*s* is detected.

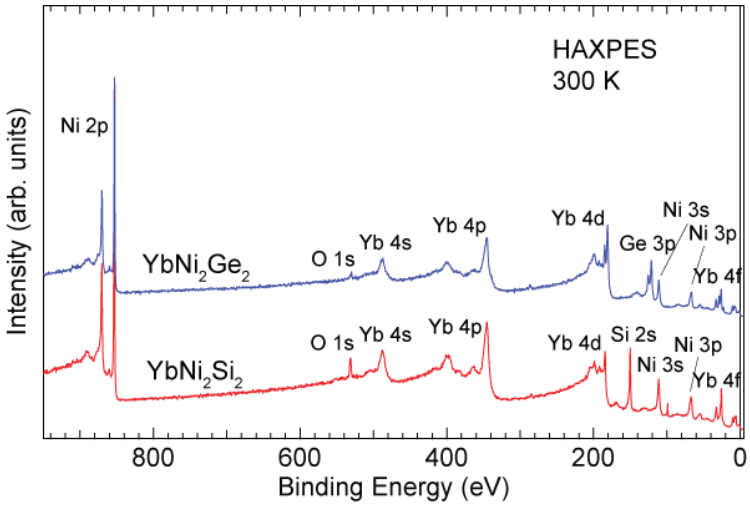

Figure 6.3: HAXPES spectra of $YbNi_2X'_2$ in the wide energy region measured at 300 K.

The temperature dependent Yb 3*d* HAXPES results of $YbNi_2X'_2$ are shown in Fig. 6.4. In all the spectra, the Yb 3*d* spectra are split into $3d_{5/2}$ region at 1515-1540 eV and $3d_{3/2}$ region at 1560-1585 eV due to spin-orbit interaction. The peaks at 1520 and 1568 eV are assigned to Yb^{2+} components. On the other hand, Yb^{3+} components are observed at 1524-1536 eV and 1570-1584 eV as multiplet structures due to the Coulomb interaction between the 3*d*-photohole and Yb^{3+} 4*f* hole with the electron configuration of the $3d^9 4f^{13}$ final states. Broad structures around 1546 and 1594 eV are derived from plasmon excitations. In the Yb 3*d* spectra of $YbNi_2Si_2$ as shown in Fig. 6.4 (a), the intensity of the Yb^{2+}-derived components are much weaker than that of Yb^{3+}-derived multiple structures, implying that the valence of Yb is close to 3+. The intensities of Yb^{2+} and Yb^{3+} structures are almost unchanged with temperature, indicating that the Yb valence of $YbNi_2Si_2$ is almost temperature-independent. In contrast, the intensity of Yb^{2+}

(Yb^{3+}) components in $YbNi_2Ge_2$ gradually increase (decrease) on cooling, as shown in Fig. 6.4 (b), indicating that the Yb valence moves to 2+ side.

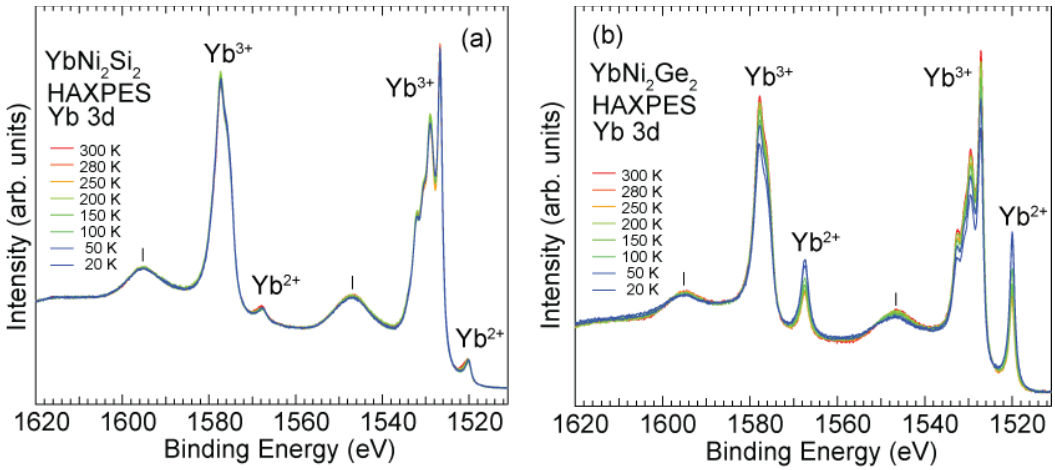

Figure 6.4: Temperature dependences of Yb 3*d* HAXPES spectra of (a) $YbNi_2Si_2$, and (b) $YbNi_2Ge_2$ measured between 300 and 20 K. Vertical bars indicate the plasmon satellite structures.

In order to estimate the Yb valences in these compounds, we performed fitting analyses for the Yb 3*d* spectra. As described in Chapter 3, the calculated line spectra convolved with the Lorentzian function for lifetime broadening were used for Yb^{2+} and Yb^{3+} compounds. The plasmon structures were assumed with the Gaussian functions and the background contribution due to the secondary electrons was estimated by Shirley's method [6.6]. All the spectra were finally broadened with the Gaussian function for instrumental resolution [6.7]. As an example, the fitting result of $YbNi_2Si_2$ at 20 K is shown in Fig. 6.5 (a).

The Yb valences of $YbNi_2Si_2$ and $YbNi_2Ge_2$ were evaluated from the intensity ratio between Yb^{2+} and Yb^{3+} components of the fitted spectra as described in Chapter 3. The evaluated Yb valences are summarized in Fig. 6.5 (b). The Yb valence of $YbNi_2Si_2$ is ~2.97 at 300 K and almost temperature-independent, while that of $YbNi_2Ge_2$ is ~2.90 at 300 K and gradually decrease to ~2.79 at 20 K. The different temperature dependence of the Yb valence in those compounds can be interpreted from their different T_K. Because T_K of $YbNi_2Si_2$ is a few K, far below the measurement temperature region and Yb valence is constant in the measurement region, which same situation as in $YbNi_3Al_9$. T_K of $YbNi_2Ge_2$ is ~150 K and the Yb valence changes within the measurement temperature region as in $YbNi_3Ga_9$.

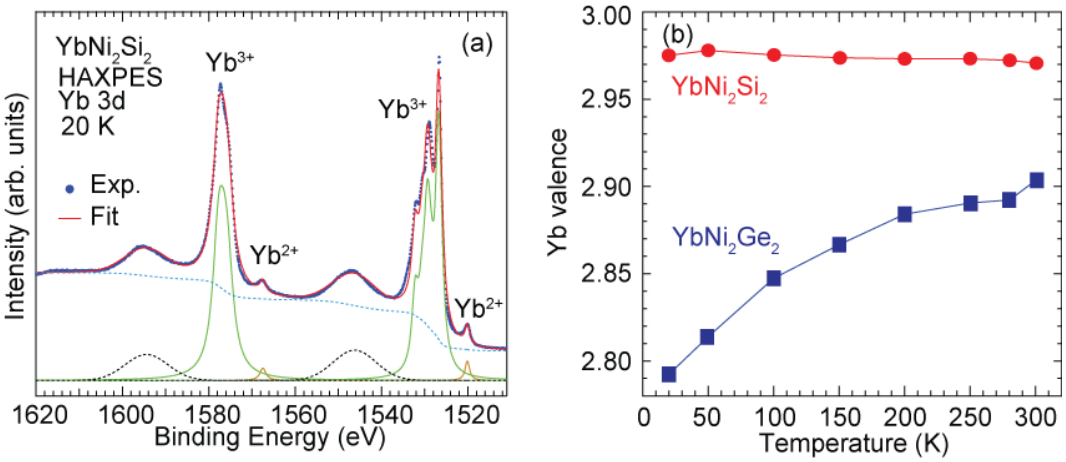

Figure 6.5: (a) Fit of Yb 3*d* HAXPES spectrum of $YbNi_2Si_2$ measured at 20 K. (b) Yb valences of $YbNi_2X'_2$ estimated from the fits of the Yb 3*d* spectra as a function of temperature.

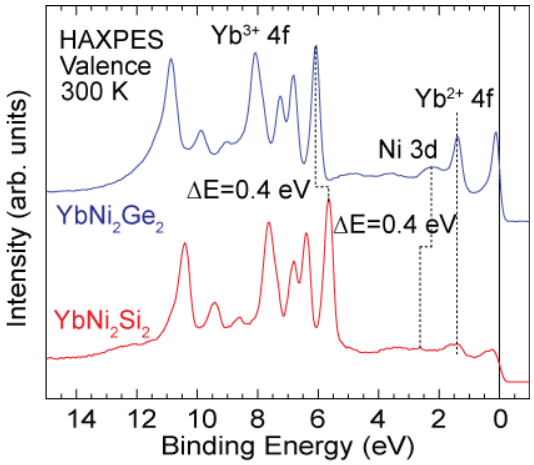

Figure 6.6: Valence-band HAXPES spectra of $YbNi_2X'_2$ measured at 300 K.

Figure 6.6 shows the valence-band HAXPES spectra of $YbNi_2X'_2$ measured at 300 K. The valence-band spectra show clear Yb^{2+} 4*f* and Yb^{3+} 4*f*-derived structures. The prominent peak in the vicinity of E_F in the spectrum of $YbNi_2Ge_2$ is due to Yb^{2+} $4f_{7/2}$ and that at ~1.5 eV is due to Yb^{2+} $4f_{5/2}$. On the other hand, the Yb^{3+} 4*f* state is observed at 5.5 - 12 eV as multiplet structure due to the $4f^{12}$ final state in both spectra. The intensity of Yb^{2+} 4*f* peaks of $YbNi_2Si_2$ is significantly weaker than that of $YbNi_2Ge_2$, implying Yb valence of $YbNi_2Si_2$ is close to 3+ and is larger than $YbNi_2Ge_2$, in consistent with the Yb 3*d* spectra. The tiny peak centered at ~2 eV for $YbNi_2Si_2$ is derived from Ni 3*d* states and that of $YbNi_2Ge_2$ is located at lower E_B than $YbNi_2Si_2$ by 0.4 eV. The Yb^{3+} 4*f* multiplet structures shift to deeper E_B on going from $YbNi_2Si_2$ to $YbNi_2Ge_2$. The energy shift of Yb^{3+} 4*f*

suggests that the 4*f* hole level gradually gets closer to E_F from $YbNi_2Si_2$ to $YbNi_2Ge_2$, and the conduction electrons go into the Yb^{3+} 4*f* hole leading to valence fluctuation for $YbNi_2Ge_2$.

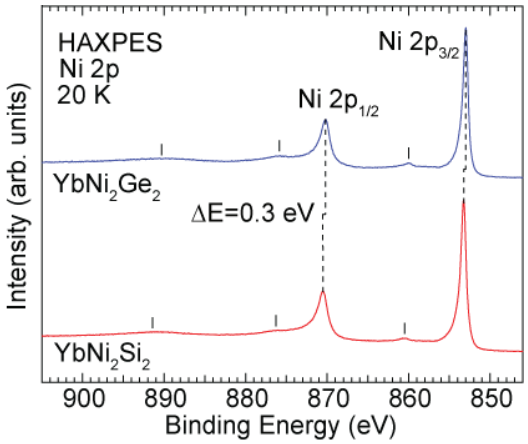

Figure 6.7: Ni 2*p* HAXPES spectra of $YbNi_2X'_2$ measured at 20 K. Vertical bars indicate plasmon satellite structures.

Figure 6.7 shows Ni 2*p* HAXPES spectra of $YbNi_2Si_2$ and $YbNi_2Ge_2$ measured at 20 K. The Ni $2p_{1/2}$ and Ni $2p_{3/2}$ peaks are located at 870 and 853 eV, respectively. One can also see the broad structures at 860.5, 876.5 and 890.5 eV as shown by vertical bars, and a shoulder structure at higher E_B side of the Ni $2p_{1/2}$ peak about 872 eV. These structures were also observed in $YbNi_3X_9$ [6.1]. The broad structure at 890.5 eV and the shoulder structure at 872 eV correspond to bulk plasmon associated with the Ni $2p_{1/2}$ and Ni $2p_{3/2}$, respectively. The surface plasmon energy is usually lower than bulk plasmon energy [6.8, 6.9]. The two peaks at 876.5 and 860.5 eV correspond to the surface plasmons of the Ni $2p_{1/2}$ and Ni $2p_{3/2}$, respectively. E_B of the Ni $2p_{1/2}$ and Ni $2p_{3/2}$ states of $YbNi_2Si_2$ are located at 870.51 and 853.21 eV, respectively, shifting to lower E_B side by amount of ~0.3 eV compared with $YbNi_2Ge_2$. The energy shifts of Ni 2*p* is consistent with that of Ni 3*d* in valence-band spectra. These trends of the spectral change between $YbNi_2X'_2$ are similar to $Yb_2Pt_6X_{15}$ and $YbNi_3X_9$ cases. With decreasing T_K (from $YbNi_2Si_2$ to $YbNi_2Ge_2$, from $YbNi_3Al_9$ to $YbNi_3Ga_9$, and from $Yb_2Pt_6Al_{15}$ to $Yb_2Pt_6Ga_{15}$), the Yb valence is shifted to the divalent side, the Yb^{3+} 4*f* to deeper E_B and the Ni/Pt core states to shallower E_B. This suggests that the characteristic universalities in the electronic structure when the compounds with the same crystal structure and similar conduction electron states move from non-magnetic to magnetic regions in the Doniach phase diagram.

6.4 Conclusion

The HAXPES with $\hbar\omega$=5.95 keV was performed on the Kondo lattices $YbNi_2X'_2$. In the Yb 3*d* HAXPES spectra, both Yb^{2+} and Yb^{3+}-derived components were clearly seen as an evidence of valence fluctuation, in particular for $YbNi_2Ge_2$. The Yb valence estimated from Yb 3*d* spectra of $YbNi_2Si_2$ is ~2.97 at 20 K, and it is almost temperature-independent. On the other hand, the Yb valence of $YbNi_2Ge_2$, is ~2.90 at 300 K and gradually decreases to ~2.79 at 20 K. In the valence-band HAXPES spectra, the Yb^{3+} 4*f* structures gradually shift to deeper E_B from $YbNi_2Si_2$ to $YbNi_2Ge_2$ suggesting the Yb^{3+} 4*f* hole level gets close to E_F, leading to the decrease of the Yb valence for $YbNi_2Ge_2$. The Ni 2*p* of $YbNi_2Si_2$ shifts to lower E_B side compared to that of $YbNi_2Ge_2$. These spectral changes are the same as observed in $Yb_2Pt_6X_{15}$ and $YbNi_3X_9$.

Reference:

[6.1] Y. Utsumi, H. Sato, S. Ohara, T. Yamashita, K. Mimura, S. Motonami, K. Shimada, S. Ueda, K. Kobayashi, H. Yamaoka, N. Tsujii, N. Hiraoka, H. Namatame, and M. Taniguchi, Phys. Rev. B **86**, 115114 (2012).

[6.2] G. Andre, P. Bonville, F. Bouree, A. Bombik, M. Kolenda, A. Oles, A. Pacyna, W. Sikora, and A. Szytula, J. Alloy. Compd. **224**, 253 (1995).

[6.3] S. L. Bud'ko, Z. Islam, T. A. Wiener, I. R. Fisher, A. H. Lacerda, and P. C. Canfield, J. Magn. Magn. Mat. **205**, 53 (1991).

[6.4] S. Ueda, Y. Katsuya, M. Tanaka, H. Yoshikawa, Y. Yamashita, S. Ishimaru, Y. Matsushita, and K. Kobayashi, AIP Conf. Proc. **1234**, 403 (2010).

[6.5] K. Kobayashi, M. Yabashi, K. Tamasaku, D. Miwa, T. Ishikawa H. Nohira, T. Hattori, Y. Sugita, O. Nakatsuka, A. Sakai, and S. Zaima, Appl. Phys. Lett. **83**, 1005 (2003).

[6.6] D. A. Shirley, Phys. Rev. B **5**, 12 (1981).

[6.7] H. Sato, K. Shimada, M. Arita, K. Hiraoka, K. Kojima, Y. Takeda, K. Yoshikawa, M. Sawada, M. Nakatake, H. Namatame, M. Taniguchi, Y. Takata, E. Ikenaga, S. Shin, K. Kobayashi, K. Tamasaku, Y. Nishino, D. Miwa, M. Yabashi, and T. Ishikawa, Phys. Rev. Lett. **93**, 246404 (2004).

[6.8] J. A. Leiro and M. H. Heinonen, Surf. Sci. **346**, 73 (1996).

[6.9] N. Martensson, B. Nyhol, and B. Johansson, Phys. Rev. Lett. **45**, 9 (1980).

Chapter 7: Summary

In this thesis, electronic structures of the Zr, Y and Lu-doped Kondo insulator YbB_{12} and the Kondo lattices $Yb_2Pt_6X_{15}$ (X=Al, Ga) and $YbNi_2X'_2$ (X'=Si, Ge) were studied by means of hard x-ray photoemission spectroscopy (HAXPES) with $\hbar\omega$=5.95 keV, low-energy photoemission spectroscopy (LEPES) with $\hbar\omega$=7 eV, vacuum ultraviolet photoemission spectroscopy (VUVPES) with $\hbar\omega$=182 eV and angle-resolved photoemission spectroscopy (ARPES) with $\hbar\omega$=35 eV.

The electronic structure of the Kondo insulator $Yb_{1-x}Zr_xB_{12}$ was investigated by means of HAXPES and LEPES. In the Yb 3*d* HAXPES spectra, both Yb^{2+} and Yb^{3+}-derived structures were clearly seen for $0 \leq x \leq 0.875$, indicating valence fluctuation. The Yb valence decreases with Zr-doping and on cooling. The valence at 300 K changes from 2.93 for YbB_{12} (x=0) to 2.83 for $Yb_{0.125}Zr_{0.875}B_{12}$ (x=0.875). The Yb^{3+} 4*f* multiplet structures in the valence-band spectra shifts to the deeper binding energy (E_B) with Zr-doping, reflecting that the Yb^{3+} 4*f* hole level becomes closer to Fermi level (E_F). The energy shifts of the B 1*s* and Zr $3d_{5/2}$ peaks toward deeper E_B, which is understood as a result that the supplied electrons by Zr-doping push E_F to higher energy of the conduction-band DOS. The detailed gap formation at E_F were clearly observed by LEPES. In YbB_{12}, the pseudo gap at 18 meV starts to open from 130 K. The *c-f* hybridization and Yb $4f_{7/2}$ peaks are observed at 15 and 45 meV, respectively. With Zr-doping, the *c-f* hybridization peak disappears and the spectral weight at E_F is gradually recovered by Zr-doping and the pseudo gap is closed.

The electronic structures of $Yb_{1-x}R_xB_{12}$ (R= Y, Lu) were also studied by means of HAXPES and LEPES for comparison with the results of $Yb_{1-x}Zr_xB_{12}$. Both Yb^{2+} and Yb^{3+}-derived structures are clearly seen in the Yb 3*d* HAXPES spectra and the intensity of Yb^{2+} components gradually increases while that of Yb^{3+} gradually decreases with increasing R-concentration. The Yb 3*d* spectra of $Yb_{0.125}Y_{0.875}B_{12}$ shows temperature dependence on cooling, and the Yb valence is ~2.88 at 300 K and gradually decreases to 2.84 at 20 K. In the valence-band HAXPES spectra at 300 K, the Yb^{2+} 4*f* and Yb^{3+} 4*f*-derived structures are observed near E_F and at 6 - 12 eV, respectively. With R-doping the Yb^{3+} 4*f* multiplet structures gradually shifts to higher E_B side and the Yb 4*f* hole level gradually closer to E_F. In the B 1*s* spectra, the energy shifts toward higher E_B side with R-doping are also observed.

The energy shifts in the core level suggest that the conduction electron is transferred mainly from B site to Yb site, leading to the decrease of the Yb valence. The decreases of the Yb valence and the energy shifts of the core levels with R-doping similar to the Zr-doping case. However, the changes are smaller than the Zr-doping case. Temperature dependent LEPES was also performed for $Yb_{1-x}R_xB_{12}$. We clearly observed the pseudo gap is still opens in $Yb_{0.5}Y_{0.5}B_{12}$ and $Yb_{0.5}Lu_{0.5}B_{12}$ in contrast to $Yb_{0.5}Zr_{0.5}B_{12}$, where the pseudo gap is already closed. The gap is closed in $Yb_{0.125}Y_{0.875}B_{12}$. These results suggest that the electron doping plays significant role in the pseudo gap closing. The large change in the maximal value of in the magnetic susceptibility (T_{max}) observed only in the Zr-doping system $Yb_{1-x}Zr_xB_{12}$ is also originated from the electron doping system.

The electronic structures of the Kondo lattices $Yb_2Pt_6X_{15}$ were investigated by means of HAXPES, LEPES, VUVPES and ARPES. In the Yb 3*d* HAXPES spectra, the both Yb^{2+} and Yb^{3+}-derived structures were clearly observed. The intensity of the Yb^{2+} (Yb^{3+}) structures for $Yb_2Pt_6Al_{15}$ gradually increases (decreases) on cooling, showing significant valence fluctuation. The estimated Yb valence of $Yb_2Pt_6Al_{15}$ is 2.89 at 250 K and gradually decreases to 2.83 at 20 K. On the other hand, the Yb 3*d* spectra for $Yb_2Pt_6Ga_{15}$ show almost temperature-independent with the Yb valence of 2.34. The energy shifts toward lower E_B by ~0.3 and 0.25 eV were observed in the Pt $4f_{7/2}$ and Pt $4d_{5/2}$ states on going from X=Al to Ga. At the same time, in the valence-band HAXPES and VUVPES spectra, we found the energy shift toward deeper E_B in the Yb^{3+} 4*f* multiplet structures. Based on the experimental results, we proposed the electronic model of $Yb_2Pt_6X_{15}$.

These results are well compared with the Kondo lattices $YbNi_3X_9$ with the similar crystal structure as $Yb_2Pt_6X_{15}$ and the same local coordination around the Yb atom. In $YbNi_3X_9$, $YbNi_3Al_9$ has antiferromagnetic (a chiral helical order) ground state and Yb valence close to 3+. On the other hand, $YbNi_3Ga_9$ exhibits a typical valence fluctuation behavior with the Yb valence of 2.6. We compared the valence-band and core level spectra of both $Yb_2Pt_6X_{15}$ and $YbNi_3X_9$ systems, and proposed a common electronic model. We described the enhanced *c-f* hybridization and T_K in $Yb_2Pt_6X_{15}$ based on the Pt-derived DOS at E_F and the Yb^{3+} 4*f* hole level relative to E_F. The increased Pt 5*d* DOS at E_F and Yb^{3+} 4*f* hole level closer to E_F for $Yb_2Pt_6Ga_{15}$ increases the *c-f* hybridization and T_K, and decreases the Yb valence. We also conclude that the larger Pt-derived conduction-band DOS at E_F compared to Ni-derived conduction-band DOS at E_F is a main reason for their different physical properties. The same trend is observed between $YbNi_2Si_2$ with low T_K and $YbNi_2Ge_2$ with high T_K. The similarity suggests that the characteristic universalities in the electronic structure when the compounds with

the same crystal structure and similar conduction electron states move from non-magnetic to magnetic regions in the Doniach phase diagram. We performed ARPES measurements on $Yb_2Pt_6X_{15}$ and the results show very clear Fermi surface structure and *c-f* hybridization band features. Based on periodic Anderson model (PAM) without the 4*f*-4*f* Coulomb interaction energy, we fitted the *c-f* hybridization band feature and the *c-f* hybridization energy and the mass enhancement factor are estimated to be 0.0008 eV and 1.18 for $Yb_2Pt_6Al_{15}$, and those are 0.13 eV and 1.59 for $Yb_2Pt_6Ga_{15}$.

Acknowledgments

Firstly, I would like to sincerely thank my supervisor, Associate Professor Hitoshi Sato, for the patient guidance, encouragement and advice he has provided over three years. I have been extremely lucky to have a supervisor who cared so much about my research, and who respond my questions so quickly.

I would also like to thank Professor Masaki Taniguchi, Professor Hirofumi Namatame, Associate Professor Galif Kutluk and again my supervisor Associate professor Hitoshi Sato. They gave me a valuable opportunity to interview for the PhD position. Associate professor Galif teached me a lot of knowledge about operation and basic principles of machines. Also, I like to thank to Professor Kenya Shimada for giving me valuable comments to paper writing.

I would like to thank Mr. Masashi Arita, Dr. Eike Fabian Schwier and Mr. Mingtian Zheng. They not only supported in my ARPES and LEPES measurements in BL-9A and BL-1 at HiSOR, but also gave me valuable suggestions for data collection and fruitful discussion regarding the collected results. Moreover, I thank again Mr. Masahi Arita for helping me in my supervisor absence. I also again thank Dr. Eike Fabian Schwier, who did band structure calculations of $Yb_2Pt_6X_{15}$ to support our interpretation of the experimental data.

It is my pleasure to express my thanks to Professor Fumitoshi Iga, Mr. Kento Hayashi, Mr. Katsuya Ishii and Mr. Toru Wada for growing Zr- and R-doped YbB_{12}, and Professor Shigeo Ohara, Dr. Yuji Matsumoto and Dr. Takuya Ueda for growing $Yb_2Pt_6X_{15}$ and $YbNi_2X'_2$ used for the HAXPES, VUVPES, LEPES and ARPES experiments. I cannot do experiments for my thesis without their high-quality samples. I also thank them for stimulating discussion and valuable comments. I also express my thanks to Dr. Shigenori Ueda for the support in HAXPES experiments at BL15XU at SPring8. I want to thank to Professor Kojiro Mimura, Dr. Hiroaki Anzai and Mr. Katsuya Ichiki for their corporation and kind helps in the experiments at SPring8. I also thank them for discussion and comments on the published paper. I like to thank our group members Mr. Toshiki Nagasaki and Mr. Shogo Nakamura for their huge support. I want to thank all the members of the HiSOR who helped me and supported me in my research.

I want to express my gratitude to my parents, brothers and sister. They have encouraged and supported me all stages of my education. I will be grateful forever.

The HAXPES experiments at SPring-8 were under the approvals of NIMS Synchrotron X-ray Station (Proposal Nos. 2014B4800, 2014B4902, 2015A4800, 2015A4906, 2015B4801, 2015B4908, 2016A4802, 2016A4906, 2016B4801, 2016B4908, 2017A4800, 2017A4907). The VUVPES, LEPES and ARPES experiments at HiSOR are performed under the approval of HSRC (Proposal Nos. 14-A-31, 14-A-32, 15-A-41, 15-A-42, 16AG042, 16BG036, 16BG037, 17AG044). This work was partly supported by JSPS KAKENHI Grant Numbers 15K05174, 26400333, and 16H01073 (J-Physics) and by NIMS microstructural characterization platform as a program of "Nanotechnology Platform" (Project No. 12024046) of the MEXT, Japan.

Finally, I would like to thank the JSPS, not only for providing the funding which allowed me to undertake this research, but also for giving me the opportunity to attend conferences and meet so many interesting people.

August 2017 Awabaikeli Rousuli